

Fig 16. Histograms of links strength in the brain-respiration network during different sleep stages. Group averaged links strength are obtained using the TDS measure, where each link represents the interaction of the respiratory system with a given brain area through a specific frequency band. Links are separately grouped by brain areas (Frontal, Central or Occipital), and are arranged in order from low-frequency (δ and θ) to high-frequency (γ_1 and γ_2) bands. Brain-respiration networks are characterized by a very homogeneous frequency profile of links strength which is consistently observed across all brain areas—an almost flat distribution across all 7 physiologically relevant frequency bands (δ , θ , α , σ , β , γ_1 , γ_2). The sleep-stage stratification observed for the links strength in the brain-respiration radar-charts (Fig 15) is consistently observed for all frequency bands and brain areas although less pronounced compared to other brain-organ networks. A strong symmetry in the links strength distribution between the left and right hemisphere is present for all sleep stages. Overall brain-respiration links are much weaker than in other brain-organ networks.

doi:10.1371/journal.pone.0142143.g016

Further, with transitions across sleep stages we observe a complex hierarchical reorganization in both the number and the strength of links in the integrated brain-organs network—lowest number of links during DS (sparse network), higher during REM, and highest number of links involving most of the frequency bands during LS and W. Remarkably, this structural reorganization of the integrated brain-organs network is consistent with the sleep-stage stratification patterns observed for each individual organ system, indicating a previously unknown general rule of neural regulation of organ systems.

Organ-Organ Networks

We develop a novel approach to analyze and graphically present the complex behavior of organ-organ interactions. Integrating information obtained from our investigation of brain-organ interactions, we focus on how organ-to-organ interactions are influenced by neural regulation through different brain areas. We combine radar-charts representing the characteristics of brain-organ interactions with the network of links between all organ systems obtained through TDS analysis of the output signals for each pair of organ systems (Fig 18).

We observe that, with transitions from one sleep stage to another there is a pronounced structural reorganization in the topology and links strength of the organ-organ network. This demonstrates a clear association between organ-to-organ network structure and physiologic function of the entire organism. The result in Fig 18 shows how physiologic states influence the dynamics of horizontal integration among organ systems through changing the configuration of links strength in the organ-to-organ network.

Specifically, we find that eye, chin and leg are always strongly connected despite the very different characteristics in their interactions with the brain—i.e., different dominating frequency bands (different color rim of the organ hexagons) and different involvement of the brain areas (different shape of radar-charts in each hexagon) and different overall strength of their network interaction with the brain (different size of the nodes representing each organ), as shown in Fig 18. In contrast, the heart and respiratory system significantly vary their degree of coupling with the rest of network across physiologic states (Fig 18). Further, we note that even when two organ systems predominantly interact with the same brain areas, their coupling strength in the organ-to-organ network can still exhibit a complex transition across different physiologic state—for example, both heart and chin which predominantly interact with Central brain areas, however, the strength of the heart-chin link in the organ network dramatically changes across different sleep stages.

Interestingly, we discover that strong organ-to-organ links often occur between large nodes in the network that represent strong brain-organ interactions, suggesting our TDS network approach captures significant cerebral component in organ-organ interactions. Notably, the reduced link strength of the heart and respiratory system in the organ-to-organ network during LS and DS compared to REM and W is consistent with earlier findings of reduced sympathetic

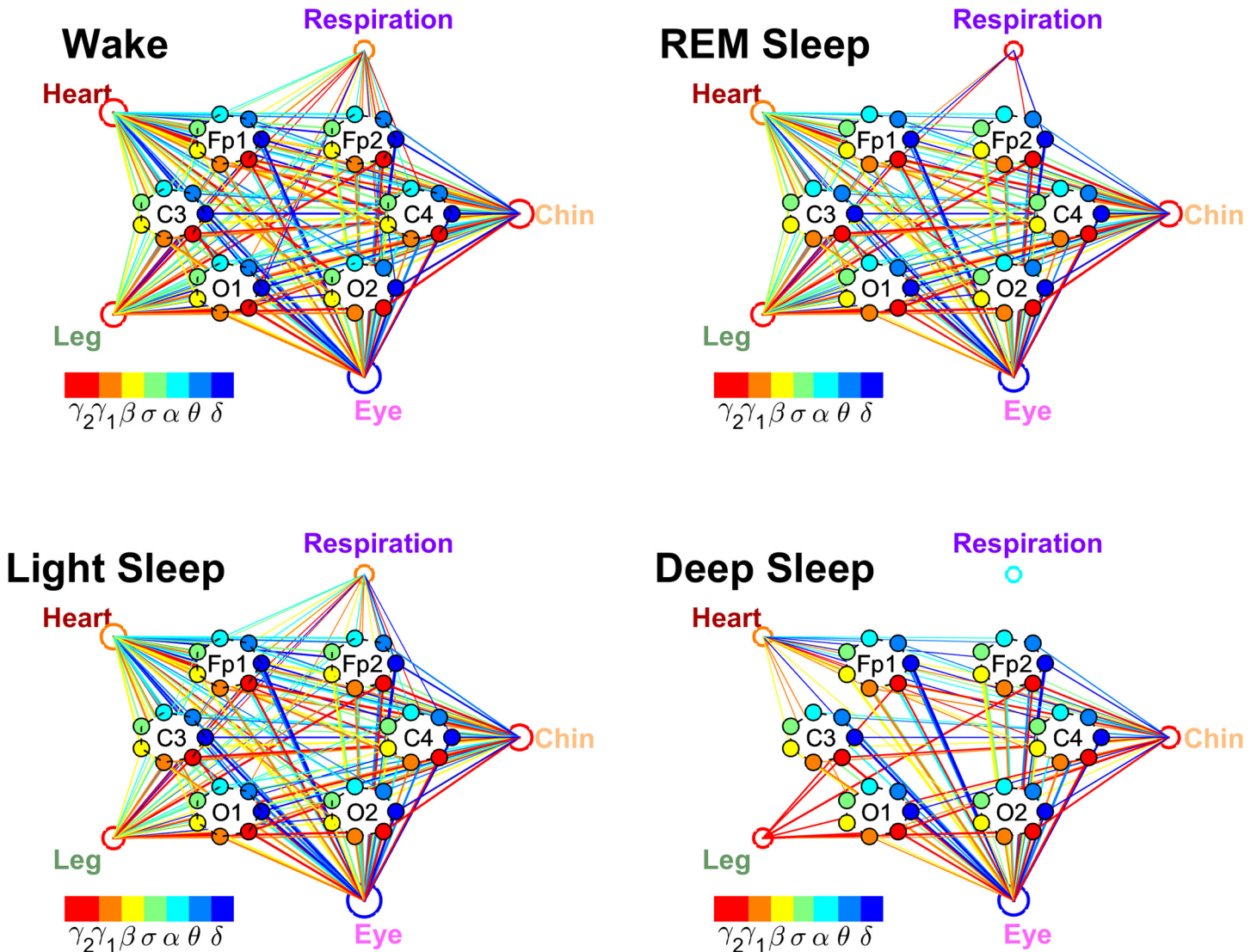


Fig 17. Networks of physiologic interactions between brain areas and key organ systems during different physiologic states. Brain areas are represented by Frontal (Fp1 and Fp2), Central (C3 and C4) and Occipital (O1 and O2) EEG channels. Interactions between brain channels and organ systems are represented by weighted undirected graphs. The size of each organ node in the network is proportional to the strength of the overall brain-organ interaction as measured by the summation of the TDS links strength for all frequency bands and EEG channel locations. The color of each organ node corresponds to the dominant frequency band in the coupling of the organ system with the brain. The width of each link reflects the strength of dynamic coupling as measured by %TDS, and colors of the links correspond to the colors of the nodes representing the different frequency bands (color bars). Plotted are only links with strength $\geq 3\%$ TDS. Thicker links correspond to stronger coupling and higher time delay stability. The physiological network exhibits transitions across sleep stages—lowest number of links during DS, higher during REM, and highest during LS and W. For different organs, brain-organ interactions are mediated through different dominant frequency bands, e.g., the chin and the leg are predominantly coupled to the brain through the high-frequency γ_2 band during all sleep stages whereas brain-eye network interactions are mediated mainly through low-frequency δ band. The complex networks of dynamic interactions between key organ systems and the brain undergoes a hierarchical reorganization across different sleep stages, indicating a previously unknown mechanism of regulation.

doi:10.1371/journal.pone.0142143.g017

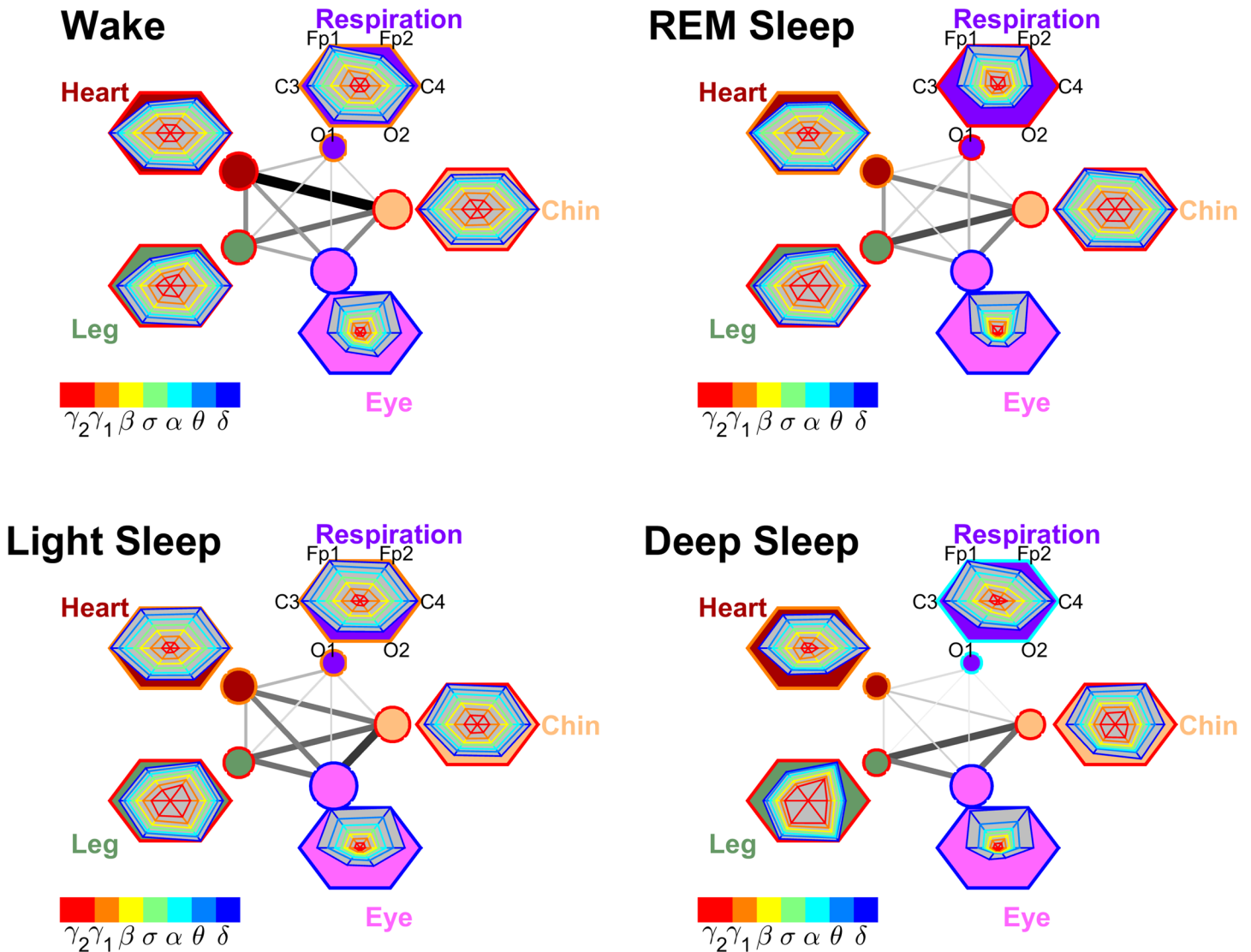


Fig 18. Networks of physiologic interactions among key organ systems during different physiologic states. Interactions among organ systems are represented by weighted undirected graphs, where links reflect the strength of dynamic coupling as measured by %TDS (Section [Methods](#)). Darker and thicker links between organ systems correspond to stronger interaction with higher %TDS. The size of each organ node in the network is proportional to the strength of the overall brain-organ interaction as measured by the summation of the TDS links strength for all frequency bands and EEG channel locations. Hexagons representing individual organs in the networks are obtained in the same way as in Figs [7](#), [9](#), [11](#), [13](#), and [15](#); and are normalized to the same size. Color bar represents different physiologically relevant frequency bands in the EEG spectral power and is used in the radar-charts for the brain-organ interactions shown in each hexagon. The color of each organ node as well as the edge color of the organ hexagon corresponds to the dominant frequency band in the coupling of the organ system with the brain. Notably, larger organ nodes representing stronger brain-organ interactions are consistently connected by stronger organ-organ links (thicker and darker lines). A pronounced re-organization in the configuration of network links strength is observed with transitions from one sleep stage to another, demonstrating a clear association between network structure and physiologic function.

doi:10.1371/journal.pone.0142143.g018

input and corresponding loss of long-range auto-correlation in cardiac and respiratory dynamics during LS and DS [22–25].

Discussion

In summary, we develop a novel analytical method based on the concept of Time Delay Stability, which allows us to identify and quantify network interactions between diverse physiologic systems with very different types of dynamics over a broad range of time scales and where their complex output signals continuously change in response to transitions across physiologic states. By investigating the dynamics of synchronous bursts of activations in neurophysiologic output signals from diverse organ systems we quantify their coupling, and we study dynamical links among systems under different physiologic states. Integrating organ-to-organ interactions into a physiologic network, we are able to probe for the first time how organ systems coordinate and optimize their function to produce distinct physiologic states.

We further develop a novel visualization approach to transform dynamical interactions among organs into network graphs that simultaneously capture several fundamental aspects of the complexity and nature of physiologic coupling. Combining the TDS method and the visualization approach, we obtain first dynamic maps of organ network interactions.

We find that during different physiologic states, the network of organ-to-organ interactions is characterized by different configurations of links and links strength. In addition, we observe that with transition from one physiologic state to another the network of interactions among organ systems undergoes a fast hierarchical reorganization that occurs on time scale from seconds to minutes, indicating a rapid dynamical response to physiologic changes. Our results are first demonstration of direct association between physiologic network topology and physiologic function.

Our investigations led to the discovery of several basic rules of regulation that underlie network dynamics of organ interactions:

1. The brain-brain network is a complex two-layered dynamical network that consists of: (i) an intra-channel sub-network of local (within an EEG channel) communications between different physiologically relevant brain-wave frequency bands, and (ii) an inter-channel sub-network of interactions across different brain areas (Frontal, Central and Occipital) mediated through various frequency bands.

With transitions across physiologic states such as different sleep stages, the brain-brain network undergoes a hierarchical reorganization through a well-structured process involving several building blocks of network configurations. We find that each of these building blocks involves specific types of links, e.g. links across different brain areas mediated by the same frequency band or links between different frequency bands.

Further, we find that the strength of brain-brain network links follows a robust rank order: (a) within a given brain hemisphere, Frontal-Central links are stronger than Central-Occipital, which are stronger than Frontal-Occipital links; (b) across the left and right brain hemispheres, Frontal-Frontal links are stronger than Central-Central, which are stronger than Occipital-Occipital. These rank order is preserved for each sleep stage.

Our statistical analysis of the building blocks in the network of brain-brain interactions reveals a pronounced stratification pattern across sleep stages, i.e. higher network connectivity and average links strength during W and LS, and much lower connectivity and links strength during REM and DS.

2. Networks of brain-organ interactions reveal different involvement of Frontal, Central and Occipital brain areas the regulation of organ systems, and that these network interactions

are predominantly mediated through specific frequency bands.

While the brain-eye networks exhibit strongest links to the Frontal areas, other brain-organ networks are characterized by a spatially symmetric distribution in the coupling strength with different brain areas. Notably, this spatial distribution of coupling strength to different brain areas changes significantly for certain organ systems with transitions across different sleep stages, e.g. brain-respiration network, whereas other brain-organ networks exhibit stable spatial distribution of network links strength to different brain areas.

We discover that in its communication with the brain each organ has its own frequency profile, representing the relative strength of brain-organ links mediated through the different frequency bands. For some organs, these frequency profiles are characterized by the presence of a dominant frequency—e.g., strongest links in the brain-leg network are mediated through the highest-frequency γ band, while the strongest links in the brain-eye network are mediated through the lowest-frequency δ band. In contrast, other organ systems have relatively uniform (flat) frequency profiles such as the brain-respiratory network.

For all brain-organ networks the organ-specific frequency profiles are consistently observed for each subgroup of network links to the Frontal, Central and Occipital brain areas. Further, we find that these frequency profiles remain stable with transitions across sleep stages (with the exception of brain-heart network).

3. For both brain-brain and brain-organ networks, we find a remarkable symmetry between the left and right brain hemispheres in both network topology and the configuration of links strength.
4. We find a very robust sleep-stage stratification pattern for all brain-brain, brain-organ and organ-organ networks—more and stronger links during W and LS, and less and weaker links during REM and DS. Further, in all these networks, the sleep-stage stratification is consistently observed for all subgroups of network links related to the Frontal, Central and Occipital areas. Moreover, this sleep-stage stratification pattern is stable even when we consider only links that are mediated through a single frequency band.
5. Our results demonstrate a direct association between network topology and physiologic function. We uncover new basic principles of how physiologic networks reorganize in response to well defined physiologic states. The network behavior we find is universal, since it is observed for every healthy subject in the database we analyzed, and thus points to a new previously unknown regulatory mechanism that underlies the dynamics of organ interactions.

These findings are first steps in understanding how organ systems synchronize and coordinate their output dynamics as a network to produce distinct physiologic functions. Our investigations reveal basic rules that underlie (i) the dynamics of network interactions among organ systems, and (ii) the hierarchical reorganization of organ network interactions in response to changes in physiologic state. To our knowledge, this is the first report on how an entire network of diverse dynamical systems hierarchically reorganizes its structure in real time to facilitate distinct functions. The presented here findings and visualization maps are initial steps in building the first atlas of dynamic interactions among organ systems.

Acknowledgments

We acknowledge support from W. M. Keck Foundation, National Institutes of Health (NIH Grant 1R01-HL098437), the Office of Naval Research (ONR Grant 000141010078), the US-Israel Binational Science Foundation (BSF Grant 2012219), EC- FP7 Marie Curie Fellowship (IIF 628159).

Author Contributions

Conceived and designed the experiments: RB KL AB PI. Performed the experiments: RB AB PI. Analyzed the data: RB KL AB PI. Contributed reagents/materials/analysis tools: RB KL AB PI. Wrote the paper: RB KL PI.

References

1. Bashan A, Bartsch RP, Kantelhardt JW, Havlin S, Ivanov PCh. Network physiology reveals relations between network topology and physiological function. *Nat Commun.* 2012; 3:702. doi: [10.1038/ncomms1705](https://doi.org/10.1038/ncomms1705) PMID: [22426223](https://pubmed.ncbi.nlm.nih.gov/22426223/)
2. Ivanov PCh, Bartsch RP. Network Physiology: Mapping Interactions Between Networks of Physiologic Networks. In: D'Agostino G, Scala A, editors. *Networks of Networks: The Last Frontier of Complexity*. Springer International Publishing; 2014. p. 203–222.
3. Quill E. When Networks Network. *Science News.* 2012; 182(6):18–25. doi: [10.1002/scin.5591820619](https://doi.org/10.1002/scin.5591820619)
4. Arodz T, Bonchev D. Identifying influential nodes in a wound healing-related network of biological processes using mean first-passage time. *New Journal of Physics.* 2015; 17(2):025002. doi: [10.1088/1367-2630/17/2/025002](https://doi.org/10.1088/1367-2630/17/2/025002)
5. Rothkegel A, Lehnertz K. Irregular macroscopic dynamics due to chimera states in small-world networks of pulse-coupled oscillators. *New Journal of Physics.* 2014; 16(5):055006. doi: [10.1088/1367-2630/16/5/055006](https://doi.org/10.1088/1367-2630/16/5/055006)
6. Fernandes HM, Van Hartevelt TJ, Boccard SG, Owen SL, Cabral J, Deco G, et al. Novel fingerprinting method characterises the necessary and sufficient structural connectivity from deep brain stimulation electrodes for a successful outcome. *New Journal of Physics.* 2015; 17(1):015001. doi: [10.1088/1367-2630/17/1/015001](https://doi.org/10.1088/1367-2630/17/1/015001)
7. Muller L, Destexhe A, Rudolph-Lilith M. Brain networks: small-worlds, after all? *New Journal of Physics.* 2014; 16(10):105004. doi: [10.1088/1367-2630/16/10/105004](https://doi.org/10.1088/1367-2630/16/10/105004)
8. Mosqueiro T, de Lecea L, Huerta R. Control of sleep-to-wake transitions via fast amino acid and slow neuropeptide transmission. *New Journal of Physics.* 2014; 16:115010. doi: [10.1088/1367-2630/16/11/115010](https://doi.org/10.1088/1367-2630/16/11/115010) PMID: [25598695](https://pubmed.ncbi.nlm.nih.gov/25598695/)
9. Oliveira CL, Bates JH, Suki B. A network model of correlated growth of tissue stiffening in pulmonary fibrosis. *New Journal of Physics.* 2014; 16(6):065022. doi: [10.1088/1367-2630/16/6/065022](https://doi.org/10.1088/1367-2630/16/6/065022) PMID: [25484613](https://pubmed.ncbi.nlm.nih.gov/25484613/)
10. Bartsch RP, Ivanov PCh. Coexisting Forms of Coupling and Phase-Transitions in Physiological Networks. *Communications in Computer and Information Science.* 2014; 438:270–287. doi: [10.1007/978-3-319-08672-9_33](https://doi.org/10.1007/978-3-319-08672-9_33)
11. Faes L, Nollo G, Jurysta F, Marinazzo D. Information dynamics of brain–heart physiological networks during sleep. *New Journal of Physics.* 2014; 16:105005. doi: [10.1088/1367-2630/16/10/105005](https://doi.org/10.1088/1367-2630/16/10/105005)
12. Piper D, Schiecke K, Pester B, Benninger F, Feucht M, Witte H. Time-variant coherence between heart rate variability and EEG activity in epileptic patients: an advanced coupling analysis between physiological networks. *New Journal of Physics.* 2014; 16(11):115012. doi: [10.1088/1367-2630/16/11/115012](https://doi.org/10.1088/1367-2630/16/11/115012)
13. Scala A, Auconi P, Scaccocchio M. Complex networks for data-driven medicine: the case of Class III dentoskeletal disharmony. *New Journal of Physics.* 2014; 16:115017. doi: [10.1088/1367-2630/16/11/115017](https://doi.org/10.1088/1367-2630/16/11/115017)
14. Liu KKL, Bartsch RP, Ma QDY, Ivanov PCh. Major component analysis of dynamic networks of physiologic organ interactions. *Journal of Physics: Conference Series.* 2015; 640(1):012013. Available from: <http://stacks.iop.org/1742-6596/640/i=1/a=012013>
15. Traxl D, Boers N, Kurths J. General scaling of maximum degree of synchronization in noisy complex networks. *New Journal of Physics.* 2014; 16(11):115009. doi: [10.1088/1367-2630/16/11/115009](https://doi.org/10.1088/1367-2630/16/11/115009)
16. Stankovski T, Ticcinielli V, McClintock PVE, Stefanovska A. Coupling functions in networks of oscillators. *New Journal of Physics.* 2015; 17:035002. doi: [10.1088/1367-2630/17/3/035002](https://doi.org/10.1088/1367-2630/17/3/035002)
17. Stramaglia S, Cortes JM, Marinazzo D. Synergy and redundancy in the Granger causal analysis of dynamical networks. *New Journal of Physics.* 2014; 16:105003. doi: [10.1088/1367-2630/16/10/105003](https://doi.org/10.1088/1367-2630/16/10/105003)
18. West BJ, Turalska M, Grigolini P. Fractional calculus ties the microscopic and macroscopic scales of complex network dynamics. *New Journal of Physics.* 2015; 17:045009. doi: [10.1088/1367-2630/17/4/045009](https://doi.org/10.1088/1367-2630/17/4/045009)
19. Karasik R, Sapir N, Ashkenazy Y, Ivanov PCh, Dvir I, Lavie P, et al. Correlation differences in heartbeat fluctuations during rest and exercise. *Phys Rev E.* 2002; 66(6):062902. doi: [10.1103/PhysRevE.66.062902](https://doi.org/10.1103/PhysRevE.66.062902)

20. Ivanov PCh, Bunde A, Amaral LAN, Havlin S, Fritsch-Yelle J, Baevsky RM, et al. Sleep-wake differences in scaling behavior of the human heartbeat: analysis of terrestrial and long-term space flight data. *Europhys Lett.* 1999; 48(5):594–600. doi: [10.1209/epl/i1999-00525-0](https://doi.org/10.1209/epl/i1999-00525-0) PMID: [11542917](https://pubmed.ncbi.nlm.nih.gov/11542917/)
21. Bunde A, Havlin S, Kantelhardt JW, Penzel T, Peter JH, Voigt K. Correlated and Uncorrelated Regions in Heart-Rate Fluctuations during Sleep. *Phys Rev Lett.* 2000 Oct; 85(17):3736–3739. doi: [10.1103/PhysRevLett.85.3736](https://doi.org/10.1103/PhysRevLett.85.3736) PMID: [11030994](https://pubmed.ncbi.nlm.nih.gov/11030994/)
22. Kantelhardt JW, Ashkenazy Y, Ivanov PCh, Bunde A, Havlin S, Penzel T, et al. Characterization of sleep stages by correlations in the magnitude and sign of heartbeat increments. *Phys Rev E.* 2002; 65(5):051908. doi: [10.1103/PhysRevE.65.051908](https://doi.org/10.1103/PhysRevE.65.051908)
23. Kantelhardt JW, Havlin S, Ivanov PCh. Modeling transient correlations in heartbeat dynamics during sleep. *Europhys Lett.* 2003; 62(2):147–153. doi: [10.1209/epl/i2003-00332-7](https://doi.org/10.1209/epl/i2003-00332-7)
24. Schmitt DT, Stein PK, Ivanov PCh. Stratification pattern of static and scale-invariant dynamic measures of heartbeat fluctuations across sleep stages in young and elderly. *IEEE Trans Biomed Eng.* 2009 May; 56(5):1564–1573. doi: [10.1109/TBME.2009.2014819](https://doi.org/10.1109/TBME.2009.2014819) PMID: [19203874](https://pubmed.ncbi.nlm.nih.gov/19203874/)
25. Schumann AY, Bartsch RP, Penzel T, Ivanov PCh, Kantelhardt JW. Aging effects on cardiac and respiratory dynamics in healthy subjects across sleep stages. *Sleep.* 2010 Jul; 33(7):943–955. PMID: [20614854](https://pubmed.ncbi.nlm.nih.gov/20614854/)
26. Hu K, Ivanov PCh, Hilton MF, Chen Z, Ayers RT, Stanley HE, et al. Endogenous circadian rhythm in an index of cardiac vulnerability independent of changes in behavior. *Proc Natl Acad Sci USA.* 2004; 101(52):18223–18227. doi: [10.1073/pnas.0408243101](https://doi.org/10.1073/pnas.0408243101) PMID: [15611476](https://pubmed.ncbi.nlm.nih.gov/15611476/)
27. Ivanov PCh, Hu K, Hilton MF, Shea SA, Stanley HE. Endogenous circadian rhythm in human motor activity uncoupled from circadian influences on cardiac dynamics. *Proc Natl Acad Sci USA.* 2007 Dec; 104(52):20702–20707. doi: [10.1073/pnas.0709957104](https://doi.org/10.1073/pnas.0709957104) PMID: [18093917](https://pubmed.ncbi.nlm.nih.gov/18093917/)
28. Ivanov PCh. Scale-invariant aspects of cardiac dynamics—Observing sleep stages and circadian phases [Article]. *IEEE Eng Med Biol.* 2007 NOV-DEC; 26(6):33–37. doi: [10.1109/EMB.2007.907093](https://doi.org/10.1109/EMB.2007.907093)
29. Rechtschaffen A, Kales A. A manual of standardized terminology, techniques and scoring system for sleep stages of human subjects. Bethesda, MD: U.S. Dept. of Health, Education, and Welfare; 1968.
30. Klösch G, Kemp B, Penzel T, Schlögl A, Rappelsberger P, Trenker E, et al. The SIESTA project polygraphic and clinical database. *IEEE Eng Med Biol Mag.* 2001; 20(3):51–57. doi: [10.1109/51.932725](https://doi.org/10.1109/51.932725) PMID: [11446210](https://pubmed.ncbi.nlm.nih.gov/11446210/)
31. Hegger R, Bunner MJ, Kantz H, Giaquinta A. Identifying and modeling delay feedback systems. *Phys Rev Lett.* 1998 JUL 20; 81(3):558–561. doi: [10.1103/PhysRevLett.81.558](https://doi.org/10.1103/PhysRevLett.81.558)
32. Bartsch RP, Liu KKL, Ma QDY, Ivanov PCh. Three Independent Forms of Cardio-Respiratory Coupling: Transitions across Sleep Stages. *Computing in Cardiology.* 2014; 41:781–784. PMID: [25664348](https://pubmed.ncbi.nlm.nih.gov/25664348/)



Free Full Text from Publisher



Save to EndNote online

Add to Marked List

116 of 127

Network Physiology: How Organ Systems Dynamically Interact

By: Bartsch, RP (Bartsch, Ronny P.)^[1,2]; Liu, KKL (Liu, Kang K. L.)^[2,3,4]; Bashan, A (Bashan, Amir)^[4,5]; Ivanov, PC (Ivanov, Plamen Ch.)^[2,4,6,7]

[View ResearcherID and ORCID](#)

PLOS ONE

Volume: 10 **Issue:** 11

Article Number: e0142143

DOI: 10.1371/journal.pone.0142143

Published: NOV 10 2015

Document Type: Article

[View Journal Impact](#)

Abstract

We systematically study how diverse physiologic systems in the human organism dynamically interact and collectively behave to produce distinct physiologic states and functions. This is a fundamental question in the new interdisciplinary field of Network Physiology, and has not been previously explored. Introducing the novel concept of Time Delay Stability (TDS), we develop a computational approach to identify and quantify networks of physiologic interactions from long-term continuous, multi-channel physiological recordings. We also develop a physiologically-motivated visualization framework to map networks of dynamical organ interactions to graphical objects encoded with information about the coupling strength of network links quantified using the TDS measure. Applying a system-wide integrative approach, we identify distinct patterns in the network structure of organ interactions, as well as the frequency bands through which these interactions are mediated. We establish first maps representing physiologic organ network interactions and discover basic rules underlying the complex hierarchical reorganization in physiologic networks with transitions across physiologic states. Our findings demonstrate a direct association between network topology and physiologic function, and provide new insights into understanding how health and distinct physiologic states emerge from networked interactions among nonlinear multi-component complex systems. The presented here investigations are initial steps in building a first atlas of dynamic interactions among organ systems.

Keywords

Keywords Plus: ENDOGENOUS CIRCADIAN-RHYTHM; CARDIAC DYNAMICS; SLEEP STAGES; HEARTBEAT; BEHAVIOR

Author Information

Reprint Address: Ivanov, PC (reprint author)

+ Boston Univ, Dept Phys, 590 Commonwealth Ave, Boston, MA 02215 USA.

Addresses:

+ [1] Bar Ilan Univ, Dept Phys, IL-52900 Ramat Gan, Israel

+ [2] Boston Univ, Dept Phys, Boston, MA 02215 USA

+ [3] Beth Israel Deaconess Med Ctr, Dept Neurol, Boston, MA 02115 USA

+ [4] Harvard Univ, Sch Med, Boston, MA 02115 USA

+ [5] Brigham & Womens Hosp, Channing Div Network Med, Boston, MA 02115 USA

Citation Network

In Web of Science Core Collection

32

Times Cited

Create Citation Alert

All Times Cited Counts

32 in All Databases

[See more counts](#)

32

Cited References

[View Related Records](#)

Most recently cited by:

Li, Xinwei; Li, Qionglng; Wang, Xuetong; et al.

[Differential Age-Related Changes in Structural Covariance Networks of Human Anterior and Posterior Hippocampus.](#)
FRONTIERS IN PHYSIOLOGY (2018)

Martin-Gonzalez, Sofia; Navarro-Mesa, Juan L.; Julia-Serda, Gabriel; et al.

[Improving the understanding of sleep apnea characterization using Recurrence Quantification Analysis by defining overall acceptable values for the dimensionality of the system, the delay, and the distance threshold.](#)
PLOS ONE (2018)

[View All](#)

Use in Web of Science

Web of Science Usage Count

1

18

Last 180 Days

Since 2013

[Learn more](#)

This record is from:

+ [6] Brigham & Womens Hosp, Div Sleep Med, Boston, MA 02115 USA

+ [7] Bulgarian Acad Sci, Inst Solid State Phys, BU-1784 Sofia, Bulgaria

E-mail Addresses: plamen@buphy.bu.edu

Funding

Funding Agency	Grant Number
W. M. Keck Foundation	
National Institutes of Health	1R01-HL098437
Office of Naval Research	000141010078
US-Israel Binational Science Foundation	2012219
EC-FP7 Marie Curie Fellowship	IIF 628159

[View funding text](#)

Publisher

PUBLIC LIBRARY SCIENCE, 1160 BATTERY STREET, STE 100, SAN FRANCISCO, CA 94111 USA

Journal Information

Impact Factor: [Journal Citation Reports](#)

Categories / Classification

Research Areas: Science & Technology - Other Topics

Web of Science Categories: Multidisciplinary Sciences

[See more data fields](#)

Web of Science Core Collection

View Record in Other Databases:

[View biological data](#) (in Biological Abstracts)

[View medical data](#) (in MEDLINE®)

Suggest a correction

If you would like to improve the quality of the data in this record, please [suggest a correction](#).

◀ 116 of 127 ▶

Cited References: 32

Showing 30 of 32 [View All in Cited References page](#)

(from Web of Science Core Collection)

- Identifying influential nodes in a wound healing-related network of biological processes using mean first-passage time** **Times Cited: 4**

By: Arodz, Tomasz; Bonchev, Danail
 NEW JOURNAL OF PHYSICS Volume: 17 Article Number: 025002 Published: FEB 4 2015
- Three Independent Forms of Cardio-Respiratory Coupling: Transitions across Sleep Stages** **Times Cited: 11**

By: Bartsch, Ronny P.; Liu, Kang K. L.; Ma, Qianli D. Y.; et al.
 2014 COMPUTING IN CARDIOLOGY CONFERENCE (CINC), VOL 41 Book Series: Computing in Cardiology Series Volume: 41
 Pages: 781-784 Published: 2014
- Coexisting Forms of Coupling and Phase-Transitions in Physiological Networks** **Times Cited: 20**

By: Bartsch, Ronny P.; Ivanov, Plamen Ch.
 NONLINEAR DYNAMICS OF ELECTRONIC SYSTEMS Book Series: Communications in Computer and Information Science
 Volume: 438 Pages: 270-287 Published: 2014
- Network physiology reveals relations between network topology and physiological function** **Times Cited: 192**

By: Bashan, Amir; Bartsch, Ronny P.; Kantelhardt, Jan. W.; et al.
 NATURE COMMUNICATIONS Volume: 3 Article Number: 702 Published: FEB 2012

Research



Cite this article: Lin A, Liu KKL, Bartsch RP, Ivanov PCh. 2016 Delay-correlation landscape reveals characteristic time delays of brain rhythms and heart interactions. *Phil. Trans. R. Soc. A* **374**: 20150182.
<http://dx.doi.org/10.1098/rsta.2015.0182>

Accepted: 26 February 2016

One contribution of 16 to a theme issue 'Uncovering brain–heart information through advanced signal and image processing.'

Subject Areas:

biomedical engineering, biophysics, complexity, medical physics, statistical physics

Keywords:

brain–heart interactions, time-delay analysis, delay-correlation landscape, Network Physiology

Author for correspondence:

Plamen Ch. Ivanov
e-mail: plamen@buphy.bu.edu

Electronic supplementary material is available at <http://dx.doi.org/10.1098/rsta.2015.0182> or via <http://rsta.royalsocietypublishing.org>.

Delay-correlation landscape reveals characteristic time delays of brain rhythms and heart interactions

Aijing Lin^{1,2}, Kang K. L. Liu^{2,3}, Ronny P. Bartsch⁴ and Plamen Ch. Ivanov^{2,5,6}

¹Department of Mathematics, School of Science, Beijing Jiaotong University, Beijing 100044, People's Republic of China

²Keck Laboratory for Network Physiology, Department of Physics, Boston University, Boston, MA 02215, USA

³Department of Neurology, Beth Israel Deaconess Medical Center, Harvard Medical School, Boston, MA 02215, USA

⁴Department of Physics, Bar-Ilan University, Ramat Gan, 5290002, Israel

⁵Division of Sleep Medicine, Brigham and Women's Hospital, Harvard Medical School, Boston, MA 02115, USA

⁶Institute of Solid State Physics, Bulgarian Academy of Sciences, Sofia, 1784, Bulgaria

Within the framework of 'Network Physiology', we ask a fundamental question of how modulations in cardiac dynamics emerge from networked brain–heart interactions. We propose a generalized time-delay approach to identify and quantify dynamical interactions between physiologically relevant brain rhythms and the heart rate. We perform empirical analysis of synchronized continuous EEG and ECG recordings from 34 healthy subjects during night-time sleep. For each pair of brain rhythm and heart interaction, we construct a delay-correlation landscape (DCL) that characterizes how individual brain rhythms are coupled to the heart rate, and how modulations in brain and cardiac dynamics are coordinated in time. We uncover characteristic time delays and an ensemble of specific profiles for the probability distribution of time delays that underly brain–heart interactions. These profiles are consistently observed in all subjects, indicating a universal pattern. Tracking the evolution of DCL across different sleep stages, we find

that the ensemble of time-delay profiles changes from one physiologic state to another, indicating a strong association with physiologic state and function. The reported observations provide new insights on neurophysiological regulation of cardiac dynamics, with potential for broad clinical applications. The presented approach allows one to simultaneously capture key elements of dynamic interactions, including characteristic time delays and their time evolution, and can be applied to a range of coupled dynamical systems.

1. Introduction

As an integrated physiologic system under neural regulation, the cardiac system exhibits complex behaviour characterized by continuous fluctuations and transient, nonlinear and scale-invariant temporal dynamics. Reflecting modulation in neural autonomic control and sympatho-vagal balance [1–4], the linear and nonlinear characteristics of cardiac dynamics [5–7] change with sleep–wake cycle [8,9], across circadian phases [10] and sleep-stage transitions [11–13]. Various measures derived from linear and nonlinear characteristics of cardiac dynamics have been established as robust biomarkers for diagnosis and prognosis under a broad range of conditions [14,15], young versus elderly [16,17] and under pathological perturbations [18–23]. To account for these extensive empirical observations, modelling approaches have been developed (i) to investigate the underlying mechanisms of neuroautonomic control and associated nonlinear feedback loops acting on a wide range of time scales, and (ii) to study how these mechanisms change across different physiologic states and conditions [24].

Despite the importance of understanding the basic mechanisms of neural regulation of organ systems, it is not well understood how the brain and the cardiac system dynamically interact and coordinate their functions to generate a variety of physiologic states. Specifically, the role of different brain rhythms and their temporal dynamics in mediating brain–heart communications remains an open question.

Probing dynamics of brain–heart interactions is a major challenge due to several levels of complexity. At the individual systems level: the heart and the brain are very different integrated systems, each with its own structural and functional complexity, leading to output dynamics with distinct characteristics, i.e. the cardiac system exhibits a pronounced oscillatory pattern on the scale of seconds, whereas brain dynamics are characterized by multiple rhythms with different origins and functions that operate on much shorter time scales. At the level of pairwise interactions: physiological systems often interact through multiple forms of coupling, which are of transient nature, can switch on/off, and can simultaneously coexist [25–29]. In the context of brain–heart communications [30], synchronization [31–33], coherence [34], time delay [35,36] and information transfer [37,38] play important roles. At the organism level where dynamical networks of diverse organ systems are essential: integrated physiologic function emerges as a global phenomenon from hierarchical networks representing the dynamical interactions among organ systems, and cannot be simply described by summing up the behaviours of individual systems.

Within the framework of ‘Network Physiology’ [36,39,40], using the concept of time-delay stability (TDS), recent work [26,40] has demonstrated that the cardiac system communicates with the brain not only through one but rather through multiple brain rhythms simultaneously. Further, empirical analyses have shown that, during different physiologic states, brain–heart communications are predominantly mediated through different brain rhythms, where patterns of brain–heart networked interactions depend on brain locations, and undergo complex hierarchical reorganization with transitions across physiologic states [40].

To quantify brain–heart interactions, here we extend the TDS approach [36,40–42] and we propose a generalized time-delay analysis based on the novel concept of delay-correlation landscape (DCL) to investigate coordination of bursting activities in the brain and heart output signals. We hypothesize that key properties of the brain–heart DCL reflect changes in neuroautonomic control of cardiac and brain dynamics associated with distinct physiologic

states such as sleep or wake and different sleep stages. Specifically, we hypothesize that the characteristic time delays and directionality of brain–heart communications between each physiologically relevant brain rhythm and cardiac output dynamics exhibit unique signature profiles reflecting physiologic function during distinct physiologic states.

2. Material and methods

(a) Data

We analyse continuously recorded multichannel physiological data obtained from 34 healthy young subjects (17 female, 17 male, with ages between 20 and 40, average 29 years) during night-time sleep [43] (average record duration is 7.8 h). This allows us to track the dynamics and evolution of brain–heart interactions during different sleep stages and sleep-stage transitions. We focus on physiological dynamics during sleep as sleep stages are well-defined physiological states, and external influences due to physical activity or sensory inputs are reduced during sleep. Sleep stages are scored in 30 s epochs by sleep laboratory technicians based on standard criteria [43,44]. In particular, we focus on the electroencephalogram (EEG) and the electrocardiogram (ECG). To compare these very different signals with each other and to study interrelations between them, we extract the following time series from the raw signals: the spectral power of five physiologically relevant frequency bands of the EEG, derived from the central C3 channel, in moving windows of 2 s with a 1 s overlap (namely δ wave (0.5–3.5 Hz), θ wave (4–7.5 Hz), α wave (8–11.5 Hz), σ wave (12–15.5 Hz) and β wave (16–19.5 Hz)); heartbeat RR intervals are re-sampled to 1 Hz (1 s bins) after which values are inverted to obtain the instantaneous heart rate (HR). Thus, all time series have the same time resolution of 1 s before our analyses are applied.

We calculate the fast Fourier transform (FFT) in 2 s EEG windows and determine the spectral power in the EEG frequency bands mentioned above. As there is a problem of power leakage from one frequency bin to others, we taper the window by a Hann function, and because tapering itself introduces the problem of weighting the edge of the windows much less than the data in the middle, we choose an overlap of half the window length, i.e. 1 s. According to Press *et al.* [45], tapering and choosing an overlap that is half the window length resolves the problems of power leakage and different weights, respectively. Because we are analysing EEG data that were recorded during sleep, we use the five EEG band definitions that are commonly accepted in sleep medicine [46] as defined above. We originally extended the definition for β to include ‘high β waves’ (20–30 Hz); however, we noted that, past 20 Hz, the EEG is more susceptible to electromyography (EMG) movement artefacts, and therefore we chose the traditional 16–19.5 Hz frequency band.

The ECG data are analysed and annotated by a semi-automatic R-peak detector (see below). EEG recordings were filtered by a high-pass filter (0–0.4 Hz) and a low-pass filter (30–70 Hz). We apply the high-pass filter in this range to filter out slow movement artefacts without much affecting δ frequencies. The low-pass filter filters out high-frequency artefacts (e.g. from EMG). In addition, the EEG recording device had a 50 Hz notch filter. R-peaks are extracted from the ECG data using the semi-automatic peak detector Raschlab developed by the cardiology group of Klinikum Rechts der Isar, Munich, Germany (R. Schneider. Open source toolbox for handling cardiologic data, available on the internet: www.librasch.org). A beat classification (normal beat, ventricular beat, artefact) is assigned to each R-peak by the detector. Then we calculate the series of RR time intervals between each pair of consecutive heartbeats and obtain the HR time series by inverting the RR series. Ectopic beats and artefacts are detected by Raschlab. Additionally, we examine more carefully the obtained RR intervals and exclude RR intervals from our calculations, if (i) the beat at the beginning or at the end of the interval is not normal, (ii) the calculated interval is shorter than 330 ms or longer than 2000 ms or (iii) the interval is more than 30% shorter or more than 60% longer than the preceding interval. The purpose of the last filter is to eliminate extrasystoles and ectopic beats unnoticed by the peak detector. This procedure led to $\approx 1\%$ removal of original ECG RR intervals and corresponding $\approx 1\%$ reduction in the original EEG data.

One potential approach to study brain–heart interaction mediated by different brain rhythms is to use the absolute spectral power in each EEG frequency band. However, our preliminary results (not shown) indicate that the bursting activity in HR is strongly modulated by trends in the total EEG power within the frequency range of 0.5–19.5 Hz (sum of all five frequency bands)—a masking effect leading to very similar results for each pair of HR and brain rhythm interaction. In order to eliminate this masking effect and to isolate spurious synchronization among all brain rhythms caused by modulations in the total EEG spectral power, we use normalized (relative) spectral power in our analyses. First, we calculate the time series of the total power of EEG (S_{EEG}) as the sum of all spectral powers from the five frequency bands listed above. Next, we obtain the relative spectral power in each frequency band with a 1 s resolution. The relative spectral power ($S_{\delta}(t), S_{\theta}(t), S_{\alpha}(t), S_{\sigma}(t), S_{\beta}(t)$) is obtained as the ratio between the spectral power in the specific frequency band and the total spectral power of all five bands. Thus, the obtained normalized relative spectral power represents the relative contribution of each brain rhythm to the total brain activity, and allows one to investigate the individual role of each brain rhythm in facilitating brain–heart communications.

(b) Generalized time-delay analysis and delay-correlation landscape

The TDS method proposed in earlier studies [36,40,41] focuses on the time evolution and stability of the time delay defined as the time shift corresponding to maximum degree of correlation/anti-correlation between two signals. While the percentage of data segments exhibiting time-delay stability (%TDS) was found to have important physiological relevance, as it undergoes a pronounced transition from one physiologic state to another, it does not provide information on the type of correlation (positive or negative) and directionality of interaction based on the sign of the time delay.

To address these limitations and to further quantify the dynamical aspects of brain–heart interaction, we extend our TDS methodology to a more generalized time-delay analysis framework, which keeps track of both the time t evolution of cross-correlation C as well as the time shift τ dependence of the cross-correlation, i.e. $C(t, \tau)$.

As shown in figure 1, for each time window t with size $L = 30$ s, we obtain the Spearman cross-correlation as a function C_{xy} of the time shift $\tau \in [-30, 30]$ between two signals x and y , where r_x and r_y represent the ranks of the values in the signals x and y , respectively. The functional form of $C_{xy}(t, \tau)$ can be written as:

$$C_{xy}(t, \tau) \equiv \frac{\sum_{i=1}^L [r_x(t+i) - \bar{r}_x][r_y(t+\tau+i) - \bar{r}_y]}{\sqrt{\sum_j^L [r_x(t+j) - \bar{r}_x]^2} \sqrt{\sum_k^L [r_y(t+\tau+k) - \bar{r}_y]^2}} \quad (2.1)$$

$$= 1 - \frac{6 \sum_{i=1}^L [r_x(t+i) - r_y(t+\tau+i)]^2}{L(L^2 - 1)}, \quad (2.2)$$

where $\bar{r}_x = \bar{r}_y = (L + 1)/2$. At each time step t , we shift the 30 s window of the HR (signal y) relatively to the 30 s window of EEG spectral power (signal x) in steps of 1 s, and calculate the cross-correlation as a function of the relative time shift τ (vertical axis in figure 1). $C_{xy}(t, \tau)$ forms a DCL as shown in figure 1c that represents the time evolution of cross-correlation for different choices of time shift τ between two signals.

Theoretically, the DCL contains the information provided by both the traditional cross-correlation analysis and the original TDS method [36,40,41]. The cross-section of DCL along the black dashed line $\tau = 0$ in figure 1c represents the cross-correlation of the two signals without any time shift, i.e. $C_{xy}(t)|_{\tau=0}$. Black triangle symbols in figure 1c mark the evolution of time delay defined in the original TDS method as the time shift between the two signals at which the maximum in the absolute value of cross-correlation is observed, i.e. $\tau(t)|_{\max|C_{xy}|}$. The DCL reveals a more comprehensive picture of the dynamic interaction between two signals as represented by a heterogeneous landscape within which red ‘hills’ (positive correlation, $C > 0$) and blue ‘valleys’ (negative correlation, $C < 0$) form a complex mixture.

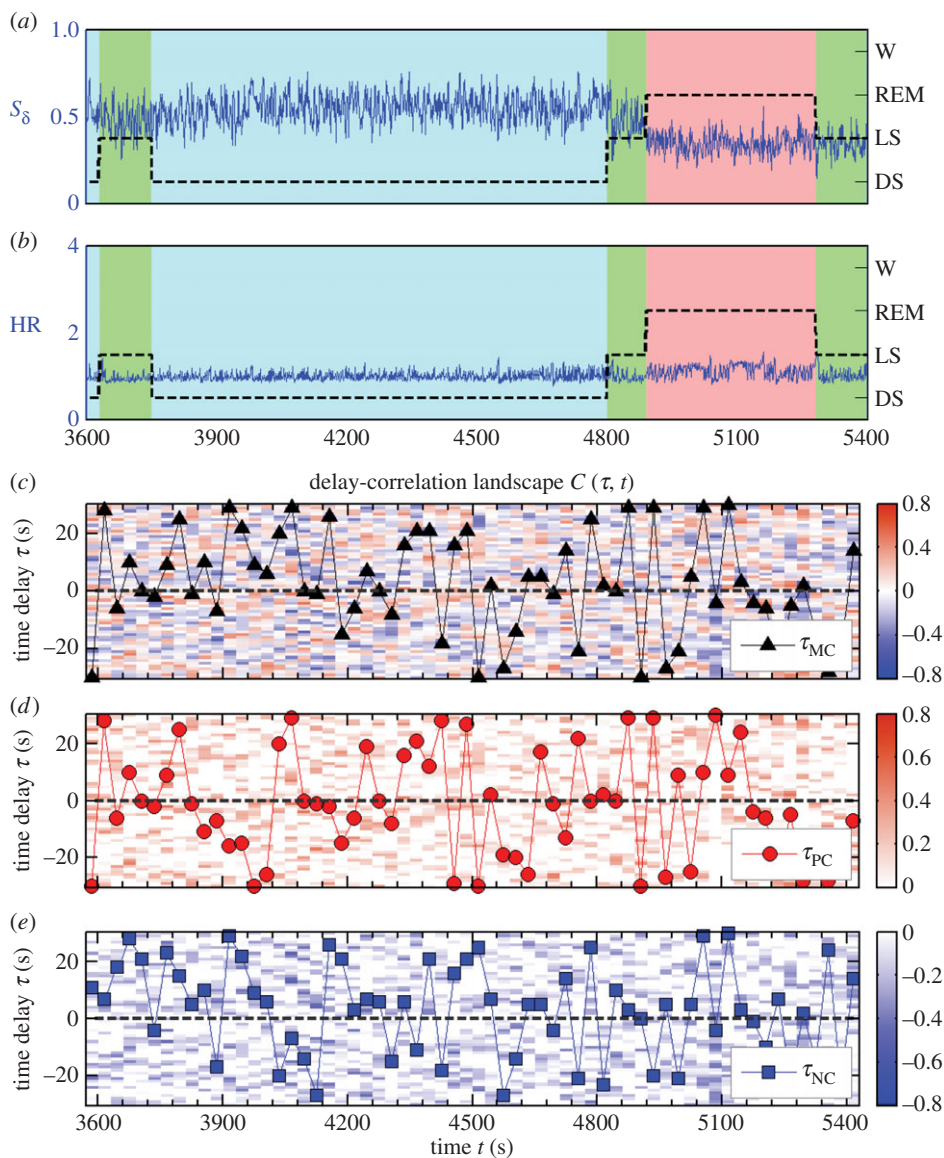


Figure 1. Generalized time-delay analysis and delay-correlation landscape. (a) Normalized spectral power S_{δ} of δ brain rhythm (0.5–4 Hz) derived from EEG recording at the central C3 channel (C3–M2 set-up), and (b) heart rate (HR) from a healthy subject during 30 min of night-time sleep. Black dashed lines and background colours in (a) and (b) represent sleep stages (denoted on the right vertical axis) as defined by traditional sleep-stage scoring criteria [43,44]. (c) Spearman cross-correlation function $C_{\delta,HR}(\tau, t)$ between S_{δ} and heart rate (HR) are obtained in 30 s windows moving with a step of 30 s and plotted as delay-correlation landscape (colour map). Horizontal axis t indicates the time corresponding to the centre of the two aligned 30 s windows used for the cross-correlation calculation. At each time step t , we shift the 30 s window of the HR relatively to the 30 s window of EEG spectral power, and calculate the cross-correlation as a function of the relative time shift τ (vertical axis): $\tau > 0$ when the 30 s window for brain rhythm signal precedes the window of cardiac signal and vice versa for $\tau < 0$. Colour of the delay-correlation landscape (DCL) represents the value of cross-correlation: red corresponds to positive correlation $C > 0$ and blue corresponds to negative correlation $C < 0$. Black triangle symbols in (c) mark the time evolution (in 30 s steps) of the maximum correlation time delay $\tau_{MC}(t)$ defined as the time shift corresponding to the maximum absolute value of the cross-correlation function. Positive and negative correlation maps are plotted separately in (d) and (e), where only positive or negative correlation values are shown. We define positive correlation time delay $\tau_{PC}(t)$ (red circles) and negative correlation time delay $\tau_{NC}(t)$ (blue squares) as the time shift corresponding to the maximum positive or maximum negative correlation. (Online version in colour.)

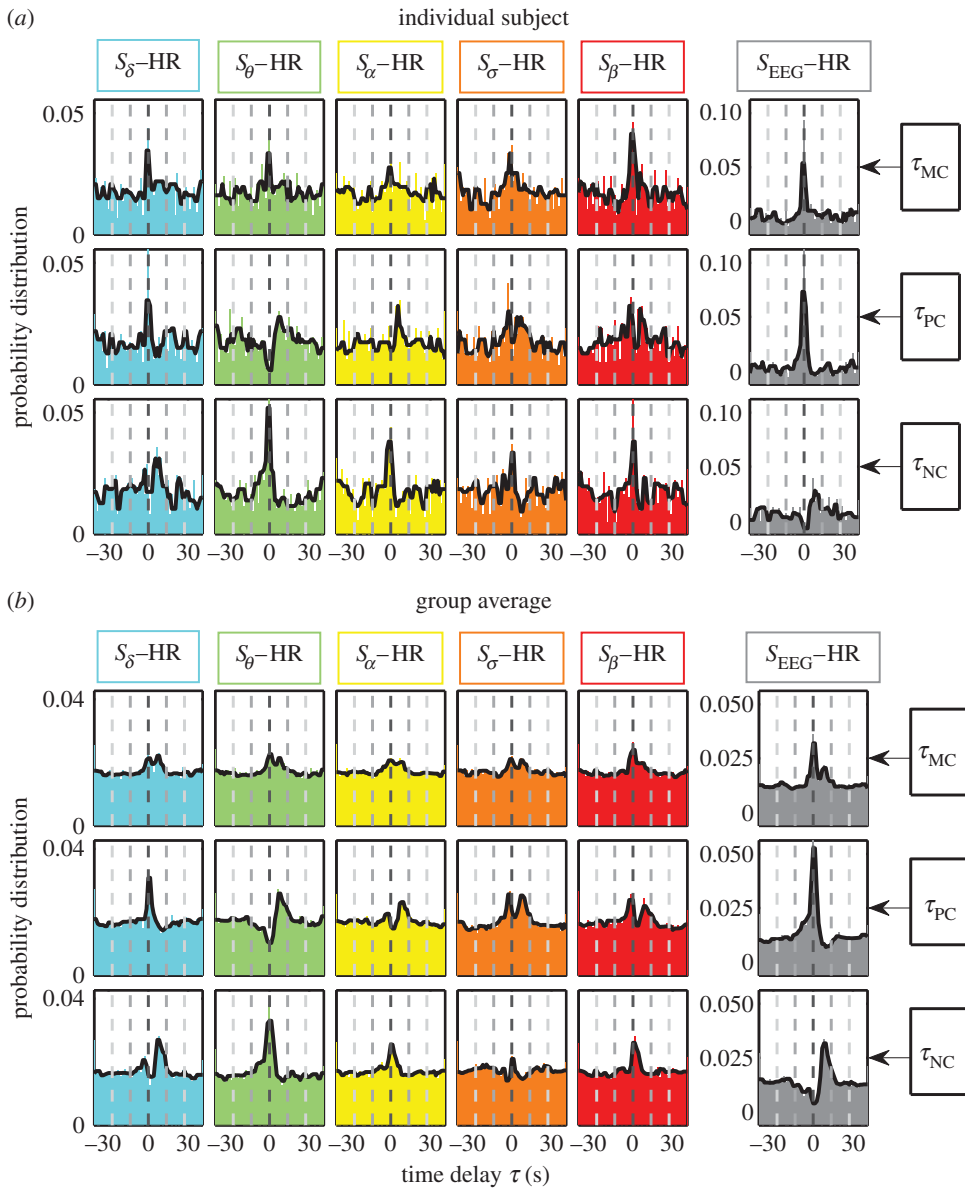


Figure 2. Probability distribution profiles for maximum, positive and negative correlation time delays τ_{MC} , τ_{PC} and τ_{NC} : (a) for an individual subject and (b) for the group average of 34 healthy subjects representing the entire night-time sleep period. Solid black line in each panel is a moving average of the probability distribution (smoothed profile with 3 s moving window). The bin size for the time delay τ is 1 s. Similarity between the individual subject profiles and the group average profiles for each pair of brain rhythm–heart interaction indicates a universal mechanism underlying time delays in brain–heart communication. (Online version in colour.)

To quantify the structure of DCL and to better understand the nature of interactions that generate the delay–correlation configuration at each time t , it is important to differentiate the two types of cross-correlation—positive versus negative. Thus, we construct the subset of DCL with only positive correlation, i.e. only ‘hills’ in the DCL, as shown in figure 1*d*, where red solid circles mark the positive correlation time delay, $\tau_{PC}(t) \equiv \tau(t)|_{\max C}$, corresponding to the time shift where maximum positive cross-correlation is observed at each time step t . Similarly, we also construct the negative DCL of blue ‘valleys’ as shown in figure 1*e*, where blue squares track the time

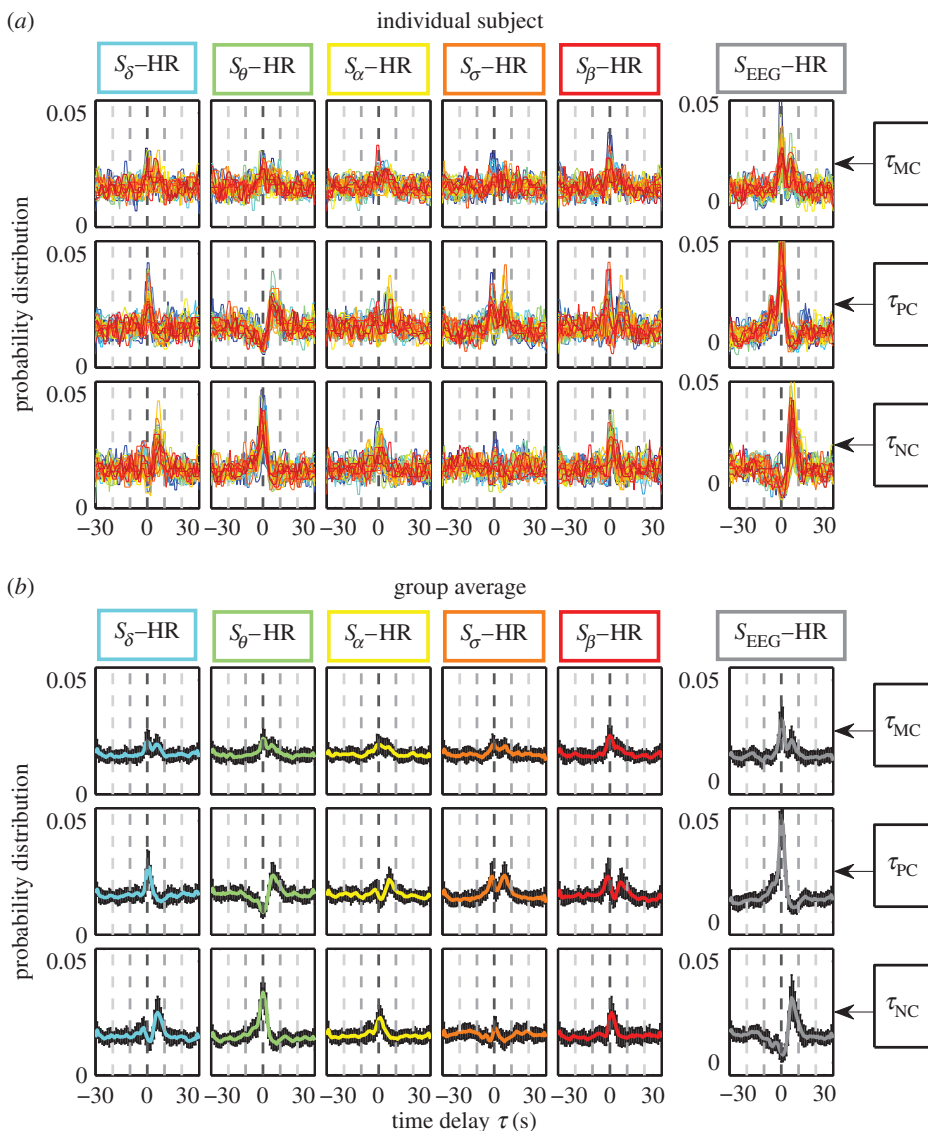


Figure 3. Statistical patterns of characteristic time delays underlying brain–heart communications. Probability distributions of the maximum correlation time delay τ_{MC} (first row), positive correlation time delay τ_{PC} (second row) and negative correlation time delay τ_{NC} (third row) are obtained from the generalized time-delay analysis (figure 1) for each pair of brain–heart interactions. (a) Individual distributions for all 34 subjects (plotted in different colours) and (b) the group average, where black error bars represent the standard deviation across subjects. Distributions are obtained for the entire night-time sleep period. Distribution profiles skewed to the right with peak at $\tau > 0$ indicate that activations in brain dynamics precede cardiac dynamics. Considering interactions between the relative spectral power of each brain rhythm and the HR, we find unique profiles for the probability distribution of the time delay τ , indicating a specific role of each brain rhythm in mediating brain–heart interactions. Note the different distribution profiles of τ_{MC} , τ_{PC} and τ_{NC} for the interaction between each brain rhythm and the heart, indicating that positive and negative cross-correlations are characterized by different time delays. Interactions between the total EEG power (all five brain rhythms) and the HR are characterized by a significant peak at $\tau_{PC} = 0$, indicating synchronized bursting activity in the brain–heart network where modulations in the same direction for the heart and the brain occur simultaneously. By contrast, total EEG power and HR interactions exhibit a sharp peak at $\tau_{NC} > 0$, indicating that modulations in the HR that are in opposite direction to changes in brain oscillation occur with a positive time delay. The double-peak distribution profile of τ_{MC} reflects a combination of the profiles for τ_{PC} and τ_{NC} . Remarkably, the ensemble of probability distribution profiles for all three types of time delays is consistently observed for all subjects with small standard deviation, indicating a universal mechanism underlying time delays in brain–heart communication. (Online version in colour.)

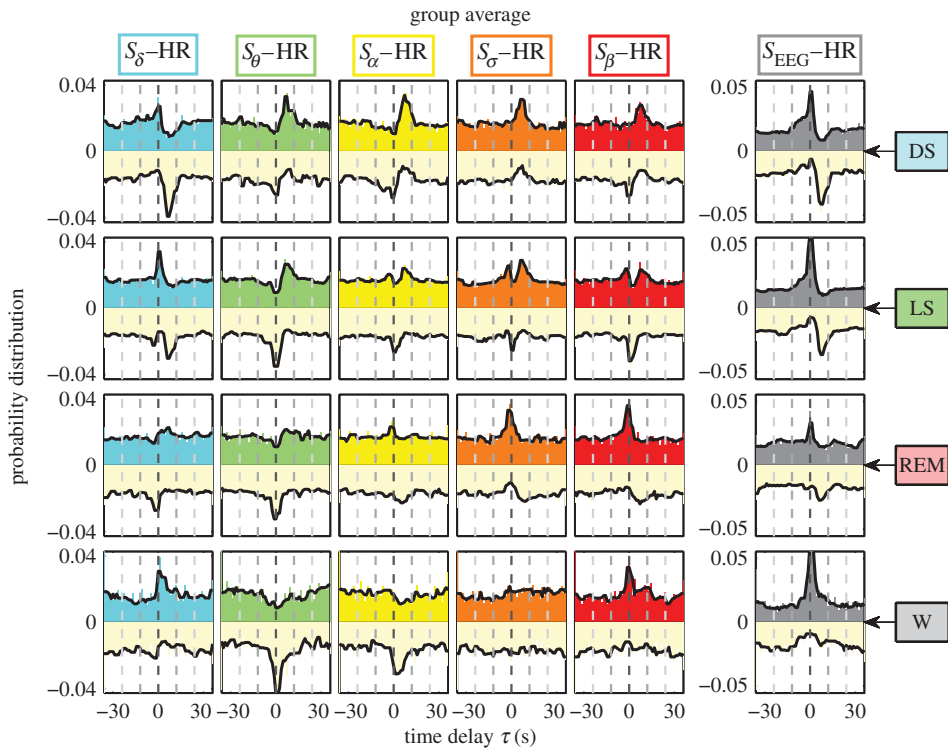


Figure 4. Change in brain–heart time-delay distribution profiles with transitions across physiologic states. Joint profiles of the probability distribution of τ_{PC} and τ_{NC} for each pair of brain–heart interactions during different physiologic states (sleep stages) obtained by pooling data from all subjects (see S2). Distributions for τ_{PC} are plotted in the upper half plane in each panel (different colours for different brain–heart interactions as in figure 3). Distributions for τ_{NC} are inverted and plotted in the lower half plane with the same light shade. Each sleep stage (horizontal row) is characterized by a specific set of profiles representing the time-delay characteristics for each brain–heart interaction. Considering each pair of brain rhythm and heart interaction (column), the joint distribution profile of τ_{PC} and τ_{NC} changes from one sleep stage to another, leading to a complex reorganization for the entire set of profiles across different physiologic states. This reorganization in the time-delay profiles across sleep stages is also observed for the total EEG spectral power (right column), indicating a pronounced change in the coupling between the overall brain activity and cardiac dynamics. Note that, for all pairs of brain–heart interactions during all sleep stages, there are no peaks with significant negative time delay, indicating that brain–heart communications are mainly mediated through directional interaction from the brain to the heart. Each sleep stage is characterized by a specific ensemble of joint time-delay distribution profiles indicating that these profiles are a robust signature of physiologic state. (Online version in colour.)

evolution of negative correlation time delay, $\tau_{NC}(t) \equiv \tau(t)|_{\min C}$, corresponding to the maximum negative cross-correlation at each time step t .

In our analyses of brain–heart interactions, we fix the second signal to be the instantaneous heart rate $y(t) \equiv \text{HR}(t)$, and we assign the first signal $x(t)$ as the relative spectral power of five physiologically relevant brain rhythms ($S_\delta(t)$, $S_\theta(t)$, $S_\alpha(t)$, $S_\sigma(t)$, $S_\beta(t)$) and the total spectral power $S_{\text{EEG}}(t)$. Under this definition, a positive time delay $\tau > 0$ always corresponds to a situation when the modulation in brain rhythms precedes corresponding changes in the cardiac signal, and vice versa for $\tau < 0$.

(c) Probability distributions of time delay

Our previous work has shown that TDS is a reliable measure of interaction and coupling between dynamical systems, and that it is sensitive to differentiate between physiological states and conditions even in cases when the amplitude of cross-correlation cannot provide a

statistically significant separation between real and surrogate data [36]. Thus, to probe brain–heart interactions, here we quantify the temporal dynamics and statistical properties of the time delay inherent to different pairs of brain rhythms and heart interactions by calculating the probability distribution $P(\tau)$ of three types of time delay, including maximum correlation time delay (τ_{MC}), positive correlation time delay (τ_{PC}) and negative correlation time delay (τ_{NC}). In other words, we are interested in the most probable time delay when significant cross-correlations are observed. The probability distribution is represented by a renormalized histogram of time delays and the summation of the histogram values over all bins (1 s bin) equals 1. As shown in figures 2 and 3, we obtain the probability distributions for all three types of time delay for a typical individual subject as well as for the entire group of subjects. Panels along the horizontal direction are colour-coded to represent interactions between different brain signals and the HR output, whereas different rows of panels correspond to different types of time delay.

For a given pair of brain–heart interaction, the probability distributions of τ_{PC} and τ_{NC} can be further combined into one histogram profile by plotting $P(\tau_{PC})$ in the upper half plane with corresponding colours as in figures 2 and 3, and inverting and plotting $P(\tau_{NC})$ in the lower half plane with the same light shade (figure 4). Combining histograms in this way enables us to better demonstrate the changes in the probability distribution profile of the time delay for a given pair of brain–heart interaction with transitions from one physiologic state (sleep stage) to another, as well as the corresponding hierarchical reorganization of the entire set of distribution profiles for all pairs of brain rhythms and heart interactions (shown in figure 4).

Peaks in the probability distribution profiles of time delay correspond to the characteristic time delays that underlie brain–heart communications, and the sign of these characteristic time delays is indicative of the directionality of brain–heart communication: $\tau > 0$ for directional interaction from the brain to the heart, whereas $\tau < 0$ indicates that cardiac dynamics precede modulations in brain activity.

3. Results and discussion

Integrated physiological systems, in general, are coupled by feedback and/or feed-forward loops with a broad range of time delays that underlie physiologic interactions. Combination of these feedback loops leads to different types of coordinated modulation in the output dynamics of physiological systems that can simultaneously coexist [25–27]. Characteristics of physiologic coupling and interaction, such as the range of time delays and different modes of coordination, are essential for the entire organism to optimize its function during different physiologic states and to generate proper response to external perturbation. Consequently, we focus on the characteristic time delays involved in different modes of brain–heart interaction.

We perform empirical analyses of EEG and HR data recorded in healthy subjects during nighttime sleep to probe the interaction between distinct brain rhythm and the heart, and how these interactions change with different sleep stages (well-defined physiologic states). As brain rhythm activation and cardiac dynamics continuously change even within the same physiologic state, we expect a high degree of complexity in the DCL representing brain–heart communications (§2). As shown in figure 1c, the DCL for the S_3 –HR interaction is characterized by pronounced heterogeneity where different types of cross-correlation (positive or negative correlation as represented by regions with different colours) form a complex mixture.

(a) Ensemble of characteristic time-delay profiles

To investigate whether there are characteristic time delays associated with brain–heart interactions, we construct the DCL (figure 1) for each pair of brain rhythm and HR signals. We obtain probability distributions for three distinct types of time delays:

- (i) Maximum correlation time delay (τ_{MC}) is the time shift which corresponds to the highest degree of cross-correlation defined as the maximum of $|C|$. If the fluctuations of τ_{MC}

remain small within the range of $\Delta\tau_{MC} = \pm 1$ s, the two signals are considered to exhibit TDS and the two physiological systems are linked during this time period [36,40,41].

- (ii) Positive correlation time delay (τ_{PC}) is the time shift for which two signals exhibit the maximum positive cross-correlation. Strong positive correlation C_{xy} is often associated with coordinated bursting activities in both signals, namely increase (or decrease) in signal x is accompanied by a corresponding increase (or decrease) in signal y .
- (iii) Negative correlation time delay (τ_{NC}) represents the time shift for which two signals exhibit the most negative cross-correlation. Thus, τ_{NC} characterizes the typical time delay when modulations in two signals occur in the opposite direction.

We find that, for each pair of brain–heart interaction, τ_{MC} , τ_{PC} and τ_{NC} are characterized by markedly different patterns in their probability distribution $P(\tau)$ (vertical columns in figures 2 and 3). For example, S_δ –HR interaction has a pronounced peak for $P(\tau_{PC})$ at $\tau_{PC} \approx 0$ s, while the peak for $P(\tau_{NC})$ is located at $\tau_{NC} \approx 6$ s, indicating that different modes of brain–heart coordination operate at markedly different time delays. For τ_{MC} , we consistently observe a double-peak pattern in its probability distribution for all pairs of brain rhythm and HR interactions, which reflects features of the distribution profiles for both τ_{PC} and τ_{NC} —this double-peak pattern is most pronounced for the S_{EEG} –HR interaction (figures 2 and 3).

Comparing pairs of interaction between the HR and different brain rhythms, we find that for each type of time delay (horizontal rows in figures 2 and 3) different pairs of brain–heart interactions exhibit distinct profiles of the probability distribution $P(\tau)$. For example, while $P(\tau_{PC})$ for the pair S_δ –HR has a dominant peak at $\tau_{PC} \approx 0$ s, the pair S_θ –HR is characterized by a dominant time delay of $\tau_{PC} \approx 6$ s, and S_σ –HR has characteristic time delays at both $\tau_{PC} \approx 0$ s and $\tau_{PC} \approx 6$ s. By contrast, comparing $P(\tau_{NC})$ for different pairs of brain rhythm–HR interaction, we observe a pronounced peak at $\tau_{NC} \approx 6$ s for S_δ –HR and peak at $\tau_{NC} \approx 0$ s for S_θ –HR; this is exactly opposite to the peak locations observed in $P(\tau_{PC})$ (figures 2 and 3). These distinct profiles indicate that each brain rhythm plays a specific role in mediating brain–heart interactions.

Remarkably, the entire ensemble of distribution profiles for all three types of time delays is robust, as it is consistently observed for all individual subjects (figure 3*a*) as well as for the group average behaviour (figure 3*b*). This consistency in time-delay distribution profiles is demonstrated by the small standard deviation across subjects (error bars around group average value, figure 3).

Our statistical analysis (electronic supplementary material, figure S5*a*) reveals that the most pronounced characteristic time delays underlying brain–heart communications are associated with the following pairwise interactions: (i) S_δ –HR, (ii) S_θ –HR and (iii) S_{EEG} –HR. These interactions exhibit statistically significant peaks in the profiles of $P(\tau_{PC})$ and $P(\tau_{NC})$, coupled with consistent time delays for τ_{PC} and τ_{NC} across subjects: (i) for S_δ –HR, $\tau_{PC} = 0$ s and $\tau_{NC} = 6$ s; (ii) for S_θ –HR, $\tau_{PC} = 6$ s and $\tau_{NC} = 0$ s; and (iii) for S_{EEG} –HR, $\tau_{PC} = 0$ s and $\tau_{NC} = 6$ s.

To further explore the interrelation between the characteristic time delays in the brain–heart communication and distinct physiologic functions, we calculate the probability distributions for τ_{PC} and τ_{NC} for different sleep stages, including deep sleep (DS), light sleep (LS), rapid eye movement sleep (REM) and wake/brief arousals (W).

We find that each sleep stage is characterized by a specific set of joint profiles of the probability distribution for τ_{PC} and τ_{NC} (horizontal rows in figure 4). Following each pair of brain–heart interaction (vertical columns in figure 4), we observe that the joint profile of τ_{PC} and τ_{NC} changes significantly from one sleep stage to another, reflecting changes in the neural regulation of cardiac dynamics. Moreover, we find that the joint τ_{PC} and τ_{NC} profile for each pair of brain–heart interaction follows a specific transition pattern across sleep stages (figure 4). Thus, with transition across physiological states there is a complex reorganization of the entire ensemble of time-delay distribution profiles of the different brain rhythm–HR interactions.

Intriguingly, our results for the total power S_{EEG} –HR interaction show that, with increase in sympathetic tone from DS to LS, REM and W, the peak in $P(\tau_{NC})$ at $\tau_{NC} = 6$ s completely vanishes (figure 4), corresponding to the loss of significant time delays for negative brain–heart cross-correlation (i.e. for modulations in the opposite directions between the EEG and

HR signals). Indeed, increased bursting activity in brain dynamics associated with dominant parasympathetic tone during DS and LS is associated with dipping in the HR, leading to a pronounced anti-correlation profile, which disappears under dominant sympathetic tone during wake. This pronounced $\tau_{\text{NC}} = 6 \text{ s}$ time delay is consistently observed for all subjects (electronic supplementary material, figure S5). While it may be associated with the baroreflex feedback loop, the underlying physiologic mechanism for this characteristic time delay remains to be explored. These observations identify characteristic time delays of brain–heart communications as a new hallmark of physiologic state and function.

Notably, we find that, for both τ_{PC} and τ_{NC} , there are no peaks at significant negative time delays as shown by the profiles in figure 4, indicating that brain–heart communications are mainly mediated through directional interaction from the brain to the cardiac system.

4. Conclusion

To understand the basic mechanisms of neuroautonomic control of the cardiac systems, we develop a generalized time-delay analysis framework and a novel DCL approach to investigate the role of distinct physiologically relevant brain rhythms in mediating brain–heart interactions. Compared with the traditional cross-correlation analysis with a fixed time delay or the original TDS approach, where the emergence of stable time delay marks the onset of dynamical coupling between two systems, the approach proposed here keeps track of both the time evolution and the delay dependence of the cross-correlation between two signals.

We find that brain–heart interactions exhibit characteristic time delays and that different modes of interaction (i.e. positive or negative cross-correlations) are characterized by different time delays. Our results demonstrate that the interactions between different brain rhythms and the HR are characterized by distinct distribution profiles for time delays, indicating that each brain rhythm has a specific role in mediating brain–heart communications. Furthermore, we find that the time-delay profile for each pair of brain rhythm and HR interaction follows a unique transition pattern from one sleep stage to another, leading to a complex reorganization of the entire ensemble of time-delay profiles.

As sleep-stage transitions are closely associated with changes in sympatho-vagal balance, the uncovered ensemble of time-delay profiles representing brain–heart interactions reveals previously unknown dynamical aspects of cardiac neural regulation that are a hallmark of physiologic state and function.

Remarkably, the uncovered time-delay distribution profiles for all pairs of brain rhythm and HR interactions are consistently observed in all healthy subjects, and exhibit a similar reorganization with transition across sleep stages in each subject. Thus, these new measures can potentially be used not only as robust markers of physiologic states and functions under healthy condition, but also as diagnostic and prognostic indicators of pathological perturbations.

The main purpose of this work is to present a first proof-of-concept demonstration of a DCL approach to identify and quantify the characteristic time delay underlying brain–heart interactions. Thus, in this study, we use data from the C3 EEG channel only, which is most commonly used in sleep research, and we use EEG_{C3}–HR interaction as an example to present our computational framework. Naturally, follow-up work will extend to other EEG leads to identify the different roles of brain location in mediating brain–heart interactions. These extended analyses may include not only instantaneous HR time series, as presented here, but also high- and low-frequency HR components as well as other static and dynamic local characteristics of the cardiac output. Further, modelling approaches based on surrogate time series with different autocorrelations and other dynamical characteristics as observed in the brain and heart output signals can help elucidate the origin and structure of the DCL representing brain–heart interactions during different sleep stages.

The proposed time-delay approach is general and can be applied to other types of dynamical systems with complex output signals where the existence and the nature of coupling and interactions are not known *a priori*. Moreover, the novel concept of delay-correlation landscape

encompasses all key elements of cross-correlation, and provides a comprehensive picture of the coupling strength, characteristic time delays and time evolution of correlation between dynamical systems. Thus, the approach presented here can serve as a general analytical tool to understand basic mechanisms underlying physiological interactions, which is essential for the development of the new field of ‘Network Physiology’.

Ethics. The research protocol was approved by the Institutional Review Boards of Boston University (Boston, MA, USA) and was conducted according to the principles expressed in the Declaration of Helsinki.

Data accessibility. The data we used in this work are pre-existing multi-channel physiologic recordings from EU SIESTA databases. The detailed protocol of the SIESTA database can be found in Klösch *et al.* [43]. All participants provided written informed consent.

Authors' contributions. A.L. and K.K.L.L. contributed equally to this paper. A.L. and K.K.L.L. designed the analysis algorithm. A.L., K.K.L.L., R.P.B. and P.Ch.I. analysed the data. K.K.L.L., R.P.B. and P.Ch.I. prepared the manuscript. P.Ch.I. initiated the investigation and supervised all aspects of the work. All authors discussed the results and commented on the manuscript.

Competing interests. The authors declare that they have no competing interests.

Funding. This research was supported by W. M. Keck Foundation, National Institutes of Health (NIH grant 1R01-HL098437), the Office of Naval Research (ONR grant 000141010078), the US–Israel Binational Science Foundation (BSF grant 2012219), EC-FP7 Marie Curie Fellowship (IIF 628159) (to R.P.B.), the National Natural Science Foundation of China (grant no. 61304145) (to A.L.) and the Research Fund for the Doctoral Program of Higher Education (grant no. 20130009120016) (to A.L.).

Acknowledgements. We acknowledge the generous support given by the above organizations.

References

1. Akselrod S, Gordon D, Ubel FA, Shannon DC, Berger AC, Cohen RJ. 1981 Power spectrum analysis of heart rate fluctuation: a quantitative probe of beat-to-beat cardiovascular control. *Science* **213**, 220–222. (doi:10.1126/science.6166045)
2. Somers VK, Dyken ME, Mark AL, Abboud FM. 1993 Sympathetic-nerve activity during sleep in normal subjects. *New Engl. J. Med.* **328**, 303–307. (doi:10.1056/NEJM199302043280502)
3. Otzenberger H, Gronfier C, Simon C, Charloux A, Ehrhart J, Piquard F, Brandenberger G. 1998 Dynamic heart rate variability: a tool for exploring sympathovagal balance continuously during sleep in men. *Am. J. Physiol.* **275**, H946–H950. See <http://ajpheart.physiology.org/content/275/3/H946>.
4. Malliani A, Pagani M, Lombardi F, Cerutti S. 1991 Cardiovascular neural regulation explored in the frequency domain. *Circulation* **84**, 482–492. (doi:10.1161/01.CIR.84.2.482)
5. Peng C-K, Havlin S, Stanley HE, Goldberger AL. 1995 Quantification of scaling exponents and crossover phenomena in nonstationary heartbeat time series. *Chaos* **5**, 82–87. (doi:10.1063/1.166141)
6. Ivanov PCh, Amaral LAN, Goldberger AL, Havlin S, Rosenblum MG, Struzik ZR, Stanley HE. 1999 Multifractality in human heartbeat dynamics. *Nature* **399**, 461–465. (doi:10.1038/20924)
7. Ivanov PCh, Amaral LAN, Goldberger AL, Havlin S, Rosenblum MG, Stanley HE, Struzik Z. 2001 From $1/f$ noise to multifractal cascades in heartbeat dynamics. *Chaos* **11**, 641–652. (doi:10.1063/1.1395631)
8. Bonnet M, Arand D. 1997 Heart rate variability: sleep stage, time of night, and arousal influences. *Electroencephalogr. Clin. Neurophysiol.* **102**, 390–396. (doi:10.1016/S0921-884X(96)96070-1)
9. Ivanov PCh, Bunde A, Amaral LAN, Havlin S, Fritsch-Yelle J, Baevsky RM, Stanley HE, Goldberger AL. 1999 Sleep–wake differences in scaling behavior of the human heartbeat: analysis of terrestrial and long-term space flight data. *Europhys. Lett.* **48**, 594–600. (doi:10.1209/epl/i1999-00525-0)
10. Ivanov PCh, Hu K, Hilton MF, Shea SA, Stanley HE. 2007 Endogenous circadian rhythm in human motor activity uncoupled from circadian influences on cardiac dynamics. *Proc. Natl Acad. Sci. USA* **104**, 20702–20707. (doi:10.1073/pnas.0709957104)
11. Bunde A, Havlin S, Kantelhardt JW, Penzel T, Peter J-H, Voigt K. 2000 Correlated and uncorrelated regions in heart-rate fluctuations during sleep. *Phys. Rev. Lett.* **85**, 3736–3739. (doi:10.1103/PhysRevLett.85.3736)

12. Kantelhardt JW, Ashkenazy Y, Ivanov PCh, Bunde A, Havlin S, Penzel T, Peter J-H, Stanley HE. 2002 Characterization of sleep stages by correlations in the magnitude and sign of heartbeat increments. *Phys. Rev. E* **65**, 051908. (doi:10.1103/PhysRevE.65.051908)
13. Dvir I, Adler Y, Freimark D, Lavie P. 2002 Evidence for fractal correlation properties in variations of peripheral arterial tone during REM sleep. *Am. J. Physiol. Heart Circ. Physiol.* **283**, H434–H439. (doi:10.1152/ajpheart.00336.2001)
14. Karasik R, Sapir N, Ashkenazy Y, Ivanov PCh, Dvir I, Lavie P, Havlin S. 2002 Correlation differences in heartbeat fluctuations during rest and exercise. *Phys. Rev. E* **66**, 062902. (doi:10.1103/PhysRevE.66.062902)
15. Echeverria JC, Aguilar SD, Ortiz MR, Alvarez-Ramirez J, González-Camarena R. 2006 Comparison of RR-interval scaling exponents derived from long and short segments at different wake periods. *Physiol. Meas.* **27**, N19–N25. (doi:10.1088/0967-3334/27/4/N01)
16. Corino VDA, Matteucci M, Cravello L, Ferrari E, Ferrari AA, Mainardi LT. 2006 Long-term heart rate variability as a predictor of patient age. *Comp. Methods Prog. Biomed.* **82**, 248–257. (doi:10.1016/j.cmpb.2006.04.005)
17. Schmitt DT, Stein PK, Ivanov PCh. 2009 Stratification pattern of static and scale-invariant dynamic measures of heartbeat fluctuations across sleep stages in young and elderly. *IEEE Trans. Biomed. Eng.* **56**, 1564–1573. (doi:10.1109/TBME.2009.2014819)
18. Ho KKL, Moody GB, Peng C-K, Mietus JE, Larson MG, Levy D, Goldberger AL. 1997 Predicting survival in heart failure cases and controls using fully automated methods for deriving nonlinear and conventional indices of heart rate dynamics. *Circulation* **96**, 842–848. (doi:10.1161/01.CIR.96.3.842)
19. Huikuri HV, Mäkikallio TH, Peng C-K, Goldberger AL, Hintze U, Moller M. 2000 Fractal correlation properties of R-R interval dynamics and mortality in patients with depressed left ventricular function after an acute myocardial infarction. *Circulation* **101**, 47–53. (doi:10.1161/01.CIR.101.1.47)
20. Moelgaard H, Soerensen KE, Bjerregaard P. 1991 Circadian variation and influence of risk factors on heart rate variability in healthy subjects. *Am. J. Cardiol.* **68**, 777–784. (doi:10.1016/0002-9149(91)90653-3)
21. Penzel T, Wessel N, Riedl M, Kantelhardt JW, Rostig S, Glos M, Suhrbier A, Malberg H, Fietze I. 2007 Cardiovascular and respiratory dynamics during normal and pathological sleep. *Chaos* **17**, 015116. (doi:10.1063/1.2711282)
22. Valenza G, Garcia RG, Citi L, Scilingo EP, Tomaz CA, Barbieri R. 2015 Nonlinear digital signal processing in mental health: characterization of major depression using instantaneous entropy measures of heartbeat dynamics. *Front. Physiol.* **6**, 74. (doi:10.3389/fphys.2015.00074)
23. Lombardi F, Sandrone G, Pernpruner S, Sala R, Garimoldi M, Cerutti S, Baselli G, Pagani M, Malliani A. 1987 Heart rate variability as an index of sympathovagal interaction after acute myocardial infarction. *Am. J. Cardiol.* **60**, 1239–1245. (doi:10.1016/0002-9149(87)90601-1)
24. Ivanov PCh, Amaral LAN, Goldberger AL, Stanley HE. 1998 Stochastic feedback and the regulation of biological rhythms. *Europhys. Lett.* **43**, 363–368. (doi:10.1209/epl/i1998-00366-3)
25. Bartsch RP, Schumann AY, Kantelhardt JW, Penzel T, Ivanov PCh. 2012 Phase transitions in physiologic coupling. *Proc. Natl Acad. Sci. USA* **109**, 10 181–10 186. (doi:10.1073/pnas.1204568109)
26. Bartsch RP, Ivanov PCh. 2014 Coexisting forms of coupling and phase-transitions in physiological networks. *Commun. Comput. Inf. Sci.* **438**, 270–287. (doi:10.1007/978-3-319-08672-9_33)
27. Bartsch RP, Liu KKL, Ma QDY, Ivanov PCh. 2014 Three independent forms of cardio-respiratory coupling: transitions across sleep stages. *Comput. Cardiol.* **41**, 781–784. See <http://www.cinc.org/archives/2014/pdf/0781.pdf>.
28. Stankovski T, Duggento A, McClintock PVE, Stefanovska A. 2012 Inference of time-evolving coupled dynamical systems in the presence of noise. *Phys. Rev. Lett.* **109**, 024101. (doi:10.1103/PhysRevLett.109.024101)
29. Stankovski T, Ticcinelli V, McClintock PVE, Stefanovska A. 2015 Coupling functions in networks of oscillators. *New J. Phys.* **17**, 035002. (doi:10.1088/1367-2630/17/3/035002)

30. Napadow V, Dhond R, Conti G, Makris N, Brown EN, Barbieri R. 2008 Brain correlates of autonomic modulation: combining heart rate variability with fMRI. *NeuroImage* **42**, 169–177. (doi:10.1016/j.neuroimage.2008.04.238)
31. Song LZ, Schwartz GE, Russek LG. 1998 Heart-focused attention and heart–brain synchronization: energetic and physiological mechanisms. *Altern. Ther. Health Med.* **4**(5), 44–52, 54–60, 62.
32. Dumont M, Jurysta F, Lanquart J-P, Migeotte P-F, van de Borne P, Linkowski P. 2004 Interdependency between heart rate variability and sleep EEG: linear/non-linear? *Clin. Neurophysiol.* **115**, 2031–2040. (doi:10.1016/j.clinph.2004.04.007)
33. Chen Z, Hu K, Stanley HE, Novak V, Ivanov PCh. 2006 Cross-correlation of instantaneous phase increments in pressure-flow fluctuations: applications to cerebral autoregulation. *Phys. Rev. E* **73**, 031915. (doi:10.1103/PhysRevE.73.031915)
34. McCraty R, Atkinson M, Tomasino D, Bradley RT. 2009 The coherent heart: heart–brain interactions, psychophysiological coherence, and the emergence of system-wide order. *Integral Rev.* **5**(2), 10–115. See http://integral-review.org/pdf-template-issue.php?pdfName=vol_5_no_2_mccraty_et_al_the_coherent_heart.pdf.
35. Long X, Arends JB, Aarts RM, Haakma R, Fonseca P, Rolink J. 2015 Time delay between cardiac and brain activity during sleep transitions. *Appl. Phys. Lett.* **106**, 143702. (doi:10.1063/1.4917221)
36. Bashan A, Bartsch RP, Kantelhardt JW, Havlin S, Ivanov PCh. 2012 Network physiology reveals relations between network topology and physiological function. *Nat. Commun.* **3**, 702. (doi:10.1038/ncomms1705)
37. Faes L, Nollo G, Jurysta F, Marinazzo D. 2014 Information dynamics of brain–heart physiological networks during sleep. *New J. Phys.* **16**, 105005. (doi:10.1088/1367-2630/16/10/105005)
38. Faes L, Marinazzo D, Jurysta F, Nollo G. 2015 Linear and non-linear brain–heart and brain–brain interactions during sleep. *Physiol. Meas.* **36**, 683–698. (doi:10.1088/0967-3334/36/4/683)
39. Ivanov PCh, Bartsch RP. 2014 Network physiology: mapping interactions between networks of physiologic networks. In *Networks of networks: the last frontier of complexity* (eds G D’Agostino, A Scala), ch. 10, pp. 203–222. Understanding Complex Systems series. Cham, Switzerland: Springer International. (doi:10.1007/978-3-319-03518-5_10).
40. Bartsch RP, Liu KKL, Bashan A, Ivanov PC. 2015 Network physiology: how organ systems dynamically interact. *PLoS ONE* **10**, e0142143. (doi:10.1371/journal.pone.0142143)
41. Liu KKL, Bartsch RP, Lin A, Mantegna RN, Ivanov PC. 2015 Plasticity of brain wave network interactions and evolution across physiologic states. *Front. Neural Circuits* **9**, 62. (doi:10.3389/fncir.2015.00062)
42. Liu KKL, Bartsch RP, Ma QDY, Ivanov PCh. 2015 Major component analysis of dynamic networks of physiologic organ interactions. *J. Phys. Conf. Ser.* **640**, 012013. (doi:10.1088/1742-6596/640/1/012013)
43. Klösch G *et al.* 2001 The SIESTA project polygraphic and clinical database. *IEEE Eng. Med. Biol. Mag.* **20**, 51–57. (doi:10.1109/51.932725)
44. Rechtschaffen A, Kales A 1968 *A manual of standardized terminology, techniques and scoring system for sleep stages of human subjects*. Bethesda, MD: U.S. Department of Health, Education, and Welfare.
45. Press WH, Teukolsky SA, Vetterling WT, Flannery BP 2007 *Numerical recipes: the art of scientific computing*, 3rd edn. Cambridge, UK: Cambridge University Press.
46. Campbell IG. 2009 Unit 10.2: EEG recording and analysis for sleep research. In *Current protocols in neuroscience*, Suppl. 49, pp. 10.2.1–10.2.19. Hoboken, NJ: John Wiley & Sons. (doi:10.1002/0471142301.ns1002s49)

Web of Science InCites Journal Citation Reports Essential Science Indicators EndNote Publons Sign In Help English

Web of Science

Clarivate Analytics

Search Search Results My Tools Searches and alerts Search History Marked List

FIND@BU Free Published Article From Repository Save to EndNote online Add to Marked List

121 of 127

Delay-correlation landscape reveals characteristic time delays of brain rhythms and heart interactions

By: Lin, AJ (Lin, Aijing)^[1,2]; Liu, KKL (Liu, Kang K. L.)^[2,3]; Bartsch, RP (Bartsch, Ronny P.)^[4]; Ivanov, PC (Ivanov, Plamen Ch.)^[2,5,6]

[View ResearcherID and ORCID](#)

PHILOSOPHICAL TRANSACTIONS OF THE ROYAL SOCIETY A-MATHEMATICAL PHYSICAL AND ENGINEERING SCIENCES

Volume: 374 Issue: 2067

Article Number: 20150182

DOI: 10.1098/rsta.2015.0182

Published: MAY 13 2016

Document Type: Article

[View Journal Impact](#)

Abstract

Within the framework of 'Network Physiology', we ask a fundamental question of how modulations in cardiac dynamics emerge from networked brain-heart interactions. We propose a generalized time-delay approach to identify and quantify dynamical interactions between physiologically relevant brain rhythms and the heart rate. We perform empirical analysis of synchronized continuous EEG and ECG recordings from 34 healthy subjects during night-time sleep. For each pair of brain rhythm and heart interaction, we construct a delay-correlation landscape (DCL) that characterizes how individual brain rhythms are coupled to the heart rate, and how modulations in brain and cardiac dynamics are coordinated in time. We uncover characteristic time delays and an ensemble of specific profiles for the probability distribution of time delays that underly brain-heart interactions. These profiles are consistently observed in all subjects, indicating a universal pattern. Tracking the evolution of DCL across different sleep stages, we find that the ensemble of time-delay profiles changes from one physiologic state to another, indicating a strong association with physiologic state and function. The reported observations provide new insights on neurophysiological regulation of cardiac dynamics, with potential for broad clinical applications. The presented approach allows one to simultaneously capture key elements of dynamic interactions, including characteristic time delays and their time evolution, and can be applied to a range of coupled dynamical systems.

Keywords

Author Keywords: brain-heart interactions; time-delay analysis; delay-correlation landscape; Network Physiology

KeyWords Plus: FRACTAL CORRELATION-PROPERTIES; ACUTE MYOCARDIAL-INFARCTION; RATE-VARIABILITY; SCALING EXPONENTS; SLEEP; DYNAMICS; LONG

Author Information

Reprint Address: Ivanov, PC (reprint author)

+ Boston Univ, Dept Phys, Keck Lab Network Physiol, Boston, MA 02215 USA.

Reprint Address: Ivanov, PC (reprint author)

+ Harvard Univ, Sch Med, Brigham & Womens Hosp, Div Sleep Med, Boston, MA 02115 USA.

Reprint Address: Ivanov, PC (reprint author)

+ Bulgarian Acad Sci, Inst Solid State Phys, Blvd Lenin 72, BU-1784 Sofia, Bulgaria.

Citation Network

In Web of Science Core Collection

9

Times Cited

[Create Citation Alert](#)

All Times Cited Counts

9 in All Databases

[See more counts](#)

48

Cited References

[View Related Records](#)

Most recently cited by:

Ma, Xiaofei; Huang, Xiaolin; Du, Sidan; et al.
[Symbolic joint entropy reveals the coupling of various brain regions.](#)
PHYSICA A-STATISTICAL MECHANICS AND ITS APPLICATIONS (2018)

Shashikumar, Supreeth P.; Li, Qiao; Clifford, Gari D.; et al.
[Multiscale network representation of physiological time series for early prediction of sepsis.](#)
PHYSIOLOGICAL MEASUREMENT (2017)

[View All](#)

Use in Web of Science

Web of Science Usage Count

3

Last 180 Days

17

Since 2013

[Learn more](#)

This record is from:
Web of Science Core Collection

Addresses:

- + [1] Beijing Jiaotong Univ, Sch Sci, Dept Math, Beijing 100044, Peoples R China
- + [2] Boston Univ, Dept Phys, Keck Lab Network Physiol, Boston, MA 02215 USA
- + [3] Harvard Univ, Sch Med, Beth Israel Deaconess Med Ctr, Dept Neurol, Boston, MA 02215 USA
- + [4] Bar Ilan Univ, Dept Phys, IL-5290002 Ramat Gan, Israel
- + [5] Harvard Univ, Sch Med, Brigham & Womens Hosp, Div Sleep Med, Boston, MA 02115 USA
- + [6] Bulgarian Acad Sci, Inst Solid State Phys, Blvd Lenin 72, BU-1784 Sofia, Bulgaria

E-mail Addresses: plamen@buphy.bu.edu

Suggest a correction

If you would like to improve the quality of the data in this record, please [suggest a correction](#).

Funding

Funding Agency	Grant Number
W. M. Keck Foundation	
National Institutes of Health (NIH)	1R01- HL098437
Office of Naval Research (ONR grant)	000141010078
US-Israel Binational Science Foundation (BSF grant)	2012219
EC-FP7 Marie Curie Fellowship	IIF 628159
National Natural Science Foundation of China	61304145
Research Fund for the Doctoral Program of Higher Education	20130009120016

[View funding text](#)

Publisher

ROYAL SOC, 6-9 CARLTON HOUSE TERRACE, LONDON SW1Y 5AG, ENGLAND

Journal Information

Impact Factor: [Journal Citation Reports](#)

Categories / Classification

Research Areas: Science & Technology - Other Topics

Web of Science Categories: Multidisciplinary Sciences

[See more data fields](#)

◀ 121 of 127 ▶

Cited References: 48

Showing 30 of 48 [View All in Cited References page](#)

(from Web of Science Core Collection)

1. **POWER SPECTRUM ANALYSIS OF HEART-RATE FLUCTUATION - A QUANTITATIVE PROBE OF BEAT-TO-BEAT CARDIOVASCULAR CONTROL** **Times Cited: 3,445**
 By: AKSELROD, S; GORDON, D; UBEL, FA; et al.
 SCIENCE Volume: 213 Issue: 4504 Pages: 220-222 Published: 1981
2. **Three Independent Forms of Cardio-Respiratory Coupling: Transitions across Sleep Stages** **Times Cited: 11**
 By: Bartsch, Ronny P.; Liu, Kang K. L.; Ma, Qianli D. Y.; et al.
 2014 COMPUTING IN CARDIOLOGY CONFERENCE (CINC), VOL 41 Book Series: Computing in Cardiology Series Volume: 41
 Pages: 781-784 Published: 2014

Magnitude and sign of long-range correlated time series: Decomposition and surrogate signal generation

Manuel Gómez-Extremera,¹ Pedro Carpena,¹ Plamen Ch. Ivanov,^{2,3,4} and Pedro A. Bernaola-Galván¹

¹*Dpto. de Física Aplicada II, ETSI de Telecomunicación, University of Málaga, 29071 Málaga, Spain*

²*Keck Laboratory for Network Physiology, Department of Physics, Boston University, Boston, Massachusetts 02215, USA*

³*Harvard Medical School and Division of Sleep Medicine, Brigham and Women's Hospital, Boston, Massachusetts 02115, USA*

⁴*Institute of Solid State Physics, Bulgarian Academy of Sciences, 1784 Sofia, Bulgaria*

(Received 23 December 2015; published 4 April 2016)

We systematically study the scaling properties of the magnitude and sign of the fluctuations in correlated time series, which is a simple and useful approach to distinguish between systems with different dynamical properties but the same linear correlations. First, we decompose artificial long-range power-law linearly correlated time series into magnitude and sign series derived from the consecutive increments in the original series, and we study their correlation properties. We find analytical expressions for the correlation exponent of the sign series as a function of the exponent of the original series. Such expressions are necessary for modeling surrogate time series with desired scaling properties. Next, we study linear and nonlinear correlation properties of series composed as products of independent magnitude and sign series. These surrogate series can be considered as a zero-order approximation to the analysis of the coupling of magnitude and sign in real data, a problem still open in many fields. We find analytical results for the scaling behavior of the composed series as a function of the correlation exponents of the magnitude and sign series used in the composition, and we determine the ranges of magnitude and sign correlation exponents leading to either single scaling or to crossover behaviors. Finally, we obtain how the linear and nonlinear properties of the composed series depend on the correlation exponents of their magnitude and sign series. Based on this information we propose a method to generate surrogate series with controlled correlation exponent and multifractal spectrum.

DOI: [10.1103/PhysRevE.93.042201](https://doi.org/10.1103/PhysRevE.93.042201)

I. INTRODUCTION

A wide variety of phenomena in different fields ranging from physiology to economy show complex dynamics generating output signals that appear to be erratic and noisy but that, in fact, possess long-range correlations with scale-invariant structure. In addition, it has been observed that the presence of such correlations is linked to relevant properties of the system under study; for example, the correlations in the series of heartbeats change from healthy to pathological conditions [1] or under different physiological states [2].

In many cases, given a time series $x_i, i = 1, 2, \dots, N$, its increments $\Delta x_i = x_{i+1} - x_i$ are more relevant than the series itself because the dynamical properties of the increments provide with interesting clues about the underlying dynamics of the system and could help to develop useful models.

For nonlinear systems it is important to go beyond the study of linear correlations because they do not account for all dynamical properties of such systems; e.g., increment time series with the same linear correlations could correspond to systems with completely different nonlinear and multifractal behaviors [3]. A simple approach to break this degeneration consists in studying separately the correlations of magnitude and sign of the increment time series. The correlations in the series of magnitudes (also known as volatility series) have been related to the presence of nonlinear correlations and multifractal structure [3–5], whereas the properties of the sign series are solely determined by the linear correlations [3,4] and have been studied in the context of first-passage time in scale-invariant correlated processes [6].

In addition, from the intuitive point of view, magnitude and sign time series contain different and complementary

information about the original signal: the magnitude measures how big the changes are and the sign indicates their direction. An example of this is the dynamics of the heart [3], which is thought to be the result of two competing forces, the sympathetic and parasympathetic branches of the autonomous nervous system, that leads to complex variability with scale-invariant characteristics. Roughly speaking, the first one is responsible for slow (small in magnitude) increases (positive in sign) of the heart rate, while the second is usually associated with fast (large in magnitude) decreases (negative in sign). Other examples of the usefulness of the magnitude and sign analysis are also found in fluid dynamics [7], geological [8,9], geophysical [10,11], and economical time series [12].

Despite the importance of the magnitude and sign time series we have just mentioned, there are still open questions: for example, given a time series with known long-range correlations, a key question is whether there are correlations present also in the magnitude and sign time series? The approach to address this question is what we call here the *decomposition* problem. In principle, the systematic study of this problem is a complicated task, since the original time series can have very different nature, as mentioned above. Instead, we study the decomposition problem in artificial time series, which are commonly used to model the behavior of long-range correlated time series. In particular, we consider fractional Gaussian noises (fGns) and fractional Brownian motions (fBms) to model respectively stationary and nonstationary long-range correlated time series.

Furthermore, a second important problem (still open in many cases) is how the magnitude and sign of the increments are coupled to form the whole signal: for example, in

the human heart, when analyzing the increments of the interbeat interval time series, it is not clear yet what the relationship is between the magnitude (how big the change in the cardiac rhythm is) and the sign (the direction of the change). Obviously, a systematic study of the coupling between magnitude and sign series would be of great interest to improve the understanding of the relation between them and the behavior of the underlying mechanisms of control. Specifically, we investigate how the correlations of the whole signal are controlled by the correlations in the magnitude and sign time series, as well as by the coupling between them. However, the coupling mechanism of magnitude and sign will be different in time series of different nature, since the underlying dynamics will be different as well, and this variety of potential coupling mechanisms makes a systematic analysis difficult. Nevertheless, we can approach this problem from a different point of view: we can study systematically the correlation properties of time series with *uncoupled* magnitude and sign. Such time series can be artificially generated by multiplying magnitude and sign time series (each one with known correlations) obtained from different fGns or fBms. In this way, we guarantee that both magnitude and sign series are independent and thus uncoupled. Such analysis is what we call here the *composition problem*. The composition problem can be useful to understand the behavior of complex systems characterized by the coupling of two different mechanisms, each controlling the dynamics of magnitude and sign respectively. In addition, the results of the composition problem are a reference of uncoupling and then can be used to detect the existence of coupling mechanisms when analyzing real complex time series.

This article is organized as follows: In Sec. II we describe the methods and algorithms used in this article. Specifically, in Sec. II A we describe Detrended Fluctuation Analysis (DFA), the method used here to quantify the linear correlations, in Sec. II B we explain Multifractal Detrended Fluctuation Analysis (MFDFA), the algorithm we use to obtain multifractal spectra of time series, and Sec. II C introduces the Fourier Filtering Method, which allows us to generate signals with given correlation exponent.

In Sec. III we systematically study the decomposition problem, i.e., the correlation properties of the magnitude and sign time series obtained from long-range power-law linearly correlated time series. In Sec. IV we investigate the composition problem; i.e., we systematically study the correlations properties of composed time series with uncoupled magnitude and sign series. The multifractal properties of such composed series are analyzed in Sec. V, and, finally, Sec. VI presents the conclusions of this work.

II. METHODS

A. Detrended Fluctuation Analysis (DFA)

Here we quantify the linear correlations of time series by using Detrended Fluctuation Analysis (DFA) [13], a modified version of Fluctuation Analysis (FA), which is able to eliminate the effects of the nonstationarity. This method provides a single quantitative parameter, the scaling exponent α , to represent the correlation properties of a long-range correlated series.

DFA consists of the following steps [13]:

(i) Starting with a correlated series $\{x_i\}$ of size N we first integrate the series and obtain

$$y(j) \equiv \sum_{i=1}^j [x_i - \mu], \quad (1)$$

where μ is the mean value of the entire series.

(ii) The integrated series $y(j)$ is divided into boxes of equal length ℓ .

(iii) In each box of length ℓ , we calculate a linear fit of $y(j)$ which represents the *linear trend* in that box. The y coordinate of the fit line in each box is denoted by $y_\ell(j)$.

(iv) The integrated series $y(j)$ is detrended by subtracting the local trend $y_\ell(j)$ in each box of length ℓ .

(v) For a given box size ℓ , the root mean square (r.m.s.) fluctuation for this integrated and detrended series is calculated:

$$F(\ell) = \sqrt{\frac{1}{N} \sum_{j=1}^N [y(j) - y_\ell(j)]^2}. \quad (2)$$

(vi) The above computation is repeated for a broad range of scales (box sizes ℓ) to provide a relationship between $F(\ell)$ and the box size ℓ .

For a power-law correlated time series, there exists a power-law relation between the average root-mean-square fluctuation function $F(\ell)$ and the box size ℓ : $F(\ell) \sim \ell^\alpha$. Thus, the fluctuations can be characterized by a scaling exponent α , a self-similarity parameter which quantifies the long-range power-law correlation properties of the signal.

If the power-law correlated time series is stationary ($\alpha < 1$), the autocorrelation function decays as a power law, $C(\ell) \sim \text{sgn}(1 - \gamma)/\ell^\gamma$, and the exponent α is related to the exponent γ by [14–16]

$$\alpha = \frac{2 - \gamma}{2}. \quad (3)$$

Note that for the special case $\gamma = 1$ ($\alpha = 0.5$) the autocorrelation function vanishes.

In addition, it can be shown, via the Wiener-Khinchin theorem, that the power spectrum of the series is also a power law, whose exponent β is indeed related to α [16]:

$$\alpha = \frac{\beta + 1}{2}. \quad (4)$$

Here it is worth mentioning that, although Wiener-Khinchin theorem is only for $\alpha < 1$, this relationship between α and β is also valid for $\alpha > 1$.

Values of $\alpha < 0.5$ indicate the presence of anticorrelations in the time series, $\alpha = 0.5$ absence of correlations (white noise) and $\alpha > 0.5$ indicates the presence of positive correlations in the time series. In particular, for $\alpha = 1.5$ the series correspond to the well-known Brownian motion.

The performance of DFA has been systematically studied for time series with different trends [17,18], missing data [19], different artifacts [20], linear and nonlinear preprocessing filters [21], and coarse graining of the time series values [22].

B. Multifractal Detrended Fluctuation Analysis (MFDFA)

DFA studies the scaling of the second-order moment as a function of the window size ℓ , and thus, it takes into account only the linear correlations present in the series. MFDFA can be understood as a generalization of DFA in the sense that it analyzes the scaling of all possible moments of order q (including negative ones) [23]. To do so, Eq. (2) is generalized as follows:

$$F_q(\ell) = \left[\frac{1}{N} \sum_{j=1}^N |y(j) - y_\ell(j)|^q \right]^{\frac{1}{q}}. \quad (5)$$

For long-range power-law correlated time series, the fluctuations $F_q(\ell)$ scale as a power law of the form

$$F_q(\ell) \sim \ell^{h(q)}, \quad (6)$$

where $h(q)$ is the scaling exponent of the fluctuations of order q as a function of the window size ℓ . Obviously, the DFA exponent α is a particular case for $q = 2$, i.e., $\alpha = h(2)$. For series with only linear correlations $h(q) = \alpha \forall q$, i.e., there is a single scaling exponent and the series is *monofractal*. On the other hand, when nonlinear correlations are present in the series, each moment scales with a different exponent $h(q)$ and the series will be *multifractal*.

The scaling exponents $h(q)$ can be related to the classical multifractal box-counting scaling exponents $\tau(q)$ by means of the expression

$$\tau(q) = qh(q) - 1. \quad (7)$$

Finally, calculating the Legendre transform we can obtain the multifractal spectrum (see Ref. [23]):

$$\zeta = \tau'(q), \quad (8)$$

$$f(\zeta) = q\zeta - \tau(q), \quad (9)$$

where $f(\zeta)$ denotes the fractal dimension of the subset of the series characterized by ζ . For the particular case of monofractal time series, as all the moments scale with the same exponent, $h(q) = \alpha, h'(q) = 0$, and the multifractal spectrum will be a delta function:

$$f(\zeta) = \delta(\zeta - \alpha). \quad (10)$$

In contrast, for a multifractal series, $f(\zeta)$ will have a nonzero width, $\Delta\zeta$, which can be used as a measure of the strength of the nonlinearities present in the series.

C. Fourier Filtering Method

To generate artificial series with long-range power-law correlations we use the Fourier Filtering Method (FFM) [24,25]. This method makes use of Eq. (4) to obtain a series with DFA exponent α .

It works as follows:

(i) Generate a white noise $\eta(i)$, i.e., a series of uncorrelated Gaussian-distributed numbers all with the same mean and variance, and compute its Fourier transform, $\hat{\eta}(f)$.

(ii) The series with the desired correlation exponent α is obtained as

$$x(i; \alpha) \equiv \mathcal{F}^{-1} \left[\frac{\hat{\eta}(f)}{f^{\alpha-1/2}} \right], \quad (11)$$

where $\mathcal{F}^{-1}[\cdot]$ denotes the inverse Fourier transform. To check this, simply take into account that the Fourier transform of $x(i; \alpha)$ is a power law of exponent $\alpha - 1/2$ and thus its power spectrum follows a power law with exponent $2\alpha - 1$, which, according to Eq. (4), gives a DFA exponent α . Time series generated by FFM are normalized to zero mean and unit variance.

III. DECOMPOSITION OF A TIME SERIES: CORRELATIONS IN THE MAGNITUDE AND SIGN

Our aim is to quantify the correlations in the magnitude and sign time series obtained from the decomposition of a long-range correlated time series with a given input correlations. To systematically analyze the correlation properties of the magnitude and sign series, we generate artificial series of length $2^{20} \simeq 10^6$ using FFM with different input values of the correlation exponent (α_{in}) equally spaced in the (0,2) interval. Figure 1 shows an example of a correlated series obtained for $\alpha_{\text{in}} = 1$, as well as its magnitude and sign series.

For each individual series we obtain its corresponding magnitude and sign series, compute their correlation exponents (α_{mag} and α_{sign} respectively), and average them over an ensemble of 200 experiments for each input α_{in} value. We also compute the correlation exponent of the generated time series (α_{out}), which could be slightly different from α_{in} due to statistical fluctuations and finite size effects (Fig. 2).

In Fig. 3 we show the results. We observe three different regions:

(i) $\alpha_{\text{in}} \leq 0.5$. Despite the anticorrelations of the time series, both magnitude and sign are essentially uncorrelated. In all cases the magnitude series show a perfect fit to a power law with exponent $\alpha_{\text{mag}} = 0.5$ for all considered scales. These series are virtually indistinguishable from random i.i.d. series. But, on the other hand, the sign series (especially for $\alpha_{\text{in}} > 0.2$)

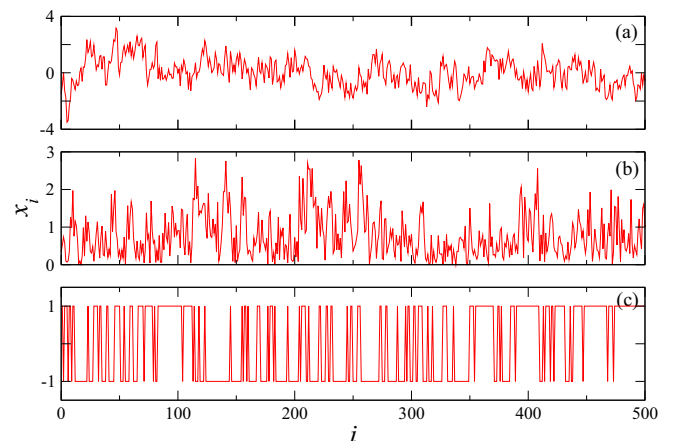


FIG. 1. (a) Example of correlated series obtained with the Fourier filtering method and $\alpha_{\text{in}} = 1$. (b) Series of its magnitudes and (c) series of its signs.

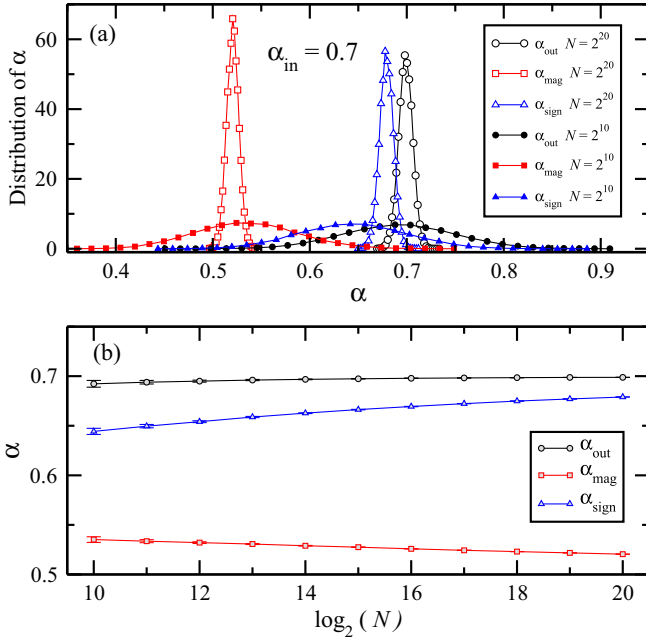


FIG. 2. Finite size effects. (a) Distributions of α_{out} , α_{mag} , and α_{sign} for two ensembles of 65 000 series generated by using the FFM with $\alpha_{\text{in}} = 0.7$. Open symbols: length of the series $N = 2^{20} \simeq 10^6$, full symbols: length of the series $N = 2^{10} \simeq 10^3$. Due to statistical fluctuations, the values of the correlation exponent α_{out} are not exactly equal to α_{in} ; instead they are normally distributed with a variance that decreases as N increases. A similar behavior is observed for α_{mag} and α_{sign} . (b) Mean values and standard deviations (error bars) of the distributions of α_{out} , α_{mag} , and α_{sign} for experiments similar to those in (a) for series size ranging from $N = 2^{10}$ to $N = 2^{20}$. In all three cases the mean values seem to approach an asymptotic value as N grows. In particular, both α_{out} and α_{sign} tend to the same value, α_{in} , the convergence being slower for α_{sign} . The fact that α_{out} and α_{sign} have the same asymptotic limit is observed only within the region $0.5 \leq \alpha_{\text{in}} < 1$, whereas in the region $\alpha_{\text{in}} > 1$, α_{mag} tends asymptotically to the same limit as α_{out} (see Sec. III).

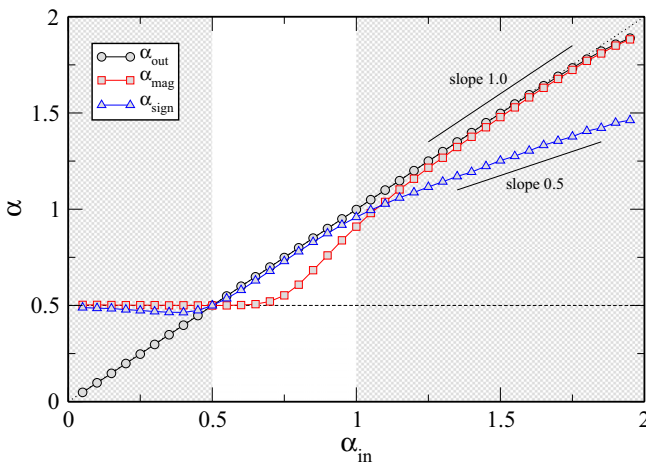


FIG. 3. Averaged correlation exponents for the composed signal (α_{out}), magnitude (α_{mag}), and sign (α_{sign}) as a function of α_{in} . For each value of α_{in} we generate 200 series of length $N = 2^{20}$ to obtain the averages.

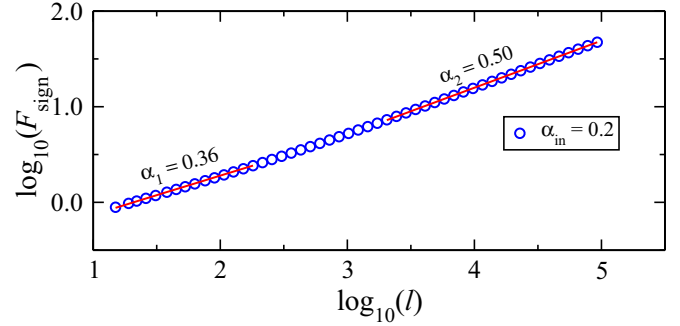


FIG. 4. $F_{\text{sign}}(\ell)$ vs ℓ for the sign series in the region $\alpha_{\text{in}} \leq 0.5$. We average $F_{\text{sign}}(\ell)$ over an ensemble of 200 sign series obtained from anticorrelated series of size $N = 2^{20}$ and $\alpha_{\text{in}} = 0.2$. The global scaling exponent, $\alpha_{\text{sign}} = 0.46$, indicates the presence of anticorrelations, but the direct inspection of $F_{\text{sign}}(\ell)$ reveals the existence of a crossover around $\ell_c = 190$. Below ℓ_c the sign series exhibits anticorrelations ($\alpha_1 = 0.36$), but such behavior disappears for $\ell > \ell_c$ ($\alpha_2 = 0.50$).

show values of $\alpha_{\text{sign}} \lesssim 0.5$ thus implying the presence of anticorrelations.

We find that only at short scales sign series show clear anticorrelated behavior, while at intermediate and large scales, the behavior is uncorrelated. This effect is shown in Fig. 4, where we plot the typical behavior of $F_{\text{sign}}(\ell)$ for the sign series in the region $\alpha_{\text{in}} \leq 0.5$. At small ℓ , $F_{\text{sign}}(\ell)$ scales with exponent $\alpha_1 = 0.36$ and, after a transition regime, the rest of the curve shows an scaling exponent $\alpha_2 = 0.50$ corresponding to uncorrelated behavior.

For this reason, the global exponent α_{sign} , obtained as a fit for the whole ℓ range (Fig. 3), is affected by these first values of the $F_{\text{sign}}(\ell)$ curve, thus leading to $\alpha_{\text{sign}} \lesssim 0.5$.

In summary, for large enough scales, both magnitude and sign series are uncorrelated. Having this in mind, the anticorrelations in the series (present at all scales) must be a result of the coupling between magnitude and sign because none of them are significantly anticorrelated themselves. To check this, we perform the following experiment: Generate a signal with $\alpha_{\text{in}} = 0.3$, decompose it into its magnitude and sign series, shuffle the sign (thus destroying all possible coupling between magnitude and sign), and finally multiply the randomized sign series by the original magnitude series to obtain a surrogate signal with uncoupled magnitude and sign. We also do the same experiment but randomizing the magnitude series. The results shown in Fig. 5 confirm our initial guess: the two surrogate series lose their anticorrelations since $F(\ell)$ scales as $\ell^{0.5}$. Note that in the second experiment, where we randomized the magnitude, the surrogate series still preserves certain anticorrelations at small scales coming from those present in the original sign series. Nevertheless, for ℓ large enough, the random behavior is recovered and the fluctuations scale with $\alpha = 0.5$.

An important conclusion drawn from here is the fact that it is not possible to obtain long-range anticorrelated binary sequences from the sign of an anticorrelated time series. This limitation has also been found in other methods described in the bibliography for the generation of long-range correlated binary sequences [26–28].

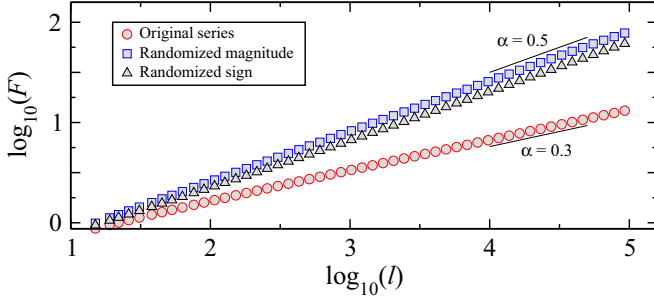


FIG. 5. $F(\ell)$ vs ℓ for anticorrelated series ($\alpha_{\text{in}} = 0.3$) and for surrogate series obtained by means of sign or magnitude randomization: Generate a sign with $\alpha_{\text{in}} = 0.3$, decompose it into its magnitude and sign series, randomize the sign or magnitude series, and obtain two surrogate series, one multiplying the randomized sign by the original magnitude (Δ) and the other multiplying the randomized magnitude by the original sign (\square). Both curves have been obtained for signals with $N = 2^{20}$ and averaging over 200 experiments.

(ii) $0.5 < \alpha_{\text{in}} < 1$. In this region sign series show correlations in the whole interval, while magnitude series are correlated only beyond $\alpha_{\text{in}} = 0.75$. Nevertheless, the correlations in the original signal are controlled by those in the sign no matter if the magnitude series are correlated or not. These results are in agreement with Ref. [29], where an analytical relation between $C(\ell)$ and $C_{\text{sign}}(\ell)$ was found:

$$C(\ell) = \sin \left[\frac{\pi}{2} C_{\text{sign}}(\ell) \right] \quad (12)$$

valid for $\gamma < 1$ and $C(\ell) > 0$, i.e., $0.5 < \alpha < 1$. Taking into account that the correlations will be much smaller than one for large enough ℓ , the sine in Eq. (12) can be approximated by its argument, and, assuming power-law dependence for the autocorrelation function, we get

$$\frac{1}{\ell^{\gamma_{\text{out}}}} \simeq \frac{\pi}{2} \frac{1}{\ell^{\gamma_{\text{sign}}}}, \quad (13)$$

and using (3) we obtain

$$\alpha_{\text{sign}} \simeq \alpha_{\text{out}} - \frac{\log(\pi/2)}{2 \log \ell}. \quad (14)$$

Note that, according to Eq. (14), in Fig. 3, α_{sign} is always slightly smaller than α_{out} . In fact, $\alpha_{\text{sign}} \rightarrow \alpha_{\text{out}}$ only asymptotically [see Fig. 2(b)]. This behavior has been already observed by Carretero-Campos *et al.* [6] studying the sign series in the context of the distribution of first-passage times in correlated time series.

Within this region, sign series provide an easy method to obtain correlated binary sequences with a correlation exponent α_{sign} , which is virtually the same as the exponent of the original series α_{in} . For example, this method is useful to study DNA sequences that have been frequently modeled as correlated binary sequences with correlation exponents $0.5 < \alpha < 1$ [30].

Here, contrary to what we observed in the previous region, the coupling between magnitude and sign does not seem to play a relevant role. Indeed, as we will show in Sec. IV, even under the assumption of independence between magnitude and

sign, the correlations of the signal are controlled by those in the sign, as long as $\alpha_{\text{mag}}, \alpha_{\text{sign}} \in (0.5, 1)$.

(iii) $1 < \alpha_{\text{in}} < 2$. Both α_{mag} and α_{sign} continue increasing with α_{in} . Now, α_{mag} is the one which tends asymptotically to α_{out} ; i.e., in this region correlations of the composed signal are controlled by the magnitude. On the other hand, α_{sign} grows as a function of α_{in} with slope $1/2$; thus, in this region:

$$\alpha_{\text{sign}} = \frac{1}{2}(1 + \alpha_{\text{in}}). \quad (15)$$

This behavior can be explained analytically by using the properties of the distribution of first-passage times for linearly correlated series found in Ref. [6]. It is also easy to show that α_{sign} cannot be larger than $3/2$ (see Appendix A for a proof of both properties).

In summary, we have for the correlation exponent α_{sign} as a function of α_{in} the next asymptotic behavior:

$$\alpha_{\text{sign}} = \begin{cases} \frac{1}{2} & \alpha_{\text{in}} < \frac{1}{2} \\ \alpha_{\text{in}} & \frac{1}{2} \leq \alpha_{\text{in}} < 1 \\ \frac{1}{2}(1 + \alpha_{\text{in}}) & 1 \leq \alpha_{\text{in}} < 2 \\ \frac{3}{2} & 2 \leq \alpha_{\text{in}} \end{cases} \quad (16)$$

For the correlation exponent α_{mag} the asymptotic behavior consists of an uncorrelated zone for $\alpha_{\text{in}} < \frac{3}{4}$, a transition for $\frac{3}{4} < \alpha_{\text{in}} < \frac{5}{4}$, and a region where $\alpha_{\text{mag}} \simeq \alpha_{\text{in}}$ for $\alpha_{\text{in}} > \frac{5}{4}$. The correlations observed for the series of magnitudes $|\Delta x_i|$ are in good agreement with those obtained for the series $(\Delta x_i)^2$ in Ref. [5].

IV. COMPOSITION OF MAGNITUDE AND SIGN SERIES

As we stated in the introduction, we are also interested in the properties of the composition of independent series of correlated signs and magnitudes. Our interest is double: On the one hand, we study the behavior of time series whose magnitude and sign are controlled by independent mechanisms. One of them controls the magnitudes of the increments while their signs are controlled by the other. This can be considered as the simplest approach to model real signals. On the other hand, by understanding the behavior of time series with independent magnitude and sign, we are able to identify when magnitude and sign are not independent, and consequently, we can establish a coupling detection method. Thus, by investigating the correlation properties of such composed time series, we can elucidate whether the magnitude and sign of a real time series are uncoupled or not.

The procedure to generate a composed time series with independent magnitude and sign works as follows. In order to obtain independent series of magnitude and sign, using FFM we generate two independent correlated series with input correlation exponents α_{in1} and α_{in2} , $x(i; \alpha_{\text{in1}})$ and $x(i; \alpha_{\text{in2}})$ respectively. Then the magnitude series is obtained as

$$x_{\text{mag}}(i) = |x(i; \alpha_{\text{in1}})|, \quad (17)$$

whose correlation exponent, α_{mag} depends on α_{in1} (Fig. 3). Correspondingly, we obtain the sign series as

$$x_{\text{sign}}(i) = \text{sgn}[x(i; \alpha_{\text{in2}})], \quad (18)$$

whose correlation exponent α_{sign} depends on $\alpha_{\text{in}2}$ (Fig. 3). Finally, the composed series is given by

$$x_{\text{comp}}(i) = x_{\text{mag}}(i) \cdot x_{\text{sign}}(i). \quad (19)$$

Here we systematically study the correlations of the composed series with $\alpha_{\text{in}1}, \alpha_{\text{in}2}$ in the range $[0.5, 2]$ leading to $\alpha_{\text{mag}} \in [0.5, 1.5]$ and $\alpha_{\text{sign}} \in [0.5, 2]$ (Fig. 3). Note that we do not explore the region $\alpha_{\text{in}1}, \alpha_{\text{in}2} < 0.5$ because, as we have shown above, for these values both magnitude and sign are essentially uncorrelated. Depending on α_{mag} and α_{sign} we have observed three different behaviors.

A. Case $\alpha_{\text{sign}} < 1$

Here, independently of the exponent α_{mag} , the correlations in the composed series are controlled by those in the sign. Given a time series obtained as the product of two independent magnitude and sign series we show in Appendix B that its autocorrelation function can be written as

$$C(\ell) = C_{\text{sign}}(\ell) \frac{(\pi - 2)C_{\text{mag}}(\ell) + 2}{\pi}, \quad (20)$$

where $C(\ell), C_{\text{mag}}(\ell)$, and $C_{\text{sign}}(\ell)$ are the autocorrelation functions of the composed signal at distance ℓ , its magnitude, and its sign, respectively.

Depending on α_{mag} we distinguish two regimes:

(i) $\alpha_{\text{mag}} < 1$. If the series are power-law correlated we have

$$C_{\text{mag}}(\ell) \sim \ell^{-\gamma_{\text{mag}}} \quad \text{and} \quad C_{\text{sign}}(\ell) \sim \ell^{-\gamma_{\text{sign}}}, \quad (21)$$

where $\gamma_{\text{mag}} = 2\alpha_{\text{mag}} - 2$ and $\gamma_{\text{sign}} = 2\alpha_{\text{sign}} - 2$ according to (3). Using Eq. (21) in Eq. (20) we have for the autocorrelation of the composed signal:

$$C(\ell) \sim \frac{\pi - 2}{\pi} \ell^{-(\gamma_{\text{mag}} + \gamma_{\text{sign}})} + \frac{2}{\pi} \ell^{-\gamma_{\text{sign}}}. \quad (22)$$

As we are considering $\alpha_{\text{mag}}, \alpha_{\text{sign}} \in [0.5, 1)$, it follows that $\gamma_{\text{sign}} < \gamma_{\text{mag}} + \gamma_{\text{sign}}$, and thus, the second term will be the leading one for large enough ℓ :

$$C(\ell) \sim C_{\text{sign}}(\ell). \quad (23)$$

(ii) $\alpha_{\text{mag}} \geq 1$. Now $C_{\text{mag}}(\ell) = \text{constant}$ and it follows straightforwardly from (20) that

$$C(\ell) \propto C_{\text{sign}}(\ell). \quad (24)$$

Here it is important to note that while (23) is an approximation valid only for large enough ℓ , (24) holds in the whole range.

In Fig. 6 we show an example of such situations. For a fixed value α_{mag} we obtain composed series with different values of α_{sign} , and, in all cases, the resulting correlation exponent is almost the same as α_{sign} in agreement with Eqs. (23) and (24). According to this, we are able to generate artificial signals with the desired correlation exponent (controlled by α_{sign}) independently of the correlations in the magnitude series. As the correlations in the magnitude are known to be related to the nonlinear properties of the signal [5] this implies that we can control the linear and nonlinear properties of the composed signal (see Sec. V).

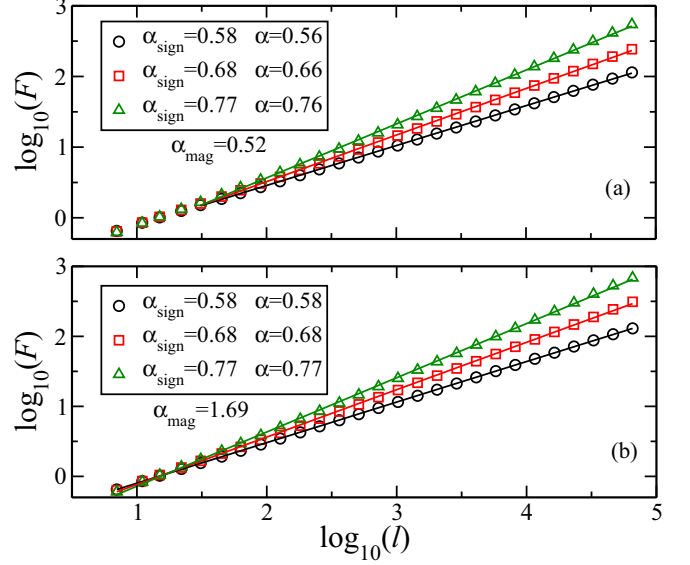


FIG. 6. Example of composed series generated by multiplying sign and magnitude from independent original series for $\alpha_{\text{sign}} < 1$. (a) $\alpha_{\text{mag}} < 1$. For ℓ large enough ($\ell > 30$) $F(\ell)$ scales with $\alpha \simeq \alpha_{\text{sign}}$ according to Eq. (23). (b) $\alpha_{\text{mag}} > 1$. $F(\ell)$ scales with $\alpha = \alpha_{\text{sign}}$ in the whole range. Note that, contrary to Eq. (23), Eq. (24) is not an approximation for large ℓ . The size of the time series is 2^{20} , and the results are averaged over 200 experiments.

B. Case $\alpha_{\text{mag}} < 1, \alpha_{\text{sign}} > 1$

Here we observe different behaviors at short and large scales (Fig. 7). While for small ℓ the correlation exponent $\alpha_1 \simeq \alpha_{\text{mag}}$, at large scales, the sign series takes over, and we get $\alpha_2 \simeq \alpha_{\text{sign}}$. The reason for this scaling crossover can be explained as follows: Taking into account that $\alpha_{\text{sign}} > 1$, a change of sign within a window of small size is unlikely to happen [6]; thus

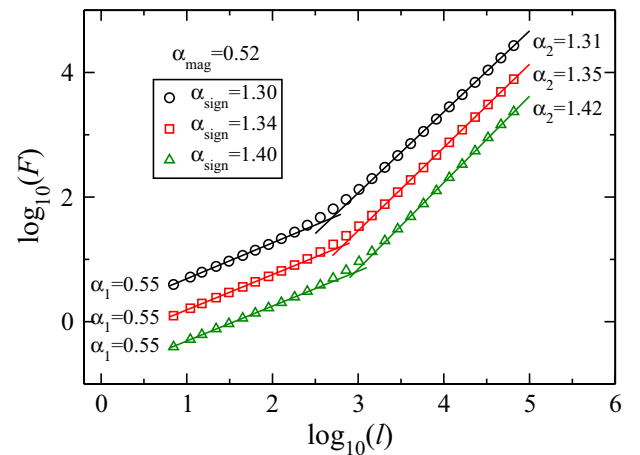


FIG. 7. Examples of composed series generated by multiplying sign and magnitude from independent original series for the case $\alpha_{\text{mag}} < 1$ and $\alpha_{\text{sign}} > 1$. We obtain a crossover ℓ dividing the range into two regions with different scaling: $\alpha_1 \simeq \alpha_{\text{mag}}$ for $\ell < \ell_c$ and $\alpha_2 \simeq \alpha_{\text{sign}}$ for $\ell > \ell_c$. The size of the time series is 2^{20} , and the results are averaged over 200 experiments. Different $F(\ell)$ have been shifted vertically for the sake of clarity.

the fluctuations at such scales depend only on the fluctuations of the magnitude. On the other hand, for large enough scales, the changes of the sign inside a single window will create fluctuations much higher than those of the magnitude, and thus, the correlation exponent will be close to α_{sign} .

The position of the crossover ℓ_c between both regimes depends on the size N of the series and can be determined analytically taking into account that the transition between these two regions should happen at a window size ℓ_c for which the fluctuations due to the oscillations of both sign and magnitude give the same contribution.

A long-range correlated series with $\alpha < 1$ is stationary, so we can write for the fluctuations in the magnitude at scale ℓ

$$F_{\text{mag}}(\ell) = A_{\text{mag}} \ell^{\alpha_{\text{mag}}}, \quad (25)$$

where A_{mag} is a constant. Nevertheless, for $\alpha \geq 1$ the series is nonstationary and the fluctuations at a given scale also depend on N . In Appendix A we show that the fluctuations in the sign series for $\alpha \geq 1$ can be written as

$$F_{\text{sign}}(\ell) = B_{\text{sign}} \frac{\ell^{\alpha_{\text{sign}}}}{N^{\alpha_{\text{sign}}-1}}, \quad (26)$$

where B_{sign} is a constant.

Clearly, the positive power of N ($\alpha_{\text{sign}} - 1 > 0$) dividing in Eq. (26) makes $F_{\text{sign}}(\ell) < F_{\text{mag}}(\ell)$ at small scales while $F_{\text{sign}}(\ell) > F_{\text{mag}}(\ell)$ for large ones. This behavior also justifies the fact, commented on above, that at short scales the series scales with $\alpha_1 \simeq \alpha_{\text{sign}}$ and $\alpha_2 \simeq \alpha_{\text{mag}}$ for the larger ones.

Thus, the crossover will be located at the point ℓ_c where the equality between (25) and (26) holds $F_{\text{mag}}(\ell_c) = F_{\text{sign}}(\ell_c)$ and then

$$\ell_c = \frac{A_{\text{mag}}}{B_{\text{sign}}} N^{\frac{\alpha_{\text{sign}}-1}{\alpha_{\text{sign}}-\alpha_{\text{mag}}}} \propto N^k, \quad (27)$$

where

$$k = \frac{\alpha_{\text{sign}} - 1}{\alpha_{\text{sign}} - \alpha_{\text{mag}}}. \quad (28)$$

The analytical results obtained in Eqs. (27) and (28) are in good agreement with the simulations shown in Fig. 8. It is worth mentioning that $k < 1$, provided that $\alpha_{\text{mag}} < 1$. This means that ℓ_c grows slower than the size of the system, and thus the crossover will always be observable for long enough series.

C. Case $\alpha_{\text{sign}} > 1, \alpha_{\text{mag}} > 1$

In this case $F(\ell)$ might also present a crossover, although it will be difficult to observe in practice. To better understand the behavior of $F(\ell)$ in this regime we follow a procedure similar to that described in the previous section. As well as in the previous section, $\alpha_{\text{sign}} > 1$, and we have for the fluctuations in the sign

$$F_{\text{sign}}(\ell) = B_{\text{sign}} \frac{\ell^{\alpha_{\text{sign}}}}{N^{\alpha_{\text{sign}}-1}}. \quad (29)$$

Now, in addition, the magnitude series is also nonstationary ($\alpha_{\text{mag}} > 1$), and, from the definition of fractional Brownian motion, the variance of the series grows as $N^{2(\alpha_{\text{mag}}-1)}$. This means that, in order to keep the series with unit standard deviation, the generation procedure (Sec. II C) carries out an

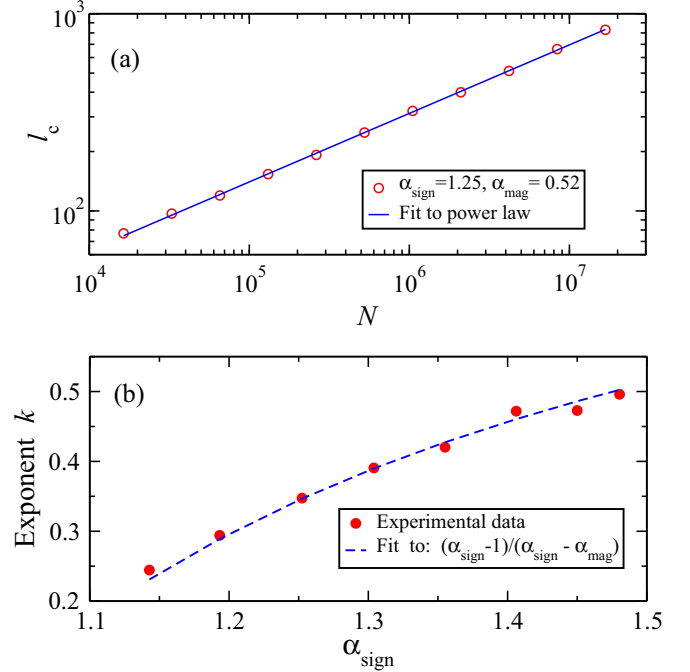


FIG. 8. Position of the crossover ℓ_c as a function of the size of the series N . (a) To check that ℓ grows as a power law of the system size N (27), we generate series with $\alpha_{\text{sign}} = 1.25$ and $\alpha_{\text{mag}} = 0.52$ and sizes in the range $[2^{13}, 2^{24}]$. For each size we obtain $F(\ell)$, average over 1000 series, and determine the position of the crossover ℓ_c by fitting $F(\ell)$ to the derivative of a sigmoid [31]. This procedure also gives α_1 and α_2 . The fit of the curve ℓ_c vs N (open red circles) to a power law (solid blue line) gives an exponent $k = 0.345$ close to the value 0.342 predicted by (28). (b) We repeat the experiment for different values of α_{sign} in the range $[1, 1.5]$ and obtain k for each one. Finally, we fit the curve of k vs α_{sign} (closed red circles) to (28) (dashed blue line). The value obtained for $\alpha_{\text{mag}} = 0.52$ coincides with the actual value used for the simulations.

implicit division of the series by the factor $N^{\alpha_{\text{mag}}-1}$ [32], and thus we will obtain for the fluctuations of the magnitude:

$$F_{\text{mag}}(\ell) = B_{\text{mag}} \frac{\ell^{\alpha_{\text{mag}}}}{N^{\alpha_{\text{mag}}-1}}. \quad (30)$$

Again, the position of the crossover will be given by the value ℓ_c for which the fluctuations in the magnitude and sign reach the same value:

$$B_{\text{mag}} \frac{\ell_c^{\alpha_{\text{mag}}}}{N^{\alpha_{\text{mag}}-1}} = B_{\text{sign}} \frac{\ell_c^{\alpha_{\text{sign}}}}{N^{\alpha_{\text{sign}}-1}}, \quad (31)$$

$$\ell_c = N \left(\frac{B_{\text{mag}}}{B_{\text{sign}}} \right)^{\frac{1}{\alpha_{\text{sign}}-\alpha_{\text{mag}}}} \propto N. \quad (32)$$

This means that the position of the crossover grows proportionally to the size of the series.

Here is important to point out that the normalization described above results in a reduction of the fluctuations at short scales [32]. This reduction becomes more evident as α increases, and thus, at short scales ($\ell \ll \ell_c$), the fluctuations are governed by the smallest exponent $\alpha_1 = \min\{\alpha_{\text{mag}}, \alpha_{\text{sign}}\}$, while at large scales ($\ell \gg \ell_c$) the correlation exponent will be given by $\alpha_2 = \max\{\alpha_{\text{mag}}, \alpha_{\text{sign}}\}$.

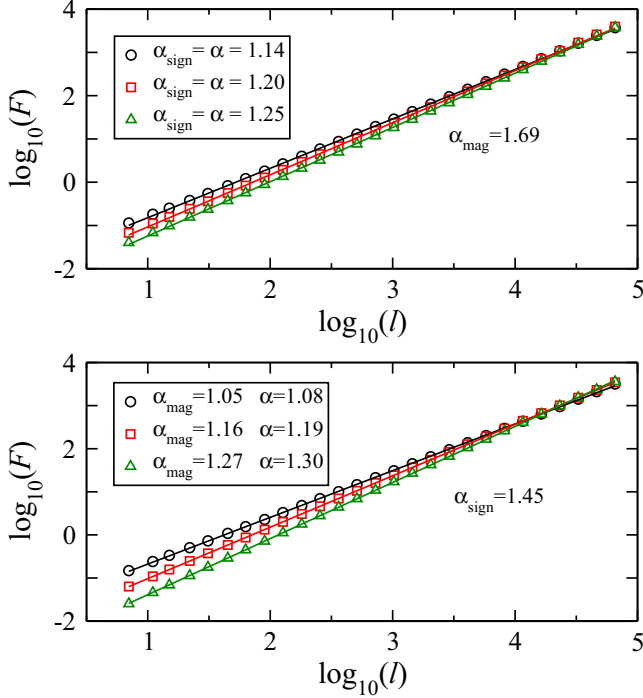


FIG. 9. Example of composed series generated by multiplying sign and magnitude from independent original series for $\alpha_{\text{mag}} > 1$ and $\alpha_{\text{sign}} > 1$. In this region we do not observe crossover (see text). (a) Example of series with $\alpha_{\text{sign}} < \alpha_{\text{mag}}$. The exponent of correlation of the composed series reaches the value α_{sign} ($\min\{\alpha_{\text{mag}}, \alpha_{\text{sign}}\}$) for each series. (b) Example of series with $\alpha_{\text{sign}} > \alpha_{\text{mag}}$. The correlations in the composed series are mainly controlled by those in the magnitude, although the exponent of correlation is slightly higher. This effect becomes more noticeable as the difference between both magnitude and sign exponents of correlation decreases because in these cases, the crossover is less sharp, thus there is a small contribution of the regime after the transition.

In order to find out the values of ℓ_c we have systematically generated pairs of correlated series of signs and magnitudes with $\alpha_{\text{mag}} \in (1, 2)$ and $\alpha_{\text{sign}} \in (1, 1.5)$, and for each of them we obtain $\alpha_{\text{mag}}, \alpha_{\text{sign}}, B_{\text{mag}}$, and B_{sign} and evaluate ℓ_c by using (32). We find two different regions (Fig. 9):

- (i) $\alpha_{\text{mag}} \geq \alpha_{\text{sign}}$. In this case, in all experiments we obtain $\ell_c > N$, implying that the crossover is not reachable.
- (ii) $\alpha_{\text{mag}} < \alpha_{\text{sign}}$. Here in a few situations we obtain $\ell_c \leq N$ although the values of $F_{\text{mag}}(\ell)$ and $F_{\text{sign}}(\ell)$ are too close to display a clear crossover. In addition, only values of $\ell_c \leq N/10$ can be observed in practice because DFA is computed, as usual, up to $N/10$ [17].

In conclusion, we barely observe crossovers within this region, and the composed series will show a single scaling in the whole range, the correlation exponent being $\alpha = \alpha_1 \simeq \min\{\alpha_{\text{mag}}, \alpha_{\text{sign}}\}$.

Another conclusion we can extract from this case is that it is not possible to generate series with an exponent of correlation greater than $\alpha = 1.5$ when composing series by means of independent magnitudes and signs. We try to obtain the greatest possible exponent for composed series, by using $\alpha_{\text{in}} = 2$ for the magnitude ($\alpha_{\text{mag}} \simeq 1.9$) and $\alpha_{\text{in}} = 2$ for the

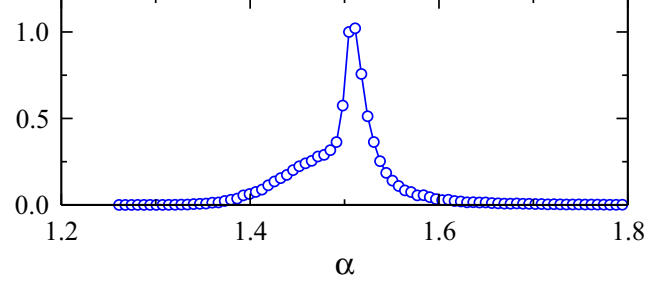


FIG. 10. Distribution of exponents of series obtained with $\alpha_{\text{mag}} \simeq 1.9$ and $\alpha_{\text{sign}} \simeq 1.5$. The size of the series is 2^{20} , and results are averaged over 10^5 series.

sign ($\alpha_{\text{sign}} \simeq 1.5$). Then we compose each pair of magnitude and sign series, obtain α of the composed series, and represent the distribution. The results (Fig. 10) show a distribution with a sharp peak at $\alpha = 1.5$ ($\min\{\alpha_{\text{mag}}, \alpha_{\text{sign}}\}$) in agreement with what we explained previously. By visual inspection, the few series we have observed with $\alpha > 1.5$ correspond to situations where the scaling of the composed series is not very good, together with those few situations where the crossover is observable. Last, Table I summarizes the results obtained in this section.

V. MULTIFRACTAL PROPERTIES OF COMPOSED SERIES

In the previous section we studied only linear correlations of the composed series. However, it has been reported [4,5] that series with correlated magnitude ($\alpha_{\text{mag}} > 0.5$) and uncorrelated sign ($\alpha_{\text{sign}} = 0.5$) also present nonlinear correlations (multifractal properties). Thus, in this section we analyze the multifractal properties of the composed series.

However, our results for composed series presented in Sec. IV indicate the existence of crossovers in the scaling at ℓ_c whenever $\alpha_{\text{sign}} > 1$. Such behavior could lead to the existence of two different multifractal spectra below and above ℓ_c . Furthermore, it is not even guaranteed that $\ell_c = \text{const}$ for the different moments of order q , thus precluding a straightforward calculation of both spectra.

For this reason, we restrict ourselves to the regime $\alpha_{\text{sign}} < 1$ where, first, the composed time series possesses single scaling and, second, the linear correlations in the composed time series are directly controlled by the sign series ($\alpha = \alpha_{\text{sign}}$). In addition, we have observed that when $\alpha_{\text{mag}} > 1.2$, there are numerical instabilities when calculating the multifractal spectra of composed series. Then we study here the multifractal

TABLE I. Results obtained for composition of independent magnitudes and signs.

α_{sign}	α_{mag}	α	Crossover
< 1	$[0.5, 2]$	α_{sign}	No
> 1	< 1	$\ell < \ell_c \alpha_1 = \alpha_{\text{mag}}$	$\ell_c \propto N^k$
		$\ell > \ell_c \alpha_2 = \alpha_{\text{sign}}$	$k = \frac{\alpha_{\text{sign}} - 1}{\alpha_{\text{sign}} - \alpha_{\text{mag}}}$
> 1	> 1	$\min\{\alpha_{\text{mag}}, \alpha_{\text{sign}}\}$	Not observable

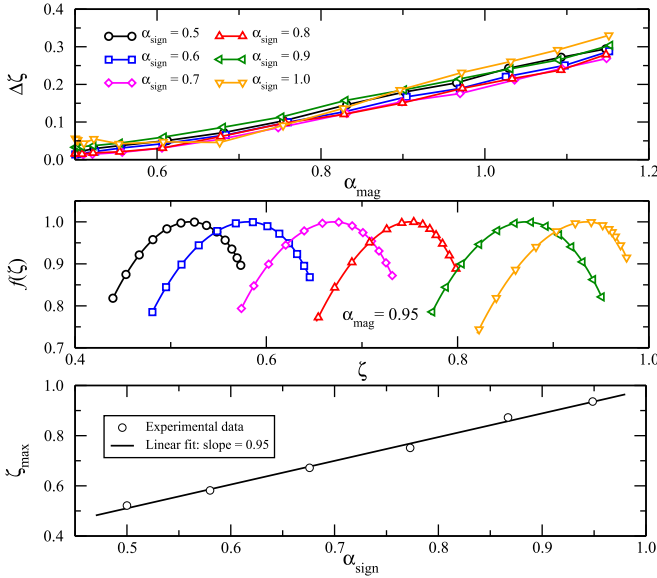


FIG. 11. (a) Relation between $\Delta\zeta$ and α_{mag} of composed series by means of independent magnitudes and signs. $\Delta\zeta$ increases linearly with α_{mag} when the magnitude series leave the uncorrelated regime ($\alpha_{\text{mag}} > 0.5$), whereas α_{sign} does not play an important role in the value of $\Delta\zeta$. Series are 2^{18} long, and results are averaged over an ensemble of 50 series. (b) Example of multifractal spectra of 2^{18} long series with $\alpha_{\text{mag}} = 0.95$ and α_{sign} in the interval $[0.5, 1]$. To obtain the multifractal spectra, the MFDFA analysis (5) has been carried out for moments $q \in [-5, 5]$. Despite varying α_{sign} , $\Delta\zeta$ is practically the same for all cases. Spectra are centered in $\zeta_{\text{max}} \simeq \alpha_{\text{sign}}$. (c) Relation between α_{sign} and ζ_{max} for the multifractal spectra obtained in (b). The data were linearly fitted with slope 0.95.

properties of composed time series with α_{mag} and α_{sign} in the intervals $[0.5, 1.2]$ and $[0.5, 1]$ respectively.

Specifically, we calculate the multifractal spectrum for each composed series using MFDFA (see Sec. II B) and study systematically two properties: the width of the multifractal spectrum, $\Delta\zeta$, and the location of its center, ζ_{max} .

Concerning the properties of the spectral width, we observe that $\Delta\zeta$ depends only on α_{mag} , and it is practically independent of the α_{sign} value. Both properties are shown in Fig. 11(a), where we also notice that the dependence of $\Delta\zeta$ on α_{mag} is essentially linear. This is an interesting property: given an input α_{mag} value in the composition, we control directly the strength of the nonlinearities of the composed time, since such strength is quantified by $\Delta\zeta$.

We also study how the linear correlations present in the composed series, which are controlled by α_{sign} ($\alpha = \alpha_{\text{sign}}$), affect the location of the center of the multifractal spectrum, ζ_{max} . We observe that, for a fixed α_{mag} value (and then for constant $\Delta\zeta$), the whole multifractal spectrum is displaced proportionally to the α_{sign} value [see Fig. 11(b)]. Indeed, if we calculate numerically the location of the center of the spectrum, ζ_{max} , we obtain a very good linear dependence of ζ_{max} on α_{sign} [Fig. 11(c)], with slope $\simeq 1$.

In conclusion, the multifractal properties of composed time series obtained by multiplying independent magnitude and signs are completely controlled by only two parameters, the correlation exponents α_{sign} and α_{mag} . While the first one

controls the linear correlations of the composed series (α) and the location of the center of the multifractal spectrum (ζ_{max}), the second quantifies the width of the spectrum ($\Delta\zeta$) and then the strength of the nonlinearities in the composed series. Obviously this procedure can be used as an algorithm for the generation of complex artificial time series possessing not only prescribed linear long-range correlations (as FFM) but also controlled multifractal properties.

VI. CONCLUSIONS

We have presented a systematic study of the correlation properties of the decomposition of artificial long-range power-law linearly correlated time series into their magnitude and sign series as well as the correlation properties, including nonlinear ones, of the composed series obtained as products of independent magnitude and sign series.

Regarding the decomposition problem, we have studied the correlations of the magnitude and sign of a variety of fractional Gaussian noises and fractional Brownian motions generated by means of the Fourier Filtering Method, one of the most widely used to generate artificial linear correlated series. The results are summarized in Fig. 3. In addition, we have obtained analytical expressions for the correlation exponent of the sign series α_{sign} [Eq. (16)]. In particular, we show that $\alpha_{\text{sign}} \leq 3/2$ independently of the correlations of the original series. These results, together with those obtained here numerically for the magnitude shown in Fig. 3 (also in agreement with Kalisky *et al.* [5] for the square of the series), will be of great help in order to model surrogate time series. For example, the sign series obtained from the decomposition are often used to generate correlated binary series in the study of DNA sequences [13,25,30] or disordered binary solids [33] as well as to generate distributions of first-passage times of correlated series [6]. It is also worth mentioning that, following the results shown in Sec. III, it is clear that long-range anticorrelated binary sequences cannot be obtained using this method, a drawback shared with other methods [26–28].

Apart from the utility of the decomposition to generate surrogate series, the comparison of the results obtained here for artificial linear series with those obtained from real data would help to unveil the existence of coupling in the mechanisms responsible for the magnitude and sign of the increments or to discard it. This information is instrumental for the study of the underlying processes generating complex nonlinear time series such as those obtained from physiological systems.

By means of the composition, we studied the correlations in series obtained as the product of independent series of correlated magnitudes and signs.

First, we explore the linear correlations as measured by the DFA exponent and find that, only for those composed series with $\alpha_{\text{sign}} < 1$, we obtain a scale-free behavior, i.e., a fit to a single power law of $F(\ell)$ in the whole range. In addition, the correlation exponent of the composition is given by α_{sign} independently of α_{mag} . On the other hand, for $\alpha_{\text{sign}} \geq 1$, we observe clear crossovers for $\alpha_{\text{mag}} < 1$ whose position, ℓ_c , can be obtained analytically [Eq. (27)]. Here the composed signal scales with $\alpha_1 \simeq \alpha_{\text{mag}}$ for $\ell < \ell_c$ whereas for $\ell > \ell_c$ it scales with $\alpha_2 \simeq \alpha_{\text{sign}}$. For $\alpha_{\text{mag}} \geq 1$ we show that the crossovers, although theoretically predicted, are difficult

to detect in practice and the composed signal approximately scales with a single exponent given by $\alpha_1 = \min\{\alpha_{\text{mag}}, \alpha_{\text{sign}}\}$. As a consequence of this and taking into account that $\alpha_{\text{sign}} \leq 3/2$, the composition cannot produce signals with correlation exponents above $3/2$. Results are summarized in Table I.

Finally, we analyze the nonlinear properties of the composed signals by means of MFDFA in the region $\alpha_{\text{sign}} < 1$. As a measure of the nonlinearity in the signal we use the width of the multifractal exponent ($\Delta\zeta$) and show that it grows almost linearly with α_{mag} , thus indicating that the nonlinear properties of the composed signals are controlled by the correlations in the magnitude. In addition, we also find that $\Delta\zeta$ is independent of α_{sign} . This last result is interesting because it means that we can generate surrogate signals for which we can fix both the linear correlations (α_{sign}) and the strength of the nonlinearity ($\Delta\zeta$).

ACKNOWLEDGMENTS

This work is partially supported by grants FQM-7964 from the Spanish Junta de Andalucía and FIS2012-36282 from the Spanish Government. We acknowledge support from the W. M. Keck Foundation, National Institutes of Health (NIH Grant No. 1R01-HL098437), Office of Naval Research (ONR Grant No. 000141010078), and US-Israel Binational Science Foundation (BSF Grant No. 2012219).

APPENDIX A: FLUCTUATIONS OF THE SIGN OF NONSTATIONARY SERIES ($\alpha \geq 1$)

Let us consider a long-range fractal correlated series with $\alpha \geq 1$ (fBM), if we denote as x the size of a segment without changes of sign inside it (i.e., segments of constant sign, or simply “segments”), it is known [6] that the distribution of x follows a power law with exponent $\alpha - 3$, which, once normalized, can be written as

$$p(x) = \frac{(2-\alpha)N^{2-\alpha}}{N^{2-\alpha}-1}x^{\alpha-3}. \quad (\text{A1})$$

The mean value $\langle x \rangle$ of the constant-sign segments will be given by

$$\langle x \rangle = \int_1^N p(x) dx = \left(\frac{2-\alpha}{\alpha-1} \right) \frac{N - N^{2-\alpha}}{N^{2-\alpha} - 1}, \quad (\text{A2})$$

and the mean number of such segments inside a series of length N :

$$n = \frac{N}{\langle x \rangle} = \left(\frac{\alpha-1}{2-\alpha} \right) \frac{N^{2-\alpha} - 1}{1 - N^{1-\alpha}}. \quad (\text{A3})$$

When evaluating the fluctuations at a given window size ℓ , only the portion of the signal covered by segments with $x < \ell$ will give a nonzero contribution: for the remainder of the signal the full window of size ℓ will be located inside a segment of constant sign, and then without internal fluctuation and its contribution to $F_{\text{sign}}(\ell)$ will be zero [34].

In order to evaluate the portion of the signal covered by segments with $x < \ell$, first we evaluate the probability that a given segment is smaller than ℓ :

$$P(x < \ell) = \int_1^\ell p(x) dx = 1 - \frac{N^{2-\alpha} - \ell^{2-\alpha}}{\ell^{2-\alpha}[N^{2-\alpha} - 1]}, \quad (\text{A4})$$

the average size of those segments,

$$\langle x_{<\ell} \rangle = \frac{\int_1^\ell x p(x) dx}{P(x < \ell)} = \left(\frac{2-\alpha}{\alpha-1} \right) \frac{\ell^{\alpha-1} - 1}{1 - \ell^{\alpha-2}}, \quad (\text{A5})$$

and the fraction of the series covered by segments with $x < \ell$:

$$f(x < \ell) = \frac{n P(x < \ell) \langle x_{<\ell} \rangle}{N} = \frac{\ell^{\alpha-1} - 1}{N^{\alpha-1} - 1} \simeq \frac{\ell^{\alpha-1}}{N^{\alpha-1}}. \quad (\text{A6})$$

If we denote by i the number of 1's in a window of size ℓ it is straightforward to obtain that the variance of the window is given by

$$\text{var}(i, \ell) = \frac{4i}{\ell} - \frac{4i^2}{\ell^2}. \quad (\text{A7})$$

Taking into account that for N large enough we will find all possible values of $i \in \{1, 2, \dots, \ell - 1\}$, we can assume that the averaged variance in windows of size ℓ located within segments with $x < \ell$ will be

$$\begin{aligned} \text{var}(\ell) &= f(x < \ell) \langle \text{var}(i, \ell) \rangle_i \\ &= \frac{\ell^{\alpha-1}}{N^{\alpha-1}} \frac{1}{\ell-1} \left(\frac{2}{3}\ell - \frac{2}{3\ell} \right) \propto \left(\frac{\ell}{N} \right)^{\alpha-1}, \end{aligned} \quad (\text{A8})$$

and the average standard deviation inside windows of size ℓ

$$\sigma(\ell) = \sqrt{\text{var}(\ell)} \propto \left(\frac{\ell}{N} \right)^{\frac{\alpha-1}{2}}. \quad (\text{A9})$$

$F_{\text{sign}}(\ell)$ measures the rms fluctuations of the integrated signal with respect to ℓ and then

$$F_{\text{sign}}(\ell) \propto \sigma(\ell) \ell \propto \frac{\ell^{\frac{1}{2}(\alpha+1)}}{N^{\frac{1}{2}(\alpha-1)}} = \frac{\ell^{\alpha_{\text{sign}}}}{N^{\alpha_{\text{sign}}-1}}, \quad (\text{A10})$$

where $\alpha_{\text{sign}} = \frac{1}{2}(\alpha + 1)$ is the DFA exponent of the sign series for $1 \leq \alpha < 2$.

For higher values of α equations from (A1) to (A3) are no longer valid [6] and now the number of segments, n , is constant and independent of N . For a given window length ℓ , only n out of N/ℓ windows will contribute with nonvanishing variance, and thus we can write

$$\begin{aligned} \text{var}(\ell) &= \frac{n\ell}{N} \langle \text{var}(i, \ell) \rangle_i \\ &= \frac{n\ell}{N} \frac{1}{\ell-1} \left(\frac{2}{3}\ell - \frac{2}{3\ell} \right) \propto \frac{\ell}{N}, \end{aligned} \quad (\text{A11})$$

$$F_{\text{sign}}(\ell) \propto \frac{\ell^{\frac{3}{2}}}{N^{\frac{1}{2}}} = \frac{\ell^{\alpha_{\text{sign}}}}{N^{\alpha_{\text{sign}}-1}}, \quad (\text{A12})$$

where $\alpha_{\text{sign}} = \frac{3}{2}$ is the DFA exponent of the sign series for $\alpha \geq 2$.

Note that both results [Eqs. (A10) and (A12)], agree with the fact that the fluctuations in a nonstationary series should depend on the size of the series, N .

APPENDIX B: AUTOCORRELATION FUNCTION OF A TIME SERIES WITH UNCOUPLED MAGNITUDE AND SIGN

The autocorrelation function of a time series $\{x_i\}$ at distance ℓ , normally distributed with zero mean and unit standard

deviation, is given by

$$C(\ell) = \frac{\langle x_i x_{i+\ell} \rangle - \langle x_i \rangle \langle x_{i+\ell} \rangle}{\sigma^2} = \langle x_i x_{i+\ell} \rangle, \quad (\text{B1})$$

where $\langle \cdot \rangle$ denotes average over the series. Obviously we can write

$$C(\ell) = \langle \text{sgn}(x_i) |x_i| \text{sgn}(x_{i+\ell}) |x_{i+\ell}| \rangle, \quad (\text{B2})$$

$$C(\ell) = \langle \text{sgn}(x_i) \text{sgn}(x_{i+\ell}) |x_i x_{i+\ell}| \rangle, \quad (\text{B3})$$

where $\text{sgn}(\cdot)$ denotes the sign function. If we consider that *magnitude and sign are not coupled* (i.e., they are independent random variables) we can assume that

$$C(\ell) = \langle \text{sgn}(x_i) \text{sgn}(x_{i+\ell}) \rangle \langle |x_i x_{i+\ell}| \rangle, \quad (\text{B4})$$

$$C(\ell) = C_{\text{sign}}(\ell) \langle |x_i x_{i+\ell}| \rangle, \quad (\text{B5})$$

where $C_{\text{sign}}(\ell)$ is the autocorrelation function at distance ℓ of the sign time series. On the other hand, we can write for the autocorrelation function of the magnitude time series:

$$C_{\text{mag}}(\ell) = \frac{\langle |x_i x_{i+\ell}| \rangle - \langle |x_i| \rangle \langle |x_{i+\ell}| \rangle}{\langle |x_i|^2 \rangle - \langle |x_i| \rangle^2}, \quad (\text{B6})$$

and, taking into account that $\{x_i\}$ are normally distributed with zero mean and unit variance, it follows that

$$\langle |x_i| \rangle = \sqrt{\frac{2}{\pi}} \quad \text{and} \quad \langle |x_i|^2 \rangle = 1. \quad (\text{B7})$$

Replacing in Eq. (B6) we get

$$\langle |x_i x_{i+\ell}| \rangle = \frac{(\pi - 2)C_{\text{mag}}(\ell) + 2}{\pi}, \quad (\text{B8})$$

and finally replacing $\langle |x_i x_{i+\ell}| \rangle$ in Eq. (B4):

$$C(\ell) = C_{\text{sign}}(\ell) \frac{(\pi - 2)C_{\text{mag}}(\ell) + 2}{\pi}. \quad (\text{B9})$$

-
- [1] P. Ch. Ivanov *et al.*, Multifractality in human heartbeat dynamics, *Nature (London)* **399**, 461 (1999).
- [2] P. C. Ivanov *et al.*, Sleep-wake differences in scaling behavior of the human heartbeat: Analysis of terrestrial and long-term spacial flight data, *Europhys. Lett.* **48**, 594 (1999).
- [3] Y. Ashkenazy, P. C. Ivanov, S. Havlin, C.-K. Peng, A. L. Goldberger, and H. E. Stanley, Magnitude and Sign Correlations in Heartbeat Fluctuations, *Phys. Rev. Lett.* **86**, 1900 (2001).
- [4] Y. Ashkenazy *et al.*, Magnitude and sign scaling in power-law correlated time series, *Physica A* **323**, 19 (2003).
- [5] T. Kalisky, Y. Ashkenazy, and S. Havlin, Volatility of linear and nonlinear time series, *Phys. Rev. E* **72**, 011913 (2005).
- [6] C. Carretero-Campos, P. Bernaola-Galván, P. Ch. Ivanov, and P. Carpena, Phase transitions in the first-passage time of scale-invariant correlated processes, *Phys. Rev. E* **85**, 011139 (2012).
- [7] L. Zhu *et al.*, Magnitude and sign correlations in conductance fluctuations of horizontal oil water two-phase flow, *J. Phys. Conf. Ser.* **364**, 012067 (2012).
- [8] H. A. Makse, G. W. Davies, S. Havlin, P. Ch. Ivanov, P. R. King, and H. E. Stanley, Long-range correlations in permeability fluctuations in porous rock, *Phys. Rev. E* **54**, 3129 (1996).
- [9] H. A. Makse, S. Havlin, P. Ch. Ivanov, P. R. King, S. Prakash, and H. E. Stanley, Pattern formation in sedimentary rocks: Connectivity, permeability, and spatial correlations, *Physica A* **233**, 587 (1996).
- [10] I. Bartos and I. M. Jánosi, Nonlinear correlations of daily temperature records over land, *Nonlin. Processes Geophys.* **13**, 571 (2006).
- [11] Q. Li, Z. Fu, N. Yuan, and F. Xie, Effects of non-stationarity on the magnitude and sign scaling in the multi-scale vertical velocity increment, *Physica A* **410**, 9 (2014).
- [12] Y. Liu, P. Gopikrishnan, P. Cizeau, M. Meyer, C. K. Peng, and H. E. Stanley, Statistical properties of the volatility of price fluctuations, *Phys. Rev. E* **60**, 1390 (1999).
- [13] C.-K. Peng, S. V. Buldyrev, S. Havlin, M. Simons, H. E. Stanley, and A. L. Goldberger, Mosaic organization of DNA nucleotides, *Phys. Rev. E* **49**, 1685 (1994).
- [14] P. Allegrini, M. Barbi, P. Grigolini, and B. J. West, Dynamical model for DNA sequences, *Phys. Rev. E* **52**, 5281 (1995).
- [15] G. M. Molchan, Maximum of fractional Brownian motion: Probabilities of small values, *Comm. Math. Phys.* **205**, 97 (1999).
- [16] G. Rangarajan and M. Z. Ding, Integrated approach to the assessment of long range correlation in time series data, *Phys. Rev. E* **61**, 4991 (2000).
- [17] K. Hu, P. C. Ivanov, Z. Chen, P. Carpena, and H. E. Stanley, Effect of trends on detrended fluctuation analysis, *Phys. Rev. E* **64**, 011114 (2001).
- [18] L. Xu, P. C. Ivanov, K. Hu, Z. Chen, A. Carbone, and H. E. Stanley, Quantifying signals with power-law correlations: A comparative study of detrended fluctuation analysis and detrended moving average techniques, *Phys. Rev. E* **71**, 051101 (2005).
- [19] Q. D. Y. Ma, R. P. Bartsch, P. Bernaola-Galván, M. Yoneyama, and P. C. Ivanov, Effects of extreme data loss on detrended fluctuation analysis, *Phys. Rev. E* **81**, 031101 (2010).
- [20] Z. Chen, P. C. Ivanov, K. Hu, and H. E. Stanley, Effect of nonstationarities on detrended fluctuation analysis, *Phys. Rev. E* **65**, 041107 (2002).
- [21] Z. Chen, K. Hu, P. Carpena, P. Bernaola-Galvan, H. E. Stanley, and P. C. Ivanov, Effect of nonlinear filters on detrended fluctuation analysis, *Phys. Rev. E* **71**, 011104 (2005).
- [22] Y. Xu *et al.*, Effects of coarse-graining on the scaling behavior of long-range correlated and anti-correlated signals, *Physica A* **390**, 4057 (2010).
- [23] J. W. Kantelhardt *et al.*, Multifractal detrended fluctuation analysis of nonstationary time series, *Physica A* **316**, 87 (2002).
- [24] H. A. Makse, S. Havlin, M. Schwartz, and H. E. Stanley, Method for generating long-range correlations for large systems, *Phys. Rev. E* **53**, 5445 (1996).
- [25] P. Bernaola-Galván, J. L. Oliver, M. Hackenberg, A. V. Coronado, P. Ch. Ivanov, and P. Carpena, Segmentation of time series with long-range fractal correlations, *Eur. Phys. J. B* **85**, 211 (2012).

- [26] F. M. Izrailev, A. A. Krokhin, N. M. Makarov, and O. V. Usatenko, Generation of correlated binary sequences from white noise, *Phys. Rev. E* **76**, 027701 (2007).
- [27] O. V. Usatenko, S. S. Melnik, S. S. Apostolov, N. M. Makarov, and A. A. Krokhin, Iterative method for generating correlated binary sequences, *Phys. Rev. E* **90**, 053305 (2014).
- [28] S. Hod and U. Keshet, Phase transition in random walks with long-range correlations, *Phys. Rev. E* **70**, 015104(R) (2004).
- [29] S. S. Apostolov, F. M. Izrailev, N. M. Makarov, Z. A. Mayzelis, S. S. Melnyk, and O. V. Usatenko, The Signum function method for the generation of correlated dichotomic chains, *J. Phys. A: Math. Theor.* **41**, 175101 (2008).
- [30] P. Bernaola-Galván, P. Carpena, R. Roman-Roldán, and J. L. Oliver, Study of statistical correlations in DNA sequences, *Gene* **300**, 105 (2002).
- [31] P. Carpena, J. Aguiar, P. Bernaola-Galván, and C. Carnero-Ruiz, Problems Associated with the treatment of conductivity-concentration data in surfactant solutions: Simulations and experiments, *Langmuir* **18**, 6054 (2002).
- [32] J. W. Kantelhardt, S. Russ, A. Bunde, S. Havlin, and I. Webman, Comment on “Delocalization in the 1D Anderson model with long-range correlated disorder,” *Phys. Rev. Lett.* **84**, 198 (2000).
- [33] P. Carpena, P. Bernaola-Galván, P. Ch. Ivanov, and H. E. Stanley, Metal-insulator transition in chains with correlated disorder, *Nature (London)* **418**, 955 (2002).
- [34] To be precise, for each segment of constant sign with $x > \ell$ we will have at most two windows that partially belong to the segment, but, especially for $\alpha > 1$, this effect will be negligible.

[Free Full Text from Publisher](#)

Save to EndNote online

[Add to Marked List](#)

119 of 127

Magnitude and sign of long-range correlated time series: Decomposition and surrogate signal generation

By: Gomez-Extremera, M (Gomez-Extremera, Manuel)^[1]; Carpena, P (Carpena, Pedro)^[1]; Ivanov, PC (Ivanov, Plamen Ch.)^[2,3,4,5]; Bernaola-Galvan, PA (Bernaola-Galvan, Pedro A.)^[1]

[View ResearcherID and ORCID](#)

PHYSICAL REVIEW E

Volume: 93 Issue: 4

Article Number: 042201

DOI: 10.1103/PhysRevE.93.042201

Published: APR 4 2016

Document Type: Article

[View Journal Impact](#)

Abstract

We systematically study the scaling properties of the magnitude and sign of the fluctuations in correlated time series, which is a simple and useful approach to distinguish between systems with different dynamical properties but the same linear correlations. First, we decompose artificial long-range power-law linearly correlated time series into magnitude and sign series derived from the consecutive increments in the original series, and we study their correlation properties. We find analytical expressions for the correlation exponent of the sign series as a function of the exponent of the original series. Such expressions are necessary for modeling surrogate time series with desired scaling properties. Next, we study linear and nonlinear correlation properties of series composed as products of independent magnitude and sign series. These surrogate series can be considered as a zero-order approximation to the analysis of the coupling of magnitude and sign in real data, a problem still open in many fields. We find analytical results for the scaling behavior of the composed series as a function of the correlation exponents of the magnitude and sign series used in the composition, and we determine the ranges of magnitude and sign correlation exponents leading to either single scaling or to crossover behaviors. Finally, we obtain how the linear and nonlinear properties of the composed series depend on the correlation exponents of their magnitude and sign series. Based on this information we propose a method to generate surrogate series with controlled correlation exponent and multifractal spectrum.

Keywords

KeyWords Plus: SCALING BEHAVIOR; HUMAN HEARTBEAT; DNA-SEQUENCES; FLUCTUATIONS; PERMEABILITY; DISORDER; MODEL

Author Information

Reprint Address: Gomez-Extremera, M (reprint author)

+ Univ Malaga, ETSI Telecomunicac, Dept Fis Aplicada 2, E-29071 Malaga, Spain.

Addresses:

+ [1] Univ Malaga, ETSI Telecomunicac, Dept Fis Aplicada 2, E-29071 Malaga, Spain

+ [2] Boston Univ, Dept Phys, Keck Lab Network Physiol, Boston, MA 02215 USA

+ [3] Harvard Univ, Sch Med, Boston, MA 02115 USA

+ [4] Brigham & Womens Hosp, Div Sleep Med, Boston, MA 02115 USA

Citation Network

In Web of Science Core Collection

8

Times Cited



[Create Citation Alert](#)

All Times Cited Counts

8 in All Databases

[See more counts](#)

33

Cited References

[View Related Records](#)

Most recently cited by:

Racz, Frigyes Samuel; Mukli, Peter; Nagy, Zoltan; et al.

[Multifractal dynamics of resting-state functional connectivity in the prefrontal cortex.](#)

PHYSIOLOGICAL MEASUREMENT (2018)

Qin, Yu-Hao; Zhao, Zhi-Dan; Cai, Shi-Min; et al.

[Dual-induced multifractality in online viewing activity.](#)

CHAOS (2018)

[View All](#)

Use in Web of Science

Web of Science Usage Count

1

Last 180 Days

8

Since 2013

[Learn more](#)

This record is from:

Web of Science Core Collection

[View Record in Other Databases:](#)

[View medical data \(in MEDLINE®\)](#)

+ [5] Bulgarian Acad Sci, Inst Solid State Phys, BU-1784 Sofia, Bulgaria

Suggest a correction

If you would like to improve the quality of the data in this record, please [suggest a correction](#).

Funding

Funding Agency	Grant Number
Spanish Junta de Andalucia	FQM-7964
Spanish Government	FIS2012-36282
W. M. Keck Foundation	
National Institutes of Health (NIH)	1R01-HL098437
Office of Naval Research (ONR)	000141010078
US-Israel Binational Science Foundation (BSF)	2012219

[View funding text](#)

Publisher

AMER PHYSICAL SOC, ONE PHYSICS ELLIPSE, COLLEGE PK, MD 20740-3844 USA

Journal Information

Impact Factor: [Journal Citation Reports](#)

Categories / Classification

Research Areas: Physics

Web of Science Categories: Physics, Fluids & Plasmas; Physics, Mathematical

[See more data fields](#)

◀ 119 of 127 ▶

Cited References: 33

Showing 30 of 33 [View All in Cited References page](#)

(from Web of Science Core Collection)

- DYNAMICAL MODEL FOR DNA-SEQUENCES** **Times Cited: 76**
 By: ALLEGRINI, P; BARBI, M; GRIGOLINI, P; et al.
 PHYSICAL REVIEW E Volume: 52 Issue: 5 Pages: 5281-5296 Part: B Published: NOV 1995
- The Signum function method for the generation of correlated dichotomic chains** **Times Cited: 9**
 By: Apostolov, S. S.; Izrailev, F. M.; Makarov, N. M.; et al.
 JOURNAL OF PHYSICS A-MATHEMATICAL AND THEORETICAL Volume: 41 Issue: 17 Article Number: 175101 Published: MAY 2 2008
- Magnitude and sign scaling in power-law correlated time series** **Times Cited: 108**
 By: Ashkenazy, Y; Havlin, S; Ivanov, PC; et al.
 PHYSICA A-STATISTICAL MECHANICS AND ITS APPLICATIONS Volume: 323 Pages: 19-41 Published: MAY 15 2003
- Magnitude and sign correlations in heartbeat fluctuations** **Times Cited: 299**
 By: Ashkenazy, Y; Ivanov, PC; Havlin, S; et al.
 PHYSICAL REVIEW LETTERS Volume: 86 Issue: 9 Pages: 1900-1903 Published: FEB 26 2001
- Nonlinear correlations of temperature records over land, Nonlin** **Times Cited: 1**
 By: Bartos, I.; Janosi, I. M.
 Processes Geophys Volume: 571 Published: 2006

Focus on the emerging new fields of network physiology and network medicine

This content has been downloaded from IOPscience. Please scroll down to see the full text.

2016 New J. Phys. 18 100201

(<http://iopscience.iop.org/1367-2630/18/10/100201>)

View [the table of contents for this issue](#), or go to the [journal homepage](#) for more

Download details:

IP Address: 128.197.42.69

This content was downloaded on 18/10/2016 at 20:53

Please note that [terms and conditions apply](#).

You may also be interested in:

[Co-controllability of drug-disease-gene network](#)

Peng Gang Sun

[From physics to pharmacology?](#)

Richard J Allen and Timothy C Elston

[The unforeseen challenge: from genotype-to-phenotype in cell populations](#)

Erez Braun

[Network-based association of hypoxia-responsive genes with cardiovascular diseases](#)

Rui-Sheng Wang, William M Oldham and Joseph Loscalzo

[Revealing networks from dynamics: an introduction](#)

Marc Timme and Jose Casadiego

[From functional to structural connectivity using partial correlation in neuronal assemblies](#)

Daniele Poli, Vito Paolo Pastore, Sergio Martinoia et al.

[A review of progress in single particle tracking: from methods to biophysical insights](#)

Carlo Manzo and Maria F Garcia-Parajo

**EDITORIAL****Focus on the emerging new fields of network physiology and network medicine****OPEN ACCESS**PUBLISHED
13 October 2016

Original content from this work may be used under the terms of the [Creative Commons Attribution 3.0 licence](#).

Any further distribution of this work must maintain attribution to the author(s) and the title of the work, journal citation and DOI.

**Plamen Ch Ivanov^{1,2,3,6}, Kang K L Liu^{1,4} and Ronny P Bartsch⁵**¹ Keck Laboratory for Network Physiology, Department of Physics, Boston University, Boston, MA, USA² Harvard Medical School and Division of Sleep Medicine, Brigham and Women Hospital, Boston, MA 02115, USA³ Institute of Solid State Physics, Bulgarian Academy of Sciences, Sofia 1784, Bulgaria⁴ Department of Neurology, Beth Israel Deaconess Medical Center and Harvard Medical School, Boston, Massachusetts, USA⁵ Department of Physics, Bar-Ilan University, Ramat Gan, 5290002, Israel⁶ Editor of the 'focus on' issue.**E-mail:** plamen@buphy.bu.edu**Abstract**

Despite the vast progress and achievements in systems biology and integrative physiology in the last decades, there is still a significant gap in understanding the mechanisms through which (i) genomic, proteomic and metabolic factors and signaling pathways impact vertical processes across cells, tissues and organs leading to the expression of different disease phenotypes and influence the functional and clinical associations between diseases, and (ii) how diverse physiological systems and organs coordinate their functions over a broad range of space and time scales and horizontally integrate to generate distinct physiologic states at the organism level. Two emerging fields, network medicine and network physiology, aim to address these fundamental questions. Novel concepts and approaches derived from recent advances in network theory, coupled dynamical systems, statistical and computational physics show promise to provide new insights into the complexity of physiological structure and function in health and disease, bridging the genetic and sub-cellular level with inter-cellular interactions and communications among integrated organ systems and sub-systems. These advances form first building blocks in the methodological formalism and theoretical framework necessary to address fundamental problems and challenges in physiology and medicine. This 'focus on' issue contains 26 articles representing state-of-the-art contributions covering diverse systems from the sub-cellular to the organism level where physicists have key role in laying the foundations of these new fields.

1. Introduction

A fundamental problem encountered in physical, biological and physiological systems is to quantify and understand phenomena where global behavior across systems emerges out of networked interactions among dynamically-changing entities with coupling forms that are function of time. In the context of systems biology, human physiology and medicine, recent advances in complex networks theory [1, 2] have stimulated and facilitated the development of new fields of research.

Studies initiated by physicists have utilized graph theory and network approaches to cellular interactions to build genetic, protein–protein interaction, metabolic and regulatory networks with the aim to understand the associations between genomic and proteomic factors and disease phenotypes [3–7]. This has led to the emergence of network medicine as a new interdisciplinary field of active research [8–11].

Following the reductionist approach, systems biology has traditionally focused on identifying key elements inside the cell and on establishing their role in cellular function. Recent research in systems biology has been facilitated also by integrative network approaches where graph theory is utilized to obtain knowledge graphs, connecting biological observations of relationships among cell elements, with the aim to uncover complex intra-

cellular signaling pathways and to treat available genomic, proteomic and metabolic information in a generalized systematic way. Thus, fundamental questions related to how genomic and proteomic factors relate to the suppression or expression of particular disease phenotypes have triggered a shift in paradigm leading to the emerging new field of network medicine. Further, this new field has developed novel concepts and methods to establish and predict associations between clusters of different disease phenotypes and shared genes [6, 7, 12]. The network medicine framework made it also possible to define and predict the role of genes and proteins in the expression of a particular disease based on the neighborhood of genes in the network (network motifs and modules), allowing to identify potential new genes that may play role in disease phenotype expression [5, 12–15]. This new perspective led to identification of disease genes based on correlations between their location in the interactome and their network topology.

Establishing functional relationships between the signature of specific genes in the network environment and their potential role in the mechanisms underlying disease phenotype expression is a fundamental breakthrough due to network medicine, as currently only about 10% of all genes have known disease association [16]. The integrative framework of network medicine has helped to further extend genetic and phenotypic networks derived for intra-cellular interactions to account for tissue and organ specificity in gene connectivity and disease association, and to establish principles of gene interactions across cells and tissues [17–20]. More recent developments in network medicine have added another level of integration through layered multiplex networks that combine genetic networks with a wide range of co-morbidity factors to understand their role in modifying the action of disease-causing genes [17] and the likelihood of disease phenotype expression in the presence of other diseases and risk factors [21, 22].

Investigations of intra- and inter-cellular signaling pathways and how alterations in these pathways lead to cascades of failure across protein and metabolic interaction networks opened the way to build the human disease network [23]—a fundamental discovery resulting from network medicine that reveals interrelations and clustering among distinct diseases based on information derived from networks of genomic, proteomic and metabolic interactions [11, 24].

Analytic tools from complex networks theory offer new avenues to systematically explore how cellular components exert their functions through network interactions across cells, tissues and organs in order to elucidate the molecular mechanisms underlying particular diseases and associations between diseases. In turn, the developments and discoveries in network medicine have initiated new directions of research in complex networks, posing new fundamental questions to network theory—for example, the role of individual nodes in network controllability—that require novel mathematical formalism and theoretical framework. Because of the inherent cross-fertilization from biology and medicine to statistical physics and network science, network medicine has emerged as a separate, self-sustained interdisciplinary field.

Advances in network medicine have laid the foundation of the human disease network by connecting microscopic cellular level genomic, proteomic and metabolic networks with human epidemiology at the macroscopic organism level. While systems biology and integrative physiology have focused on the vertical integration from the sub-cellular and cellular level to tissues and organs [25], there is a wide gap of knowledge in the direction of horizontal integration at the level of organ-to-organ interactions. A new field, network physiology, has emerged to fill this gap and to address the fundamental question of how physiological systems coordinate, synchronize and integrate their dynamics to optimize functions and to maintain health. Physiologic interactions occur at multiple levels and spatio-temporal scales to generate distinct physiologic states, e.g., wake and sleep, light and deep sleep, consciousness and unconsciousness. Thus, investigations in network physiology have focused on (i) structural and functional connectivity of physiologic networks underlying individual organ systems and their sub-systems [26–29], and (ii) how global behavior at the organism level, i.e., different physiologic states and functions, arise out of networked interactions among organ systems to generate health or disease [30, 31]. Disrupting organ communications and their dynamical coordination can lead to dysfunction of individual systems or to collapse of the entire organism, e.g., coma, multiple organ failure [32, 33]. Thus, in addition to the traditional approach in physiology that defines health and disease through structural, dynamical and regulatory changes in individual physiological systems, the new conceptual framework of network physiology focuses on the coordination and network interactions among diverse organ systems as a hallmark of physiologic state and function.

Novel computational tools and analytic formalism developed in the field of network physiology have added new rich dimensions to our understanding of physiologic states and functions. The network physiology perspective has redefined physiologic states from point of view of dynamic networks of organ interactions. This has helped establishing first associations of distinct physiologic states and conditions with network topology and with the temporal characteristics of organ interactions (network links) even when network topology remains unchanged [30, 31]. It was discovered that brain-organ interactions have preferred channels of communication (frequency bands) that are specific for each organ [34] and recent efforts in the community by physicists and physiologists that focused on networks of brain–heart interactions identified new aspects of coupling and

feedback mechanisms [35]. By developing the theoretical framework necessary to uncover basic principles of (i) integration among diverse physiologic systems that leads to complex physiologic functions at the organism level, and (ii) hierarchical reorganization of physiological networks and their evolution across states and conditions, investigations in the field of network physiology provide the building blocks of a first atlas of dynamic organ interactions.

Although the interdisciplinary research in both network physiology and network medicine takes advantage of the rapid development in complex networks theory, it is important to note the different focus, philosophy and theoretical problems in these new fields. In general, links in network medicine focus on characterizing statistical correlation and dependency, and research is focused on the global consequences of network topology and structure for identifying the specific role of genomic and proteomic factors in expression of disease phenotypes [11]. In contrast, in network physiology, links represent dynamical coordination between diverse systems and subsystems with transient characteristics, and a fundamental question is how physiologic states and functions emerge out of the collective dynamics of integrated physiological systems [34, 36]. Moreover, markedly different global behaviors can emerge from the same network topology due to minor temporal changes in the functional form of physiologic interactions. This poses new challenges to further develop generalized methodology adequate to quantify complex dynamics of networks where nodes are not identical but represent diverse dynamical systems with diverse forms of coupling which continuously change in time. Because of the new type of problems, the specificity of related challenges and the necessity of new theoretical framework and interdisciplinary efforts, network physiology has developed into a new field of research.

Network physiology and network medicine are not simply an application of established concepts and approaches in complex networks theory to existing fields of biomedical research. Their scope extends far beyond applying knowledge from one field (physics and applied mathematics) to solve problems in another (systems biology, physiology and medicine), and require new computational and analytical approaches to extract information from complex data, to infer transient interactions between dynamically changing systems, and to quantify global behavior at the organism level generated by networks of interactions that are function of time. In fact, in recent years, we have already witnessed the broad impact of introducing novel concepts and methods derived from modern statistical physics and network theory to biology and medicine, shifting the paradigm from reductionism to a new integrative framework essential to address fundamentally new problems in systems biology, neuroscience, physiology, clinical medicine [37] and even drug discovery [38]. A central focus of research within this integrative framework is the interplay between structural connectivity and functional dependency, a key problem in neuroscience and brain research [27, 29]. As a result, new physical models have been motivated and proposed to investigate the dynamical consequences of networks [39–44], which in turn trigger more theoretical questions for statistical physicists. These synergetic effects certainly establish network medicine and network physiology as new fields in the landscape of contemporary biomedical research. Understanding the relationship, conceptual difference, the broad horizon and impact of network physiology and network medicine is important to facilitate an active and productive dialog among physicists, biologists, physiologists, neuroscientists and clinicians, which is the central focus of this special issue.

In recent years, physicists have made significant contributions in both fields of research that led to discoveries with potential for broad clinical applications. This focus issue is a collection of interdisciplinary contributions highlighting new developments at the interface between physics, physiology and medicine, including: novel applications of complex networks theory to ask new questions in systems biology; human disease networks; new physics of synchronization phenomena in networks of oscillators; new insights in neural networks and brain structural and functional connectivity; innovative methods to probe physiological time series from individual systems and the impact of individual systems on the dynamics of the entire physiologic network; dynamical networks of organ systems and functional forms of coupling; and clinical applications derived from networks of physiologic interactions.

2. Network medicine

2.1. New perspectives on systems biology

In contrast to the traditional reductionist approach in systems biology, where focus of investigation is to identify and quantify the role of single molecules, individual genes and separate cellular components, recent advances in complex networks theory allow for a more holistic approach through studies of networks of interacting cellular components across multiple levels, from single molecules, genes and proteins to signaling pathways and functional modules across cells and tissues.

Investigating the chromatin interaction network, Boulos *et al* [45] took advantage of a graphical theoretical approach to uncover ‘master’ replication initiation zones organized at the N/U-domain borders that play key role in the 3D organization of the human DNA. Utilizing a thermodynamic out-of-equilibrium variational

principle approach to cellular metabolic networks, De Martino *et al* [46] identify intracellular flux patterns from extracellular metabolic interactions and the role of non-equilibrium steady states for the function of metabolic networks. Lin *et al* [47] develop a Boolean network framework to investigate the dynamics and function of the p53 regulatory network and the role of this network in tumor suppression, identifying two-phase dynamics in response to DNA damage and oncogene activation. Elucidating the signaling network for a two-cell system, Jolly *et al* [48] provide first insights on the operating principles and communication mechanisms that govern evolutionary processes of cell development and tumor progression. Extending two dimensional elastic springs network models of lung tissue, Oliveira *et al* [49] investigate the formation and growth of isolated regions of collagen deposition in the lung cell network that increase lung tissue stiffness and lead to the progression of pulmonary fibrosis. With a new focus on the mesoscale, Klimm *et al* [50] propose a framework based on a set of graph descriptors to characterize the position that each individual node takes within the modular and hierarchical architecture of complex networks to assess the influence of individual nodes to the global dynamics of the network.

2.2. Towards the human disease network

Network studies in systems biology have initially focused on deriving information from single molecular networks, protein interaction networks, metabolic and regulatory networks. Advances in network theory within the framework of network medicine make it possible to gain new insights into the properties of biological networks more generally. Since cellular signaling processes can spread the effect of a specific genetic abnormality along the network of links by altering the activity of other gene products that carry no defects, disease phenotype is rarely a consequence of an abnormality of a single gene product but reflects a broad range of biological processes that interact in a complex network. Relying on new emerging tools from network and graph theory, recent investigations in network medicine aim to quantify the complex interdependencies among cellular components that lead to functional and causal relationships among distinct disease phenotypes. To address the question of how various human genes associate with different diseases, studies have focused on quantifying network characteristics that distinguish disease genes from others, on detecting correlations between gene network location and local network topology, and on identifying disease modules based on network clustering of disease genes.

Investigating cell regulatory pathways related to hypoxia genes that are responsible for increasing oxygen supply and optimizing cellular metabolism under limited oxygen supply, Wang *et al* [51] employ the network medicine framework to identify modules of hypoxia and cardiovascular disease genes within the human protein interactome. The work leads to new insights on the relationship between hypoxia and cardiovascular diseases and to improved prediction of novel genes that may be associated with cardiovascular disease. Another line of investigations focuses on co-controllability of networks, identifying the minimal set of driver nodes that control an entire network and quantifying mutual control characteristics of multiple networks as encountered in the human interactome. A study by Sun [52] considers a drug–disease–gene network that consist of gene–gene, disease–disease and drug–drug networks to investigate co-controllability among these networks, and to uncover underlying mechanisms of the drug–disease–gene network with applications to disease treatment and drug design.

These works are great examples of the utility of the network medicine framework where a number of questions about signaling pathways, metabolic interactions, regulatory networks and cell/tissue communications can be formulated and investigated in a systematic and integrative way. Moving forward from a single network to interdependent networks (multiplex) while shifting the focus from quantifying structural properties to exploring basic principles of controllability of these networks opens new questions in systems biology that will lead to new theoretical developments in complex networks.

3. Network physiology

3.1. Unique challenges

A different kind of network problems arise when considering the complex dynamics and network interactions among integrated physiological organ systems and sub-systems, which is a focus of investigations in the field of network physiology. Physiological systems under neural regulation exhibit non-stationary, intermittent, scale-invariant and nonlinear behaviors. Their output dynamics transiently change in time with different physiologic states and under pathologic conditions, in response to changes in the underlying control mechanisms. This complexity is further compounded by various coupling and feedback interactions among different systems, the nature of which is not understood. Quantifying these physiologic interactions is a major challenge as (i) the structural and neural control networks that underlie each physiologic organ system include many individual components, connected through nonlinear interactions that lead to high degree of complexity; and (ii) each

integrated physiological system exhibits multiple simultaneous interactions and forms of coupling with other systems, thus forming a network of distinct physiologic networks.

Recent research efforts have focused on temporal networks [53], where traditional graph approaches to static network topology are extended to time-dependent structures, and are employed to investigate new phenomena related to changes in fundamental properties of networks, including the loss of transitivity and the emergence of time ordering of links [53]. However, the inherent complexity of physiological systems and the problems that arise from network physiology are beyond the scope of the current-state-of-the-art in temporal networks. Specifically, current approaches to temporal networks do not account for the complex dynamics of individual physiological systems (network nodes) and for the heterogeneity of physiological networks comprised of diverse systems where coupling forms (individual network links) vary in time. Moreover, the formalism employed in temporal networks requires a well-defined time-scale, which is not adequate for physiologic networks where scale-invariant dynamics and temporal feedbacks over a broad range of time scales are well-known hallmarks of integrated physiological systems. Currently, there is no established analytic instrumentarium and theoretical framework suitable to probe networks comprised of diverse systems with different output dynamics, operating on different time scales, and to quantify dynamic networks of organ interactions from continuous streams of noisy and transient signals.

3.2. New physics in network physiology

To develop adequate tools for network physiology and to probe how physiologic states and functions emerge out of coordinated networked interactions among physiological systems and sub-systems, recent efforts focus on understanding global network behavior and function where network nodes are dynamical in nature and links strength changes in time. Theoretical investigations on networks of nonlinear oscillators provide new insights on emergent synchronization and de-synchronization phenomena, the role of individual node output dynamics on the global behavior of the network, emergence of network sub-clusters with different dynamical behaviors, and effects of noise and perturbations on the state of global network dynamics. In that context, Rothkegel and Lehnertz [54] investigate small-world networks of pulse-coupled integrate-and-fire oscillators to generate global network dynamics characterized by irregular behaviors, and by the formation of separate coexisting and self-organized subnetworks with coordinated patterns of alternating synchronization and de-synchronization, as observed in brain neuronal populations and in organ systems interactions. Combining a theoretical model based on Granger causality with electrophysiology data from epileptic brain and gene expression time series, Stramaglia *et al* [55] investigate the effects of synergy and redundancy in the inference of information flow that characterize interactions in dynamical networks of physiological systems. Traxl *et al* [56] study the effects of noise and global coupling strength on the synchronization patterns in dynamical networks of coupled oscillators with different topologies, and report a general scaling law for the synchronizability of such networks. Adopting the complexity matching principle to coupled networks, Mafahim *et al* [57] investigate critical behavior in networks where nodes are presented by integrate-and-fire models, and highlight the role of inhibitory links in controlling global network dynamics. Employing a dynamical Bayesian inference approach, Stankovski *et al* [58] develop a method suitable to detect and reconstruct effective connectivity of oscillator networks with time-evolving coupling in the presence of noise. Incorporating network dynamics of the decision-making model with a subornation process, West *et al* [59] demonstrate the utility of fractional calculus in describing the dynamics of individual elements in complex networks.

3.3. New approaches and insights to neuroscience

Within the conceptual framework of network physiology, the traditional research paradigms of neural networks and maps that focus on structural and functional brain connectivity are now extended to the dynamical interplay between global network topology and emergent network dynamics to better understand physiologic states and functions as emergent phenomena of integration across space and time scales, from a single neuron to the brain system level. By investigating the structure of neural graphs derived from the brain and the neural systems of different species, Muller *et al* [60] discover that instead of being characterized by maximally small-world topology, neural graphs derived from real systems reside at the borderline regime of small-worldness, close to random graph topology. In the context of spike activity of neural networks, Huang *et al* [61] uncover that spike-timing dependent plasticity facilitates sequence learning, and investigate the key relationship between training and retrieval speed in neural networks. Introducing stochastic delay to a class of Wilson–Cowan models, Goychuk and Goychuk [62] investigate critical avalanche dynamics emerging from a balanced feed-forwarded network of excitatory and inhibitory neurons. Such theoretical approaches provide new mechanistic insights to critical avalanches and self-organized criticality type behavior recently reported in sleep dynamics [63–66] as well as for *in vitro* neuronal groups [67–69]. Employing a network model of three different neuronal populations, Mosqueiro *et al* [70] demonstrate how integrated sleep-wake dynamics and brain communications

can be controlled by orthogonal (e.g. excitatory versus inhibitory) mechanisms of neural transmission, while at the same time reproducing the distinct firing rates of the different neuronal populations. The work opens a new direction to investigate the origin of distinct brain rhythms, and the role of specialized neuronal populations in sleep regulation.

3.4. New data science methodology to probe physiologic interactions

Establishing various forms of dynamical coupling and the mechanisms underlying interactions between pairs of organ systems and their respective structural and regulatory networks is an essential building block in network physiology to investigate how coordinated communications among multiple organ systems integrated as a network lead to distinct physiologic states and conditions. Utilizing phase-dynamics reconstruction analysis on triplets of network nodes, Kralemann *et al* [71] propose a novel approach to detect and quantify directional connectivity in dynamical networks of nonlinear oscillators from multivariate time series data. To probe the network of interaction between the brain and the heart, Faes *et al* [72] propose an information dynamics framework and entropy-based measures to investigate flows of information between these two systems compared to the information stored by each system separately, in order to explore changes in neural regulation across different sleep stages. Time-variant coherence analysis is applied by Piper *et al* [73] to explore the dynamics of the central autonomic network that controls the cardiovascular and cardiorespiratory systems and their interactions with the brain in epileptic patients to quantify the role of epileptic neural networks on sympathetic cardiac control. Advanced signal and image-processing methods to quantify various aspects of brain–heart network interactions within the framework of Network Physiology have been further extended [35] following this focus issue on network medicine and network physiology. Another important question in this line of research is how temporal dynamics of individual network components contribute to global network behavior at the system level. Investigating bursts of activity in networks of neurons, Ferrari *et al* [74] propose a novel approach to determine whether bursting dynamics arise from inherent node properties or emerge as a consequence of integrated network interactions.

4. New clinical applications

The studies discussed above present first steps in adapting and developing data analysis methods and models necessary to address fundamental questions in network physiology and medicine. These pioneering works open new possibilities for broad clinical applications. The network medicine framework is extended to multiplex networks by Chmiel *et al* [75] to build a co-morbidity network of human diseases, and to track the dramatic structural changes this network undergoes across the life time of patients, associated with formation of new disease clusters and hubs within the co-morbidity network. Scala *et al* [76] demonstrate the utility of the novel physiologic network approach to dentistry, and how it can facilitate and improve current diagnostic and dental surgical procedures by deriving network information from interacting co-dependent skeletal and dentoalveolar components. Identifying influential nodes in a wound healing-related network of biological processes using mean first-passage time, Arodz and Bonchev [77] show that the network medicine paradigm can be useful to explore the cell signaling pathways and protein networks involved in the healing of skin wounds. Another clinical application of network physiology is a novel ‘fingerprinting’ method, developed by Fernandes *et al* [78], that combined with whole-brain anatomical parcellation provides a detailed quantitative assessment of deep brain stimulation with implications for Parkinson’s disease and other neurological disorders.

5. Summary and outlook

The interdisciplinary works contributed to this focus issue by leading experts highlight new exciting developments in the emerging fields of network medicine and network physiology. Applications of analytical tools derived from established network theory enable new discoveries in network medicine in relation to the human genome, proteome and metabolome to construct disease networks and track the evolution of co-morbidity associations with aging. In network physiology, novel theoretical works combining nonlinear dynamical systems with distinct forms of time-varying interactions under different network topologies uncover new physics that mimics (i) the complex dynamics observed in many individual organ systems, as well as (ii) emerging global behaviors and integrated functions at the organism level. Both fields show great promise in addressing new challenges arising from rapidly accumulating data and increasing complexity. It is also important to note current limitations, when one explores uncharted territory through the perspectives of these new fields. On one hand, despite many recent advances in network medicine, as presented also in this focus issue, the progress towards a reliable network-based approach to disease is still limited by the incompleteness of the available data on protein–protein interactions, metabolic networks and information of biological regulatory

pathways that are heavily relying on large scale biomedical experiments [11]. Meanwhile, as network medicine moves towards the dynamic interactome [79], it would certainly require new advances in temporal and adaptive networks to probe temporal variations in network topology and function. On the other hand, network physiology is still at an early stage (network building phase), where broad-scale empirical investigations are needed to establish a general framework to identify and define dynamical links among physiological systems, and to construct the specific physiological networks that dictate particular integrative functions. Since physiological systems communicate via complex mechanisms manifested through various functional forms of coupling, there is an urgent need to integrate distinct forms of pair-wise physiologic interactions into a general framework. Overcoming these limitations is challenging but also highly rewarding—uncovering fundamental principles of hierarchical organization, coordination and evolution in networks of physiologic interactions across different levels of integration (from sub-cellular to organism level) will in turn stimulate the development of new data-science methodology to probe complex physiologic dynamics with broad impact on both basic biomedical research and clinical practice.

In summary, the unique challenges, interdisciplinary nature and the complexity involved in these new areas demand physicists with multi-disciplinary background, able to identify unique, specific and physiologically relevant problems, and to introduce adequate computational and analytic formalism. Equipped with the ability to propose minimal models and general mechanisms to generate a variety of emergent macroscopic phenomena from microscopic interactions, physicists have an essential role to play in laying the ground work and building the theoretical framework of network physiology and network medicine.

Acknowledgments

We acknowledge support from W M Keck Foundation, National Institutes of Health (NIH Grant 1R01-HL098437), the Office of Naval Research (ONR Grant 000141010078), the US-Israel Binational Science Foundation (BSF Grant 2012219), EC- FP7 Marie Curie Fellowship (IIF 628159).

References

- [1] Albert R and Barabási A L 2002 Statistical mechanics of complex networks *Rev. Mod. Phys.* **74** 47–97
- [2] Newman M E J 2003 The structure and function of complex networks *SIAM Rev.* **45** 167–256
- [3] Jeong H, Tombor B, Albert R, Oltvai Z N and Barabási A L 2000 The large-scale organization of metabolic networks *Nature* **407** 651–3
- [4] Fraser H B, Hirsh A E, Steinmetz L M, Scharfe C and Feldman M W 2002 Evolutionary rate in the protein interaction network *Science* **296** 750–2
- [5] Stuart J M, Segal E, Koller D and Kim S K 2003 A gene-coexpression network for global discovery of conserved genetic modules *Science* **302** 249–55
- [6] Rzhetsky A, Wajngurt D, Park N and Zheng T 2007 Probing genetic overlap among complex human phenotypes *Proc. Natl Acad. Sci. USA* **104** 11694–9
- [7] Feldman I, Rzhetsky A and Vitkup D 2008 Network properties of genes harboring inherited disease mutations *Proc. Natl Acad. Sci. USA* **105** 4323–8
- [8] Barabási A L 2007 Network medicine—from obesity to the diseasome *N. Engl. J. Med.* **357** 404–7
- [9] Pawson T and Linding R 2008 Network medicine *FEBS Lett.* **582** 1266–70
- [10] Zanzoni A, Soler-López M and Aloy P 2009 A network medicine approach to human disease *FEBS Lett.* **583** 1759–65
- [11] Barabási A-L, Gulbahce N and Loscalzo J 2011 Network medicine: a network-based approach to human disease *Nat. Rev. Genet.* **12** 56–68
- [12] Oti M, Snel B, Huynen M A and Brunner H G 2006 Predicting disease genes using protein–protein interactions *J. Med. Genet.* **43** 691–8
- [13] Milo R, Shen-Orr S, Itzkovitz S, Kashtan N, Chklovskii D and Alon U 2002 Network motifs: simple building blocks of complex networks *Science* **298** 824–7
- [14] Köhler S, Bauer S, Horn D and Robinson P N 2008 Walking the interactome for prioritization of candidate disease genes *Am. J. Hum. Genet.* **82** 949–58
- [15] Song C, Havlin S and Makse H A 2005 Self-similarity of complex networks *Nature* **433** 392–5
- [16] Amberger J, Bocchini C A, Scott A F and Hamosh A 2009 McKusick’s Online Mendelian Inheritance in Man (OMIM) *Nucleic Acids Res.* **37** D793–6
- [17] Reverter A, Ingham A and Dalrymple B P 2008 Mining tissue specificity, gene connectivity and disease association to reveal a set of genes that modify the action of disease causing genes *BioData Mining* **1** 8
- [18] Lage K, Hansen N T, Karlberg E O, Eklund A C, Roque F S, Donahoe P K, Szallasi Z, Jensen T S and Brunak S 2008 A large-scale analysis of tissue-specific pathology and gene expression of human disease genes and complexes *Proc. Natl Acad. Sci. USA* **105** 20870–5
- [19] Lage K et al 2010 Dissecting spatio-temporal protein networks driving human heart development and related disorders *Mol. Syst. Biol.* **6** 381
- [20] Kirouac D C, Ito C, Csaszar E, Roch A, Yu M, Sykes E A, Bader G D and Zandstra P W 2010 Dynamic interaction networks in a hierarchically organized tissue *Mol. Syst. Biol.* **6** 417
- [21] Park J, Lee D-S, Christakis N A and Barabási A-L 2009 The impact of cellular networks on disease comorbidity *Mol. Syst. Biol.* **5** 262
- [22] Lee D-S, Park J, Kay K A, Christakis N A, Oltvai Z N and Barabási A-L 2008 The implications of human metabolic network topology for disease comorbidity *Proc. Natl Acad. Sci. USA* **105** 9880–5
- [23] Goh K-I, Cusick M E, Valle D, Childs B, Vidal M and Barabási A-L 2007 The human disease network *Proc. Natl Acad. Sci. USA* **104** 8685–90
- [24] Schadt E E 2009 Molecular networks as sensors and drivers of common human diseases *Nature* **461** 218–23

- [25] Joyner M J 2011 Physiology: alone at the bottom, alone at the top *J. Physiol.* **589** 1005
- [26] Tass P, Rosenblum M, Weule J, Kurths J, Pikovsky A, Volkmann J, Schnitzler A and Freund H 1998 Detection of n:m phase locking from noisy data: application to magnetoencephalography *Phys. Rev. Lett.* **81** 3291–4
- [27] Bullmore E and Sporns O 2009 Complex brain networks: graph theoretical analysis of structural and functional systems *Nat. Rev. Neurosci.* **10** 186–98
- [28] Liu K K L, Bartsch R P, Lin A, Mantegna R N and Ivanov P C 2015 Plasticity of brain wave network interactions and evolution across physiologic states *Front. Neural Circuits* **9** 62
- [29] Gallos L K, Makse H A and Sigman M 2012 A small world of weak ties provides optimal global integration of self-similar modules in functional brain networks *Proc. Natl Acad. Sci. USA* **109** 2825–30
- [30] Bashan A, Bartsch R P, Kantelhardt J W, Havlin S and Ivanov P C 2012 Network physiology reveals relations between network topology and physiological function *Nat. Commun.* **3** 702
- [31] Ivanov P C and Bartsch R P 2014 Network physiology: mapping interactions between networks of physiologic networks *Networks of Networks: The Last Frontier of Complexity* (Berlin: Springer) pp 203–22
- [32] Buchman T G 2006 Physiologic failure: multiple organ dysfunction syndrome *Complex Systems Science in BioMedicine* (New York: Kluwer/Plenum) pp 631–40
- [33] Moorman J R, Lake D E and Ivanov P C 2016 Early detection of sepsis role for network physiology? *Crit. Care Med.* **44** e312–3
- [34] Bartsch R P, Liu K K L, Bashan A and Ivanov P C 2015 Network physiology: how organ systems dynamically interact *PLoS One* **10** e0142143
- [35] Valenza G, Toschi N and Barbieri R 2016 Uncovering brain–heart information through advanced signal and image processing *Phil. Trans. R. Soc. A* **374** 20160020
- [36] Liu K K L, Bartsch R P, Ma Q D Y and Ivanov P C 2015 Major component analysis of dynamic networks of physiologic organ interactions *J. Phys. Conf. Ser.* **640** 012013
- [37] Loscalzo J and Barabasi A-L 2011 Systems biology and the future of medicine *Wiley Interdiscip. Rev. Syst. Biol. Med.* **3** 619–27
- [38] Hopkins A L 2008 Network pharmacology: the next paradigm in drug discovery *Nat. Chem. Biol.* **4** 682–90
- [39] Millman D, Mihalas S, Kirkwood A and Niebur E 2010 Self-organized criticality occurs in non-conservative neuronal networks during ‘up’ states *Nat. Phys.* **6** 801–5
- [40] de Arcangelis L, Perrone-Capano C and Herrmann H J 2006 Self-organized criticality model for brain plasticity *Phys. Rev. Lett.* **96** 028107
- [41] Zhang X, Boccaletti S, Guan S and Liu Z 2015 Explosive synchronization in adaptive and multilayer networks *Phys. Rev. Lett.* **114** 038701
- [42] Komarov M and Pikovsky A 2013 Dynamics of multifrequency oscillator communities *Phys. Rev. Lett.* **110** 134101
- [43] Pecora L M, Sorrentino F, Hagerstrom A M, Murphy T E and Roy R 2014 Cluster synchronization and isolated desynchronization in complex networks with symmetries *Nat. Commun.* **5** 4079
- [44] Gomez-Gardenes J, Gomez S, Arenas A and Moreno Y 2011 Explosive synchronization transitions in scale-free networks *Phys. Rev. Lett.* **106** 128701
- [45] Boulos R E et al 2014 From the chromatin interaction network to the organization of the human genome into replication n/u-domains *New J. Phys.* **16** 115014
- [46] De Martino D, Capuani F and De Martino A 2014 Inferring metabolic phenotypes from the exometabolome through a thermodynamic variational principle *New J. Phys.* **16** 115018
- [47] Lin G-Q, Ao B, Chen J-W, Wang W-X and Di Z-R 2014 Modeling and controlling the two-phase dynamics of the p53 network: a boolean network approach *New J. Phys.* **16** 125010
- [48] Jolly M K, Boaretto M, Lu M, Jose N O, Clementi C and Ben-Jacob E 2015 Operating principles of notch-delta-jagged module of cell–cell communication *New J. Phys.* **17** 055021
- [49] Oliveira C L, Bates J H and Suki B 2014 A network model of correlated growth of tissue stiffening in pulmonary fibrosis *New J. Phys.* **16** 065022
- [50] Klimm F, Borge-Holthoefer J, Wessel N, Kurths J and Zamora-López G 2014 Individual node’s contribution to the mesoscale of complex networks *New J. Phys.* **16** 125006
- [51] Wang R-S, Oldham W M and Loscalzo J 2014 Network-based association of hypoxia-responsive genes with cardiovascular diseases *New J. Phys.* **16** 105014
- [52] Sun P G 2015 Co-controllability of drug–disease–gene network *New J. Phys.* **17** 085009
- [53] Holme P and Saramäki J 2012 Temporal networks *Phys. Rep.* **519** 97–125
- [54] Rothkegel A and Lehnertz K 2014 Irregular macroscopic dynamics due to chimera states in small-world networks of pulse-coupled oscillators *New J. Phys.* **16** 055006
- [55] Stramaglia S, Cortes J M and Marinazzo D 2014 Synergy and redundancy in the Granger causal analysis of dynamical networks *New J. Phys.* **16** 105003
- [56] Traxl D, Boers N and Kurths J 2014 General scaling of maximum degree of synchronization in noisy complex networks *New J. Phys.* **16** 115009
- [57] Mafahim J U, Lambert D, Zare M and Grigolini P 2015 Complexity matching in neural networks *New J. Phys.* **17** 015003
- [58] Stankovski T, Ticcini V, McClintock P V E and Stefanovska A 2015 Coupling functions in networks of oscillators *New J. Phys.* **17** 035002
- [59] West B J, Turalska M and Grigolini P 2015 Fractional calculus ties the microscopic and macroscopic scales of complex network dynamics *New J. Phys.* **17** 045009
- [60] Muller L, Destexhe A and Rudolph-Lilith M 2014 Brain networks: small-worlds, after all? *New J. Phys.* **16** 105004
- [61] Huang X, Zheng Z, Hu G, Wu S and Rasch M J 2015 Different propagation speeds of recalled sequences in plastic spiking neural networks *New J. Phys.* **17** 035006
- [62] Goychuk I and Goychuk A 2015 Stochastic Wilson–Cowan models of neuronal network dynamics with memory and delay *New J. Phys.* **17** 045029
- [63] Lo C-C, Amaral L A N, Havlin S, Ivanov P C, Penzel T, Peter J-H and Stanley H E 2002 Dynamics of sleep–wake transitions during sleep *Europhys. Lett.* **57** 625–31
- [64] Lo C-C, Chou T, Penzel T, Scammell T E, Strecker R E, Stanley H E and Ivanov P C 2004 Common scale-invariant patterns of sleep–wake transitions across mammalian species *Proc. Natl Acad. Sci. USA* **101** 17545–8
- [65] Blumberg M S, Seelke A M H, Lowen S B and Karlsson K A 2005 Dynamics of sleep–wake cyclicality in developing rats *Proc. Natl Acad. Sci. USA* **102** 14860–4

- [66] Lo C-C, Bartsch R P and Ivanov P C 2013 Asymmetry and basic pathways in sleep-stage transitions *Europhys. Lett.* **102** 10008
- [67] Beggs J M and Plenz D 2003 Neuronal avalanches in neocortical circuits *J. Neurosci.* **23** 11167–77
- [68] Beggs J M and Plenz D 2004 Neuronal avalanches are diverse and precise activity patterns that are stable for many hours in cortical slice cultures *J. Neurosci.* **24** 5216–29
- [69] Levina A, Herrmann J M and Geisel T 2007 Dynamical synapses causing self-organized criticality in neural networks *Nat. Phys.* **3** 857–60
- [70] Mosqueiro T, de Lecea L and Huerta R 2014 Control of sleep-to-wake transitions via fast amino acid and slow neuropeptide transmission *New J. Phys.* **16** 115010
- [71] Kraleman B, Pikovsky A and Rosenblum M 2014 Reconstructing effective phase connectivity of oscillator networks from observations *New J. Phys.* **16** 085013
- [72] Faes L, Nollo G, Jurysta F and Marinazzo D 2014 Information dynamics of brain–heart physiological networks during sleep *New J. Phys.* **16** 105005
- [73] Piper D, Schiecke K, Pester B, Benninger F, Feucht M and Witte H 2014 Time-variant coherence between heart rate variability and EEG activity in epileptic patients: an advanced coupling analysis between physiological networks *New J. Phys.* **16** 115012
- [74] Ferrari F A S, Viana R L, Gomez F, Lorimer T and Stoop R 2015 Macroscopic bursting in physiological networks: node or network property? *New J. Phys.* **17** 055024
- [75] Chmiel A, Klimek P and Thurner S 2014 Spreading of diseases through comorbidity networks across life and gender *New J. Phys.* **16** 115013
- [76] Scala A, Auconi P and Scazzocchio M 2014 Complex networks for data-driven medicine: the case of Class III dentoskeletal disharmony *New J. Phys.* **16** 115017
- [77] Arodz T and Bonchev D 2015 Identifying influential nodes in a wound healing-related network of biological processes using mean first-passage time *New J. Phys.* **17** 025002
- [78] Fernandes H M, Van Hartevelt T J, Boccard S G, Owen S L, Cabral J, Deco G, Green A L, Fitzgerald J J, Aziz T Z and Kringelbach M L 2015 Novel fingerprinting method characterises the necessary and sufficient structural connectivity from deep brain stimulation electrodes for a successful outcome *New J. Phys.* **17** 015001
- [79] Przytycka T M, Singh M and Slonim D K 2010 Toward the dynamic interactome: it’s about time *Briefings Bioinform.* **11** 15–29

[Free Full Text from Publisher](#)

Save to EndNote online

[Add to Marked List](#)

122 of 127

Focus on the emerging new fields of network physiology and network medicine

By: **Ivanov, PC** (Ivanov, Plamen Ch)^[1,2,3,4]; **Liu, K** (Liu, Kang K. L.)^[1,2,5]; **Bartsch, RP** (Bartsch, Ronny P.)^[6]

[View ResearcherID and ORCID](#)

NEW JOURNAL OF PHYSICS

Volume: 18

Article Number: 100201

DOI: 10.1088/1367-2630/18/10/100201

Published: OCT 13 2016

Document Type: Editorial Material

[View Journal Impact](#)

Abstract

Despite the vast progress and achievements in systems biology and integrative physiology in the last decades, there is still a significant gap in understanding the mechanisms through which (i) genomic, proteomic and metabolic factors and signaling pathways impact vertical processes across cells, tissues and organs leading to the expression of different disease phenotypes and influence the functional and clinical associations between diseases, and (ii) how diverse physiological systems and organs coordinate their functions over a broad range of space and time scales and horizontally integrate to generate distinct physiologic states at the organism level. Two emerging fields, network medicine and network physiology, aim to address these fundamental questions. Novel concepts and approaches derived from recent advances in network theory, coupled dynamical systems, statistical and computational physics show promise to provide new insights into the complexity of physiological structure and function in health and disease, bridging the genetic and sub-cellular level with intercellular interactions and communications among integrated organ systems and sub-systems. These advances form first building blocks in the methodological formalism and theoretical framework necessary to address fundamental problems and challenges in physiology and medicine. This 'focus on' issue contains 26 articles representing state-of-the-art contributions covering diverse systems from the sub-cellular to the organism level where physicists have key role in laying the foundations of these new fields.

Keywords

KeyWords Plus: SELF-ORGANIZED CRITICALITY; SLEEP-WAKE TRANSITIONS; COMPLEX NETWORKS; HUMAN-DISEASE; NEURONAL AVALANCHES; BRAIN NETWORKS; GENES; TISSUE; INTERACTOME; COMORBIDITY

Author Information

Reprint Address: Ivanov, PC (reprint author)

+ Boston Univ, Dept Phys, Keck Lab Network Physiol, 590 Commonwealth Ave, Boston, MA 02215 USA.

Reprint Address: Ivanov, PC (reprint author)

+ Harvard Med Sch, Boston, MA 02115 USA.

Reprint Address: Ivanov, PC (reprint author)

+ Brigham & Womens Hosp, Div Sleep Med, Boston, MA 02115 USA.

Citation Network

In Web of Science Core Collection

15

Times Cited

[Create Citation Alert](#)

All Times Cited Counts

15 in All Databases

[See more counts](#)**77**

Cited References

[View Related Records](#)

Most recently cited by:

Li, Xinwei; Li, Qionglin; Wang, Xuetong; et al.
[Differential Age-Related Changes in Structural Covariance Networks of Human Anterior and Posterior Hippocampus.](#)
FRONTIERS IN PHYSIOLOGY (2018)

Topcu, Cagdas; Fruehwirth, Matthias; Moser, Maximilian; et al.
[Disentangling respiratory sinus arrhythmia in heart rate variability records.](#)
PHYSIOLOGICAL MEASUREMENT (2018)

[View All](#)

Use in Web of Science

Web of Science Usage Count

0**13**

Last 180 Days

Since 2013

[Learn more](#)

This record is from:
Web of Science Core Collection

[Suggest a correction](#)

Reprint Address: Ivanov, PC (reprint author)

+ Bulgarian Acad Sci, Inst Solid State Phys, BU-1784 Sofia, Bulgaria.

Addresses:

+ [1] Boston Univ, Dept Phys, Keck Lab Network Physiol, 590 Commonwealth Ave, Boston, MA 02215 USA

+ [2] Harvard Med Sch, Boston, MA 02115 USA

+ [3] Brigham & Womens Hosp, Div Sleep Med, Boston, MA 02115 USA

+ [4] Bulgarian Acad Sci, Inst Solid State Phys, BU-1784 Sofia, Bulgaria

+ [5] Beth Israel Deaconess Med Ctr, Dept Neurol, Boston, MA 02215 USA

+ [6] Bar Ilan Univ, Dept Phys, IL-5290002 Ramat Gan, Israel

E-mail Addresses: plamen@buphy.bu.edu

Publisher

IOP PUBLISHING LTD, TEMPLE CIRCUS, TEMPLE WAY, BRISTOL BS1 6BE, ENGLAND

Journal Information

Impact Factor: [Journal Citation Reports](#)

Categories / Classification

Research Areas: Physics

Web of Science Categories: Physics, Multidisciplinary

[See more data fields](#)

◀ 122 of 127 ▶

Cited References: 77

Showing 30 of 77 [View All in Cited References page](#)

(from Web of Science Core Collection)

1. **Statistical mechanics of complex networks** **Times Cited: 10,700**
By: Albert, R; Barabasi, AL
REVIEWS OF MODERN PHYSICS Volume: 74 Issue: 1 Pages: 47-97 Published: JAN 2002
2. **McKusick's Online Mendelian Inheritance in Man (OMIM (R))** **Times Cited: 394**
By: Amberger, Joanna; Bocchini, Carol A.; Scott, Alan F.; et al.
NUCLEIC ACIDS RESEARCH Volume: 37 Pages: D793-D796 Published: JAN 2009
3. **Identifying influential nodes in a wound healing-related network of biological processes using mean first-passage time** **Times Cited: 4**
By: Arodz, Tomasz; Bonchev, Danail
NEW JOURNAL OF PHYSICS Volume: 17 Article Number: 025002 Published: FEB 4 2015
4. **Network medicine: a network-based approach to human disease** **Times Cited: 1,499**
By: Barabasi, Albert-Laszlo; Gulbahce, Natali; Loscalzo, Joseph
NATURE REVIEWS GENETICS Volume: 12 Issue: 1 Pages: 56-68 Published: JAN 2011
5. **Network medicine - From obesity to the "Diseasome"** **Times Cited: 269**
By: Barabasi, Albert-Laszlo
NEW ENGLAND JOURNAL OF MEDICINE Volume: 357 Issue: 4 Pages: 404-407 Published: JUL 26 2007

Entropy measures, entropy estimators, and their performance in quantifying complex dynamics: Effects of artifacts, nonstationarity, and long-range correlations

Wanting Xiong,^{1,2} Luca Faes,³ and Plamen Ch. Ivanov^{2,4,5,*}¹*School of Systems Science, Beijing Normal University, Beijing 100875, People's Republic of China*²*Keck Laboratory for Network Physiology, Department of Physics, Boston University, Boston, Massachusetts 02215, USA*³*Bruno Kessler Foundation and BIOTech, University of Trento, Trento 38123, Italy*⁴*Harvard Medical School and Division of Sleep Medicine, Brigham and Women's Hospital, Boston, Massachusetts 02115, USA*⁵*Institute of Solid State Physics, Bulgarian Academy of Sciences, Sofia 1784, Bulgaria*

(Received 25 January 2017; revised manuscript received 27 April 2017; published 12 June 2017)

Entropy measures are widely applied to quantify the complexity of dynamical systems in diverse fields. However, the practical application of entropy methods is challenging, due to the variety of entropy measures and estimators and the complexity of real-world time series, including nonstationarities and long-range correlations (LRC). We conduct a systematic study on the performance, bias, and limitations of three basic measures (entropy, conditional entropy, information storage) and three traditionally used estimators (linear, kernel, nearest neighbor). We investigate the dependence of entropy measures on estimator- and process-specific parameters, and we show the effects of three types of nonstationarities due to artifacts (trends, spikes, local variance change) in simulations of stochastic autoregressive processes. We also analyze the impact of LRC on the theoretical and estimated values of entropy measures. Finally, we apply entropy methods on heart rate variability data from subjects in different physiological states and clinical conditions. We find that entropy measures can only differentiate changes of specific types in cardiac dynamics and that appropriate preprocessing is vital for correct estimation and interpretation. Demonstrating the limitations of entropy methods and shedding light on how to mitigate bias and provide correct interpretations of results, this work can serve as a comprehensive reference for the application of entropy methods and the evaluation of existing studies.

DOI: [10.1103/PhysRevE.95.062114](https://doi.org/10.1103/PhysRevE.95.062114)

I. INTRODUCTION

The growing awareness that many real-world systems exhibit complex dynamics that are challenging to quantify has initiated extensive interest in developing measures and approaches for time series analysis to characterize these systems. In this context, the utilization of tools taken from information theory has become extremely popular for the assessment of the degree of complexity of physical, biological, physiological, social, and econometric systems. A variety of measures rooted in the concept of entropy and implemented according to several estimation approaches have been proposed, including approximate entropy [1], sample entropy [2], corrected conditional entropy [3], fuzzy entropy [4], compression entropy [5], permutation entropy [6,7], distribution entropy [8], multiscale entropy [9–12], self entropy and information storage [13,14]. These measures have emerged as a less ambitious but more practical alternative to classical techniques for the analysis of nonlinear dynamical systems, like correlation dimension [15], Lyapunov exponents [16], and nonlinear prediction methods [17,18]. In fact, the popularity of entropy measures stems from their applicability to short and noisy processes with important stochastic components such as those describing the dynamical activity of real-world systems. These measures have been applied with great success to numerous research fields, including heart rate variability [3,19–23], cardiovascular control [3,24–26], cerebrovascular dynamics [27,28], cardiac arrhythmias [29], financial time series analysis [30,31], gait and posture [32–36], climatology [37], earth sciences

[38], cellular automata [39,40], electromyography [41], electroencephalography [42–44], magnetoencephalography [45], functional neuroimaging [14,46,47], and others [48–51].

Despite the broad relevance and application of entropy measures for various systems and fields of science, a number of theoretical, computational, and practical issues exist that often prevent a fair evaluation of the performance of these measures, as well as a correct interpretation of the measured complexity of the observed dynamics.

First, since there are many entropy measures with a variety of entropy estimators that are not always independent of each other, it is not straightforward to associate a given measure to the complexity of the dynamical system under analysis and to compare the variety of entropy measures obtained by different estimators. In addition, the crucial but often elusive term of “complexity” is also related to several other concepts in physics and biology, such as the existence of long-range correlations [52–56], nonlinear multifractal properties [57–61], and/or chaotic dynamics [15,16], which are not univocally linked to the signal features reflected by entropy measures [62]; even within the family of entropy measures, different working definitions of complexity have been proposed, e.g., in terms of “randomness” [63], “unpredictability” [3], or “regularity” [64].

Second, given that the practical computation of information-theoretic measures from real-world time series is not a trivial task, several approaches exist for the estimation of these measures [65]. Entropy estimators differ in the assumptions made about the properties of the investigated process and follow different approaches to approximate the probability density function utilized in the computation of entropy measures. Thus, entropy estimates are often highly

*plamen@buphy.bu.edu

dependent on method-specific parameters. In the absence of a comparative evaluation of the different estimators, assessing their performances and interpreting results obtained using different estimation strategies has become a subjective task. Furthermore, an incorrect or unaware setting of the estimation parameters may easily lead to wrong inference about the properties of the observed dynamics.

Third, even though stationarity of time series is a prerequisite for the estimation of entropy measures for the target dynamical system, entropy estimators are often blindly applied without checking the fulfillment of this prerequisite. The presence of nonstationarity is often due to artifacts of various nature and exists in diversified forms such as trends, spikes, and changes in local variance. Due to the differences in entropy measures and estimators, the effects of nonstationarity vary for different entropy measures and for different estimation approaches. Therefore, a comprehensive investigation of the limitations and biases of entropy-based methods in the presence of nonstationarity is not only vital for reducing the biases in the estimation of entropy measures, but also important for the evaluation and comparison of results from different studies.

Fourth, an unaddressed issue with the computation of entropy measures is the effect of long-range correlations. It is well known that a broad class of dynamic processes in physics, biology, and econometrics exhibit long-range power-law correlations that result in scaling properties observed across multiple temporal scales [53,55,57,58,66–74]. Despite the fact that these intrinsic properties of dynamic processes are manifested even at the shorter scales and within the shorter time windows typically used in the assessment of information theoretic measures, their effects on the estimated values of entropy measures are not comprehensively investigated and not taken into account in the majority of empirical studies.

Due to the theoretical and practical issues related to the variety of entropy measures, entropy estimators, and the complexity of real-world time series mentioned above, it is therefore difficult to compare and evaluate the results from existing literature, which are often not consistent or even contradicting because different studies are based on data with different types of nonstationarity and long-range correlations, and researchers adopt different entropy measures and estimators as well as different data preprocessing and filtering procedures, which affect the outcome of information theoretic analyses.

To address the problems and challenges mentioned above, here we present a systematic study on the performance of entropy measures and estimators in various situations with both simulated and empirical time series. We aim to answer three questions: (1) to what extent entropy measures adequately characterize the dynamics of complex systems; (2) what are the limitations and biases of entropy estimators in approximating entropy measures from time series with various types of nonstationarity and presence of long-range correlations; (3) how to perform credible estimations and provide appropriate interpretations.

We present a unifying framework for the definition of entropy measures and corresponding estimation methods from time series data, which serves to clarify their theoretical meanings and assess their practical significance in the evaluation of

the complexity of dynamic processes measured from physical systems. We show that a range of information theoretic measures can be subsumed by the three basic measures of entropy, conditional entropy, and information storage, and three of most widely used approaches for the quantification of these measures—linear estimator, kernel estimator, and nearest-neighbor estimator.

Further, we provide a detailed systematic analysis of the most basic frequently encountered dynamic processes and perform a comparative assessment of entropy measures and entropy estimators on multiple realizations of these processes. We study the dependence of entropy measures on estimator-specific parameters, as well as the effects of three types of nonstationarities due to artifacts that are commonly encountered in real data (i.e., slow trends, random spikes, and local variance changes). Importantly, we present for the first time a systematic quantitative assessment of the impact on entropy measures of trends originating from the intrinsic dynamics of systems exhibiting multifractal scaling properties, both in the case of long-range power-law correlations and in the more complicated and realistic situation in which long-range correlations and short-term autoregression coexist.

Finally, we consider a practical case of study that subsumes all the issues treated in the simulations, i.e., the study of human heartbeat fluctuations in different physiological states (wake and sleep) and pathological conditions (healthy and congestive heart failure). These analyses evidence advantages and pitfalls of entropy measures and estimators, as well as provide indications for their optimal use in the study of real-world time series, including recommendations about which measure to adopt depending on the purpose of the analysis, which estimator to implement in different conditions, how to deal with nonstationarities and artifacts, and how to interpret the values obtained from complex systems with different coexisting types of dynamics.

II. METHODS

A. Entropy measures

In the analysis of dynamical systems, entropy measures are used to characterize the temporal statistical structure of a system evolving in time. In an information-theoretic framework, the “information” contained in a dynamical system varies at each time step. When the system transits from past states to a new state, new information is produced in addition to the information that is already carried by the past states. This process is reflected by entropy measures: the entropy quantifies the information carried by the present state of the system, the conditional entropy quantifies the new information contained in the present but not in the past, and the information storage quantifies the amount of information carried by the present that can be explained by the past history of the system.

To introduce the notation, we consider a dynamical system \mathcal{X} and assume that the states visited by this system are described by the stochastic process X . Let us further denote X_n as the random variable obtained by sampling the process X at the present time n , and $X_n^- = [X_1, \dots, X_{n-2}, X_{n-1}]$ as the vector variable describing the past of X . The probability distribution for an individual variable $X_i, i =$

$1, \dots, n$, is $p(x_i) = \Pr\{X_i = x_i, x_i \in \mathcal{A}_i\}$, where \mathcal{A}_i is the set of all possible values that may be taken by X_i . Then, the process X is fully characterized by the joint probability distributions $p(x_1, \dots, x_n) = \Pr\{X_1 = x_1, \dots, X_n = x_n\}, \forall n \geq 1$, with $(x_1, \dots, x_n) \in \mathcal{A}_1 \times \dots \times \mathcal{A}_n$. An important property of dynamic processes is stationarity, which defines the time-invariance of the joint probabilities extracted from the process: $\Pr\{X_1 = x_1, \dots, X_n = x_n\} = \Pr\{X_{1+m} = x_1, \dots, X_{n+m} = x_n\} = p(x_1, \dots, x_n), \forall n, m \geq 1$. Note that all random variables that can be obtained sampling a stationary process take values inside the same set, i.e., $\mathcal{A}_i = \mathcal{A} \forall i \geq 1$.

In the following, we provide definitions and illustrations of entropy, conditional entropy, and information storage computed for a stationary stochastic process. Note that the present study considers exclusively univariate stochastic processes describing the activity of individual dynamical systems; the reader is referred to the abundant literature in the field [13,75–78] for an extension to multivariate analysis.

1. Entropy

The central concept for the derivation of entropy measures is the definition of the *Shannon information content* of a random variable V [63]: the information contained in a specific outcome v of a random variable V is the quantity $h(v) = -\log p(v)$, where $p(v) = \Pr\{V = v\}$ is the probability that V takes the value v . The units of information depend on the base of the logarithm, being usually bits (base 2) for discrete random variables, and nats for continuous variables where the natural logarithm is used. According to this definition, the information content will be low for highly probable outcomes of the observed random variable and high for unlikely outcomes. Then, if the variable is continuous, the *differential entropy* expresses the amount of information carried by V intended as its average information content:

$$H(V) = - \int_{\mathcal{A}} p(v) \log p(v) dv, \quad (1)$$

where the integral is computed over a continuous range of values \mathcal{A} . When the probability $p(v)$ is discrete rather than continuous, the entropy of the variable is defined as

$$H(V) = - \sum_{v \in \mathcal{A}} p(v) \log p(v), \quad (2)$$

where \mathcal{A} is in this case the finite alphabet of values that can be taken by V . Using a notation that subsumes both Eqs. (1) and (2), entropy can be defined as the expected value of the Shannon information content:

$$H(V) = \mathbb{E}[h(v)] = -\mathbb{E}[\log p(v)], \quad (3)$$

where $\mathbb{E}[\cdot]$ is the expectation operator. Entropy quantifies information as the average uncertainty about the outcomes of the variable: if all observations of the variable take the same value, there is no uncertainty and the entropy is zero; if, on the contrary, the variable takes different values all with the same probability of occurrence, the entropy is maximum and reflects maximum uncertainty. The concept of entropy above defined relies on the seminal work of Shannon performed in the field of communication theory [63]. The relevant measure has been extended to the definition of many alternative measures of

information such as the Renyi entropy [79] and the Tsallis entropy [80], of which the Shannon entropy constitutes a limiting case that possesses all the desired properties of an information measure. Moreover, there are close parallels between these information-theoretic entropy measures and the fundamental thermodynamic entropy investigations of Boltzmann and Gibbs [81,82].

The entropies defined in Eqs. (1) and (2) are “static” measures, in the sense that they do not take any temporal information into account when describing an observed probability distribution. “dynamic” measures of entropy can be introduced by studying the information content of a stochastic process that represents the activity of a system evolving in time such as conditional entropy and information storage explained below. Specifically, the *entropy* of the process X is defined as the average information contained in its present state:

$$E(X) = H(X_n) = -\mathbb{E}[\log p(x_n)], \quad (4)$$

where x_n is the value taken by the process X at the present time n . Equation (4) presupposes stationarity of the process, so that it carries the same entropy at all times and dependence on time is dropped in the definition of $E(X)$. The past information contained in the system up to time $n - 1$ is defined as the joint entropy of the past variables X_n^- :

$$H(X_n^-) = H(X_1, \dots, X_{n-1}) = -\mathbb{E}[\log p(x_1, \dots, x_{n-1})]. \quad (5)$$

Likewise, the total information contained the the system up to time n is the joint entropy of the present and past variables, as given by

$$H(X_n^-, X_n) = H(X_1, \dots, X_n) = -\mathbb{E}[\log p(x_1, \dots, x_n)]. \quad (6)$$

The simple ideas of separating the present from the past and of incorporating the temporal information into the definition of entropy as done in Eqs. (4)–(6) form the basis of the studies of Kolmogorov [83] and Sinai [84], who first formalized information-theoretic concepts for the analysis of dynamical systems. As further studied by Ebeling [85] and discussed in the next subsections, dynamic entropies are closely related to the notion of predictability defined for a dynamical system evolving in time.

2. Conditional entropy

In general, the present state of the observed process is partially determined by its past history, but also carries a certain amount of new information that cannot be inferred from the past. The average rate of creation of new information is given by the *conditional entropy*, also known as the Kolmogorov-Sinai entropy [86]:

$$\begin{aligned} C(X) &= H(X_n | X_n^-) = H(X_n^-, X_n) - H(X_n^-) \\ &= -\mathbb{E}[\log p(x_n | x_1, \dots, x_{n-1})], \end{aligned} \quad (7)$$

where $p(x_n | x_1, \dots, x_{n-1})$ is the conditional probability that X takes the value x_n at time n given that the values taken previously were x_1, \dots, x_{n-1} .

Thus, the conditional entropy quantifies the amount of information contained in the present of the process that cannot be explained by its past history: if the process is fully

random, the system produces information at the maximum rate, yielding maximum conditional entropy; if, on the contrary, the process is fully predictable, the system does not produce new information and the conditional entropy is zero. When the process is stationary, the system produces new information at a constant rate; i.e., the conditional entropy does not change over time.

The notion of conditional entropy subsumes a wide range of entropy measures and estimates that have been proposed in the recent past to quantify the complexity of a time series intended as the degree of predictability of the underlying process. These measures, which include approximate entropy [1], sample entropy [2], fuzzy entropy [4], corrected conditional entropy [3], and permutation entropy [6], are extremely popular for the estimation of conditional entropy in several fields ranging from applied physics to neuroscience, physiology, econometrics, climatology, earth sciences, and others [24,25,29–32,37,38,87,88].

3. Information storage

Another relevant entropy measure is the so-called information storage, which quantifies the amount of information shared between the present and the past observations of the considered stochastic process. For a generic process X , the information storage is defined as

$$S(X) = I(X_n; X_n^-) = \mathbb{E} \left[\log \frac{p(x_1, \dots, x_n)}{p(x_1, \dots, x_{n-1})p(x_n)} \right], \quad (8)$$

where $I(X_n; X_n^-)$ denotes the mutual information between X_n and X_n^- .

The information storage reflects the degree to which information is preserved in a time-evolving system [14]. As such, it measures how much of the uncertainty about the present can be resolved by knowing the past: if the process is fully random, the past gives no knowledge about the present, so that the information storage is zero; if, on the contrary, the process is fully predictable, the present can be fully predicted from the past, which results in maximum information storage. If the process X is stationary, the information shared between the present and the past is constant.

Although information storage has been long recognized as an important aspect of the dynamics of many physical and biological processes, it has been formalized only recently as in Eq. (8) as the information contained in the past of a process that can be used to predict its future [39]. This quantitative definition is gaining more and more relevance and has been used with great success to analyze complex dynamics in physiology [26,27,89], neuroscience [90,91], collective behaviors [92], and artificial systems [40,93].

To summarize, the entropy of a dynamical system measures the information contained in its present state. The information of the present state can then be decomposed into two parts: the new information that cannot be inferred from the past, which is measured by the conditional entropy and the information that can be explained by its past, which is measured by the information storage. Consequently, entropy, conditional entropy, and information storage are related to each other by the equation $S(X) = E(X) - C(X)$.

4. Illustrative example

In this section we demonstrate the properties of the entropy measures defined above using an exemplary stationary binary Markov process of order one as depicted in Fig. 1. The binary process takes values in the alphabet $\mathcal{A} = \{0, 1\}$ and is defined in a way such that the two outcomes are equiprobable; i.e., $p(X_n = 0) = p(X_n = 1) = 0.5$. Moreover, according to the Markov property, the present state of the process depends on the past at only one time lag: $p(x_n | x_1, \dots, x_{n-1}) = p(x_n | x_{n-1})$. We further assume that the conditional probability for the process to take the same value at times $n - 1$ and n , $\Pr\{X_n = x | X_{n-1} = x\}$, is inversely modulated by a parameter $\delta \in [0, 1]$ in a way such that δ quantifies the strength of the internal dynamics in the system: the higher δ is, the more the present state is dependent on the past states [Fig. 1(a)].

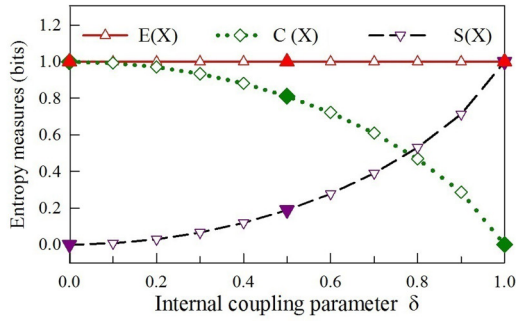
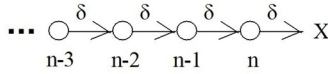
The exact theoretical values of entropy, conditional entropy and information storage computed as a function of δ are reported in the bottom panel of Fig. 1(a), while the remaining panels depict exemplary realizations of the process and values of the entropy measures for the cases of fully random dynamics [$\delta = 0$, Fig. 1(b)], fully predictable dynamics [$\delta = 1$, Fig. 1(c)] and partially predictable dynamics [$\delta = 0.5$, Fig. 1(d)]. As seen in Fig. 1(a), the entropy of the process is constant and equal to 1 bit, because it only depends on the marginal probabilities, which do not change with δ ($p(X_n = 0) = p(X_n = 1) = 0.5$). When δ moves from 0 to 1, the conditional entropy decreases and the information storage increases, reflecting the increasing predictability of the process. The entropy measures the present information contained the dynamic system, $H(X_n) = E(X)$, represented by the solid line with triangle or the red oval. The conditional entropy measures the rate of increase of the total information of the system, which is represented by the slope of the solid line with squares or the part of the red oval not overlapped with the blue. The information storage measures the shared amount of the present information $H(X_n)$ and the past information $H(X_n^-)$, which is represented by the overlap of the red and blue ovals. The fully random dynamical system described in Fig. 1(b) produces new information at the maximum rate, yielding $C(X) = E(X)$ and $S(X) = 0$ (no overlap of the red and blue ovals). The fully predictable system in Fig. 1(c) produces no new information at any time, yielding $C(X) = 0$ and $S(X) = E(X)$ (superimposition of the red and blue ovals). The partially predictable system in Fig. 1(d) produces new information but also maintains past information, yielding $C(X) \in (0, E(X))$ and $S(X) \in (0, E(X))$ (partial overlap of the red and blue ovals).

B. Entropy estimators

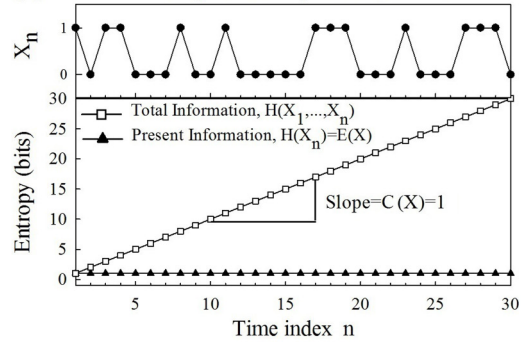
In practical analysis, entropy measures are computed from realizations of the observed process that are available in the form of time series data. In general, the estimation of information-theoretic measures from time series is a difficult task. A major issue is the so-called ‘‘curse of dimensionality’’ [94], which refers to the fact that numerical computation is possible only for entropies of finite order. Specifically, when the dimension of the observed variables increases, the conditional entropy estimated from time series of finite length decays towards zero [3]. Therefore, in the practice of short time

(a) Stationary binary order-1 Markov process

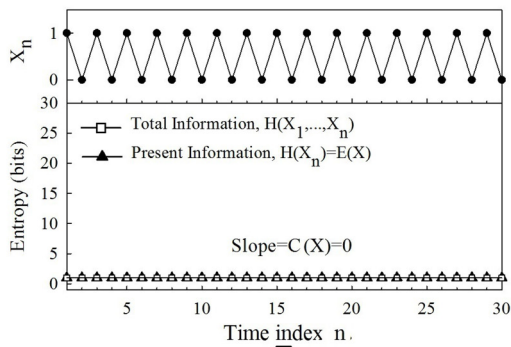
$$p(X_n = x | X_{n-1} = x) = \frac{1 - \delta}{2}, \text{ where } \delta \in [0, 1]$$



(b) Fully random process ($\delta = 0$)



(c) Fully predictable process ($\delta = 1$)



(d) Partially predictable process ($\delta = 0.5$)

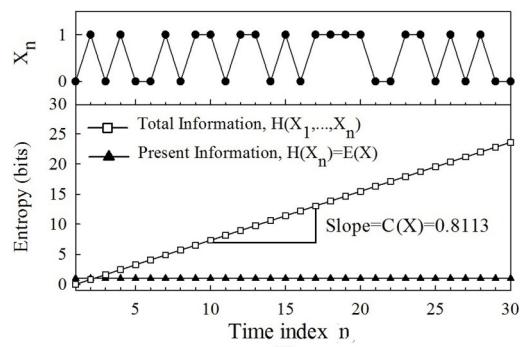


FIG. 1. Computation of entropy measures for a stationary binary order-1 Markov process. Since this process takes discrete values, entropies are computed using the base 2 logarithm and measured in bits. (a) Dependence of the transition probabilities and the entropy measures on the internal coupling parameter δ . When δ rises from 0 to 1, the probability that a state transition keeps the process in the same state ($p(X_n = x | X_{n-1} = x)$) moves from 1/2 to 0; accordingly, conditional entropy decreases from 1 to 0 (green dotted line with diamond) and information storage increases from 0 to 1 (purple dashed line with down-triangle); note that, since for this process the marginal probabilities are unaffected by δ , the entropy of the process does not change (red solid line with up-triangle). The values of entropy measures for $\delta = 0, 0.5, 1$ are marked with full symbols. (b), (c), (d) Entropy analysis for representative parameter values, showing a realization of the process (solid line with full circles), the total and present system information as a function of time, and the Venn diagram of the entropy measures (present information, red oval; past information, blue oval). For this stationary process, the present information is the same at all times and measures the entropy of the process (E), while the total information increases at a constant rate measured by the conditional entropy (C); the information storage (S) is the information shared between the present and the past (overlap of ovals), while the C is the part of the present information not shared with the past. When the process is fully random ($\delta = 0$), the total information increases at the maximum rate ($C = 1$) and there is no stored information ($S = 0$). On the contrary, a fully predictable process ($\delta = 1$) does not produce new information ($C = 0$) and stores the whole information contained in its present state ($S = 1$). Any intermediate parameter configuration ($0 < \delta < 1$) yields a partially predictable process with presence of both information production and information storage ($0 < S < 1, 0 < C < 1$).

series analysis, conditional entropy and information storage are estimated using a finite number of samples in the past, i.e., X_n^- is approximated by $X_n^m = [X_{n-1}, X_{n-2}, \dots, X_{n-m}]$ when computing $H(X_n | X_n^-)$ and $I(X_n; X_n^-)$. While optimization

techniques such as graphical models [94] or nonuniform embedding [89,95] exist to limit the detrimental effects of the curse of dimensionality, yet in this study we stick to the uniform embedding scheme, which selects m consecutive

past samples, so as to compare the performances of different estimators under the “standard” conditions that are commonly studied in the existing literature.

Various entropy estimators that follow different approaches to compute the probability distribution are available in the literature [75]. The estimators can be categorized into two groups: model-based estimators and model-free estimators. If the probability distribution of the data can be faithfully represented by a known parametric distribution (e.g., Gaussian), entropy measures can be computed using model-based estimators as functions of the parameters of the presumed probability distribution [13,75,96]. On the other hand, when no assumptions can be made about the data distribution, model-free approaches which approximate the probability distribution directly from the data should be followed. The most intuitive method is to build the histogram distribution of the quantized time series amplitudes. However, this method is proved to have serious bias problems and its estimates are strongly dependent on the size of the quantization levels [97,98]. This situation can be improved to some extent by using binless density estimators such as the kernels estimator [2,30,99] or the nearest neighbor estimator [100,101]. In this paper, we consider the linear model-based estimation method and the two model-free methods which employ kernel and nearest-neighbor entropy estimators. Details of these three estimators are presented in the following.

1. Linear estimator

The linear estimator is a model-based approach for the estimation of entropy measures. It adopts the assumption of a joint Gaussian distribution for the observed variables and exploits the exact expressions that hold in this case for the entropy measures. Specifically, the assumed Gaussian probability distribution is given by

$$p(x_n) = \frac{1}{\sqrt{2\pi\sigma_X^2}} e^{-\frac{x_n^2}{2\sigma_X^2}}, \quad (9)$$

where σ_X^2 is the variance of X_n . Then, by plugging Eq. (9) into Eq. (3), the entropy of the present state of the observed process is obtained as

$$E(X) = H(X_n) = \frac{1}{2} \ln 2\pi e\sigma_X^2. \quad (10)$$

Note that the entropy of a stationary Gaussian process is a function of its variance only.

Moreover, the linear method estimates the conditional entropy from the variance of the prediction error of the linear regression of the present of the process on its past [96]. Specifically, the linear regression of the present X_n on the past $X_{n-1}^m = [X_{n-1}, \dots, X_{n-m}]$ is performed as

$$X_n = \sum_{i=1}^m a_i X_{n-i} + U_n, \quad (11)$$

where m is the order of the regression, $a_i, i = 1, \dots, m$, are the regression coefficients, and U_n is a zero-mean white Gaussian noise. A paradigmatic example for the linear regression of X_n on X_{n-1} is given in Fig. 2. Then, the linear estimate of the conditional entropy is obtained from the variance of U_n , σ_U^2 ,

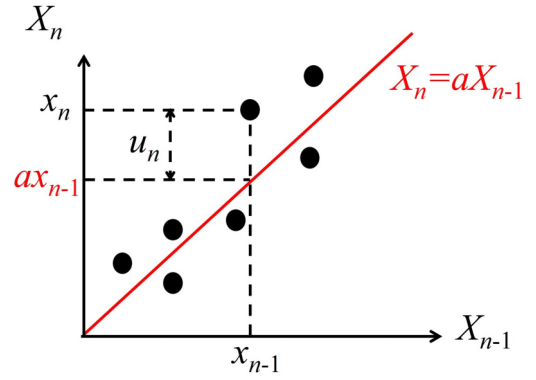


FIG. 2. Schematic illustration of the linear estimation of entropy measures. In this paradigmatic example in which a time series $\{x_1, \dots, x_8\}$ is considered as a realization of the process X , and the past of the process is approximated with $m = 1$ lags ($X_n^- \approx X_n^m = X_{n-1}$), seven realizations of (X_n, X_{n-1}) are found and used to fill a two-dimensional space. Then, the linear regression of X_n on X_{n-1} is performed yielding the regression line $X_n = aX_{n-1}$ (red line) and, for a given observation x_n of X_n , the prediction error u_n is taken as the difference between the true and the predicted value, $u_n = x_n - ax_{n-1}$. The estimates $\{u_2, \dots, u_8\}$ are finally used to compute the variance of U_n and the conditional entropy according to Eq. (12).

as follows:

$$C(X) = H(X_n|X_{n-1}^m) = \frac{1}{2} \ln 2\pi e\sigma_U^2. \quad (12)$$

Subtracting Eq. (12) from Eq. (10), the estimation of information storage is obtained as

$$S(X) = I(X_n; X_{n-1}^m) = \frac{1}{2} \ln \frac{\sigma_X^2}{\sigma_U^2}. \quad (13)$$

Hence, under the assumption of Gaussianity, the information storage is determined by the ratio of the variance of the present state of the process to the partial variance of the present given the past.

The formulations above exploit a central result relating the conditional entropy to the prediction error of a multivariate regression [96], which is here adapted to univariate regression and extended to the computation of information storage as proposed recently in both theoretical and empirical studies [13,25,25]. Note that, while the formulation presented here holds exactly only for Gaussian processes for which the linear representation captures the whole the entropy variations in the system, it may be extended in a straightforward way to nonlinear representations when non-Gaussian parametric distributions are assigned [75].

2. Kernel estimator

The Kernel entropy estimator is a model-free approach which reconstructs the probability distribution of an observed variable by centering kernel functions at each outcome of the variable and then exploits the estimated probabilities to derive the relevant entropy measures. Kernels are used to weight the distance of each point in the time series to the reference point depending on the kernel function. For instance, the entropy of the present state of the process X is estimated, starting from a realization of length N available in the form of the time

series $\{x_1, x_2, \dots, x_N\}$, first computing the kernel estimate of the probability distribution:

$$p(x_n) = \frac{1}{N} \sum_{i=1}^N K(\|x_n - x_i\|), \quad (14)$$

where K is the kernel function and $\|\cdot\|$ is an appropriate norm, and then plugging Eq. (14) into Eq. (4):

$$E(X) = H(X_n) = -\ln\langle p(x_n) \rangle, \quad (15)$$

where $\langle \cdot \rangle$ denotes the average taken over all possible x_n . Similarly, Eq. (14) can be used to estimate the joint probability distributions $p(x_n^m) = p(x_{n-1}, \dots, x_{n-m})$ and $p(x_n, x_n^m)$ in the m -dimensional and $(m+1)$ -dimensional spaces spanned by the realizations of X_n^m and (X_n, X_n^m) , from which the conditional entropy is obtained as

$$C(X) = H(X_n | X_n^m) = -\ln \frac{\langle p(x_n, x_n^m) \rangle}{\langle p(x_n^m) \rangle}. \quad (16)$$

Given the expressions of Eqs. (15) and (16) for the kernel estimates of entropy and conditional entropy, the kernel estimate of the information storage is then obtained as follows:

$$S(X) = I(X_n; X_n^m) = \ln \frac{\langle p(x_n, x_n^m) \rangle}{\langle p(x_n) p(x_n^m) \rangle}. \quad (17)$$

The most common metric to compute distances using the kernel estimator, which is adopted also in this study, is the so-called Chebyshev distance or maximum norm, which is obtained as the maximum of the absolute differences between scalar components, i.e., $\|x_n - x_i\| = |x_n - x_i|$ and $\|x_n^m - x_i^m\| = \max_{1 \leq k \leq m} |x_{n-k} - x_{i-k}|$. As to the kernel function, the most popular is the Heaviside kernel, which sets a threshold r to weight the distance of each point to the reference point. Its expression is

$$K = \Theta(\|x_n - x_i\|) = \begin{cases} 1, & \|x_n - x_i\| \leq r \\ 0, & \|x_n - x_i\| > r \end{cases}. \quad (18)$$

Substituting Eq. (18) into Eq. (14), one can see that the Heaviside Kernel estimator approximates the probability density at the reference point x_n with the fraction of time series points that falls within the distance r from x_n . The threshold r is the width of the Heaviside kernel function, which controls the precision of the density estimation: smaller values of r give more detailed estimates yet requiring more data points to be accurate, while too large values of r yield very coarse probability estimates because too many points are included in the neighborhood of the reference point. In practical computation, the threshold r is usually set to be a fraction of the data variance so as to remove the dependence of entropy measures on the amplitude of the observed process [1,2]. An illustrative example is depicted in Fig. 3 for the estimation of the probabilities $p(x_n, x_{n-1})$ and $p(x_{n-1})$ in a paradigmatic case ($m = 1$).

The kernel estimation for conditional entropy defined in Eq. (16), when implemented applying the heaviside kernel function and using the maximum norm to compute distances, is equivalent to the sample entropy (SampEn) [2], a well-known measure of dynamical complexity proposed to reduce the bias

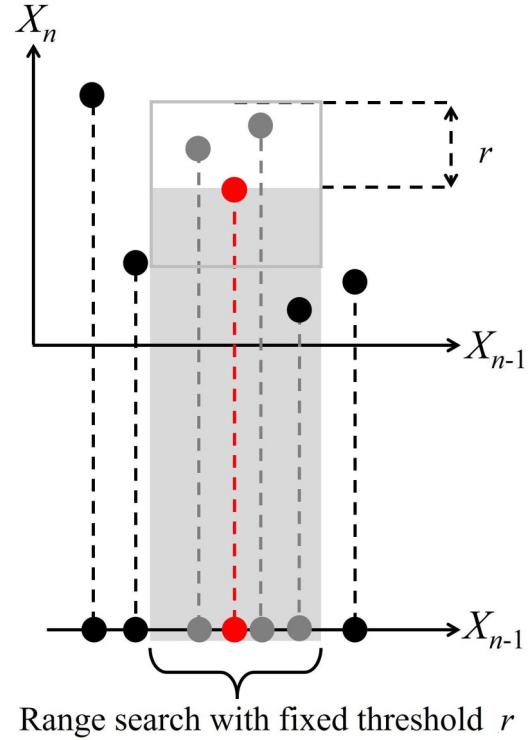


FIG. 3. Schematic illustration of the kernel estimation of entropy measures. In this example, the past of the process X is approximated using $m = 1$ samples, and the Heaviside kernel with fixed threshold r is used. In the $(m+1)$ -dimensional space spanned by the realizations of (X_n, X_{n-1}) , the probability of a given reference point (x_n, x_{n-1}) (red dot) is estimated as the fraction of points whose distance are less than r (gray dots) from it: $p(x_n, x_{n-1}) = 2/7$. The distance between two points is computed as the maximum between the horizontal and the vertical distance between the two points. Similarly, in the m -dimensional space spanned by the realizations of X_{n-1} , the probability of x_{n-1} is approximated using the same threshold r , yielding $p(x_{n-1}) = 3/7$. This procedure is repeated varying the reference point and the conditional entropy is estimated by Eq. (16).

of the first introduced kernel-based measure of conditional entropy, i.e., the approximate entropy (ApEn) [1]. These measures, and more generally all kernel-based estimators of conditional entropy and information storage, are ubiquitously used to assess the dynamical complexity of time series in several fields ranging from physics to engineering, biology, and medicine [25,29–31,33,37,102,103]. Therefore, it is of utmost importance to investigate how these estimates behave in the conditions typical of real-world time series analysis, as well as to understand their range of applicability and limitations.

3. Nearest-neighbor estimator

The k -nearest-neighbor estimator (knn) is another model-free approach that approximates the probability distribution from multiple observed realizations of the considered variable, and then plugs this probability into the entropy definition to yield the entropy estimate. The knn estimator approximates the probability distribution from the statistics of the distances between neighboring points in the multidimensional spaces spanned by the observed variables [100]. Compared to the

kernel estimator, which fixes the neighborhood size for the reference point according to a given threshold distance, the knn estimator fixes the number of neighbors of the reference point and quantifies the neighborhood size by computing the distance between the reference point and its k th nearest neighbor. Specifically, the method builds on the central results, published in Refs. [100,101], stating that the average Shannon information content of a generic d -dimensional random variable V can be estimated from a set of realizations $\{v_1, v_2, \dots, v_N\}$ of the variable as

$$-\mathbb{E}[\ln p(v_n)] = \psi(N) - \psi(k) + d\mathbb{E}[\ln \varepsilon_n], \quad (19)$$

where ψ is the digamma function and ε_n is twice the distance between the outcome v_n and its k th nearest neighbor computed according to the maximum norm (i.e., taking the maximum distance of the scalar components).

Exploiting Eq. (19), one can easily derive the expression for the knn estimate of the entropy of the present state of the process X computed for the time series $\{x_1, x_2, \dots, x_N\}$:

$$E(X) = H(X_n) = \psi(N) - \psi(k) + \langle \ln \varepsilon_n \rangle. \quad (20)$$

Then, according to Eq. (7), the conditional entropy can be computed as the difference between the joint entropy of the present and the past, $H(X_n^m, X_n)$, and that of only the past of the process, $H(X_n^m)$. The information storage can be computed as the difference between entropy and conditional entropy. However, since $H(X_n)$, $H(X_n^m)$, $H(X_n^m, X_n)$ are computed in spaces with different dimensions (respectively, 1, m and $m+1$), the naive application of the same neighbor search procedure in all spaces would result in different distance lengths when approximating the probability density in different dimensions, which would introduce different estimation biases that cannot be compensated by taking the entropy differences. Therefore, in order to keep the same distance length in all explored spaces, we adopt the solution [101] of performing a neighbor search only in the highest-dimensional space and projecting the distances found in this space to the lower-dimensional spaces, keeping these distances as the range within which neighbors are counted. An example is depicted Fig. 4 for the paradigmatic case of $m=1$. Specifically, the knn estimate of $H(X_n^m, X_n)$ is computed through the neighbor search:

$$H(X_n, X_n^m) = \psi(N) - \psi(k) + (m+1)\langle \ln \varepsilon_n \rangle, \quad (21)$$

where ε_n is twice the distance from (x_n, x_n^m) to its k th nearest neighbor, and then, given the distances ε_n , the entropies in the lower-dimensional spaces are estimated through a range search:

$$H(X_n^m) = \psi(N) - \langle \psi(N_{X_n^m}) \rangle + m\langle \ln \varepsilon_n \rangle, \quad (22)$$

$$H(X_n) = \psi(N) - \langle \psi(N_{X_n}) \rangle + \langle \ln \varepsilon_n \rangle, \quad (23)$$

where N_{X_n} and $N_{X_n^m}$ are the number of points whose distance from X_n and X_n^m , respectively, is smaller than $\varepsilon_n/2$. Finally, the conditional entropy is obtained by subtracting

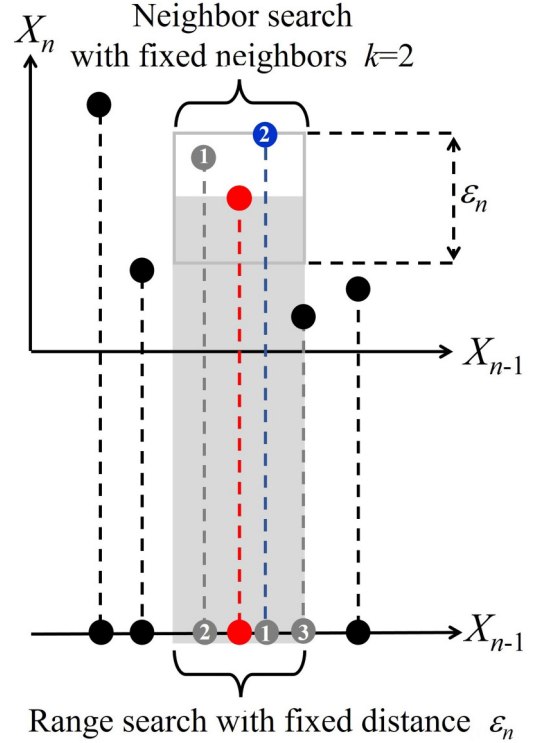


FIG. 4. Schematic illustration of the knn estimation of entropy measures. In this example, the past of the process X is approximated with $m=1$ samples and $k=2$ neighbors are used in the search for neighbors. In the $(m+1)$ -dimensional space spanned by the realizations of (X_n, X_{n-1}) , a neighbor search is performed using the maximum norm to find the k th nearest neighbor (blue dot) of the assigned reference point (red dot). Then, the distance between these two points, $0.5\varepsilon_n$ is used in the projected one-dimensional space spanned by the realizations of $X_n^1 = X_{n-1}$ as threshold distance to find the neighbors of the reference point x_{n-1} ; in this example, $N_{X_n^1} = 3$ neighbors are counted. This procedure is repeated varying the reference point and the obtained values of ε_n and $N_{X_n^1}$ are then used in Eq. (24) to compute the conditional entropy.

Eq. (22) from Eq. (21):

$$C(X) = H(X_n | X_n^m) = -\psi(k) + \langle \psi(N_{X_n^m}) \rangle + \langle \ln \varepsilon_n \rangle, \quad (24)$$

and the information storage is obtained subtracting Eq. (21) from the sum of Eqs. (22) and (23) [26]:

$$\begin{aligned} S(X) &= I(X_n; X_n^m) \\ &= \psi(N) + \psi(k) - \langle \psi(N_{X_n^m}) \rangle - \langle \psi(N_{X_n}) \rangle. \end{aligned} \quad (25)$$

Since the nearest-neighbor technique results in an adaptive resolution as it changes the distance scale according to the underlying probability distribution [97,99], and may also achieve bias compensation when implemented through distance projection [101], this approach has gained in recent years increasing popularity for the estimation of entropy measures in time series analysis. While the utilization of this estimator has been directed up to now mostly to the computation of entropy measures for multivariate time series where the issue of dimensionality is more serious [14,25,104–106], in this study we consider its implementation for the computation of

entropy measures for individual time series, as first proposed in [106].

C. Simulation model of stochastic processes

In this section, we introduce the models to simulate four different types of stochastic processes: stationary autoregressive process, autoregressive process with nonstationarities, fractionally correlated process, and fractionally integrated autoregressive process.

We start with the stationary autoregressive process (AR process), which constitutes the basic process on which entropy measures can be applied. For this type of process, techniques to compute the exact theoretical values of the various entropy measures are available [13] and are here reviewed in the Appendix. We use these theoretical values as a reference to evaluate the performance of different entropy estimators. Results of this basic process will serve as a baseline for more complicated processes that are studied later.

Second, we superimpose three types of nonstationarities (i.e., sinusoidal trends, spikes, and local variance changes) on the stationary AR signal. These nonstationarities are selected as they are commonly encountered in real-world time series as factors corrupting the underlying dynamics [57,58,107–110]. In our simulations, by comparing the estimated values of entropy measures for AR signals with nonstationarity and their corresponding theoretical values for original stationary AR signals, we aim to understand the effects of nonstationarity on entropy estimation and figure out potential solutions to mitigate or remove consequent biases.

In addition to the autoregressive process, we also investigate processes with long-range power-law correlations, a property exhibited by many empirical time series such as the human heart rate or the price index of the stock market [58,109]. Unlike the autoregressive process which is considered to be short memory, these processes, usually referred to as fractionally integrated processes, often exhibit long-range or medium-range dependence [111]. In other words, a fractionally integrated process has an autocorrelation function that damps hyperbolically, more slowly than the geometric damping of an autoregressive process. Despite the fact that entropy measures are typically applied to time series with long-range power-law correlation [2,3,24,27,30,30,31,37,89,106], it is not well understood how these measures relate to this type of long-memory dynamics and how their estimation is affected by properties of correlations including its sign and strength. To fill in this knowledge gap, we first extend the approach used in Ref. [13] to compute the theoretical values of entropy measures from given simulation parameters for fractionally integrated processes, as shown in the Appendix. In addition, we compare these theoretical values with the estimated values of different entropy measures and estimators to evaluate their estimation bias. In this way, our work provides a reference for the application of entropy measures and estimators to power-law long-range correlated processes.

Last, we consider more general cases of processes with both autoregression and power-law long-range correlations and follow the same procedures to evaluate the performance of entropy measures and estimators by computing and comparing their estimates with the corresponding theoretical values.

1. Stationary AR process

The AR process is simulated as the output process of a linear univariate AR model driven by a stochastic uncorrelated noise. Using the polynomial notation, an autoregressive process of order p can be expressed as

$$A(L)X_n = U_n, \quad (26)$$

where $A(L) = 1 - \sum_{i=1}^m A_i L^i$ is an autoregressive polynomial of order m , L is the backward shift operator ($L^i X_n = X_{n-i}$), and U is a white Gaussian innovation process with zero mean and unit variance.

In this study we simulate an AR process of order $m = 2$ by placing two complex-conjugate poles [roots of $A(L)$] in the complex plane, with modulus ρ and phase $\pm 2\pi f$, in a way such that the coefficients of the AR polynomial become

$$A_1 = 2\rho \cos(2\pi f), \quad A_2 = -\rho^2. \quad (27)$$

With this setting, the parameters ρ and f determine, respectively, the amplitude and frequency of a stochastic oscillation that is imposed for the process. Note that the process is stationary when $\rho \in [0,1)$ and that the AR amplitude ρ determines the regularity of the stochastic oscillation: the process is a fully unpredictable white noise when $\rho = 0$, and becomes a highly predictable stochastic process exhibiting a marked oscillatory behavior around the frequency f when ρ approaches 1.

Stationary realizations of the AR process described above, generated with different values set for the AR amplitude ρ and frequency f , are given in Fig. 5. Comparing Figs. 5(a)–5(c) by column one can see that, for an assigned frequency f , the process is more regular for higher values of ρ , confirming the expected increase in the predictability of the process with the AR amplitude. On the other hand, variations in the predictability of the process are more difficult to appreciate when f is varied by keeping fixed the AR amplitude ρ . To investigate this dependence in more detail, Figs. 5(d) and 5(e) report, respectively, the autocorrelation function of the process, and the two-dimensional (2D) and three-dimensional (3D) phase plots of the temporal relation between the present and the two past samples (X_n versus X_{n-1}, X_{n-2}), computed for the realizations of Fig. 5(c). These plots indicate that the process exhibits longer memory, as well as a much stronger linear dependence of the present on the past values, when the AR frequency is very low ($f = 0.01$) or very high ($f = 0.49$) compared to the intermediate value ($f = 0.25$). This suggests that, besides the pole modulus ρ , also the frequency f of the stochastic oscillation of an AR process plays a role in determining its degree of regularity.

2. AR process with nonstationarity

Stationarity is a prerequisite for the computation of the entropy measures from an individual realization of the process under investigation. In fact, if the process is nonstationary, the joint probability distribution of its present and past values changes over time, which precludes the possibility of pooling observations across time for estimating of such probabilities. If observations are pooled across time in the presence of nonstationarities, the estimated probability distribution is unreliable and the resulting entropy measures deviate from

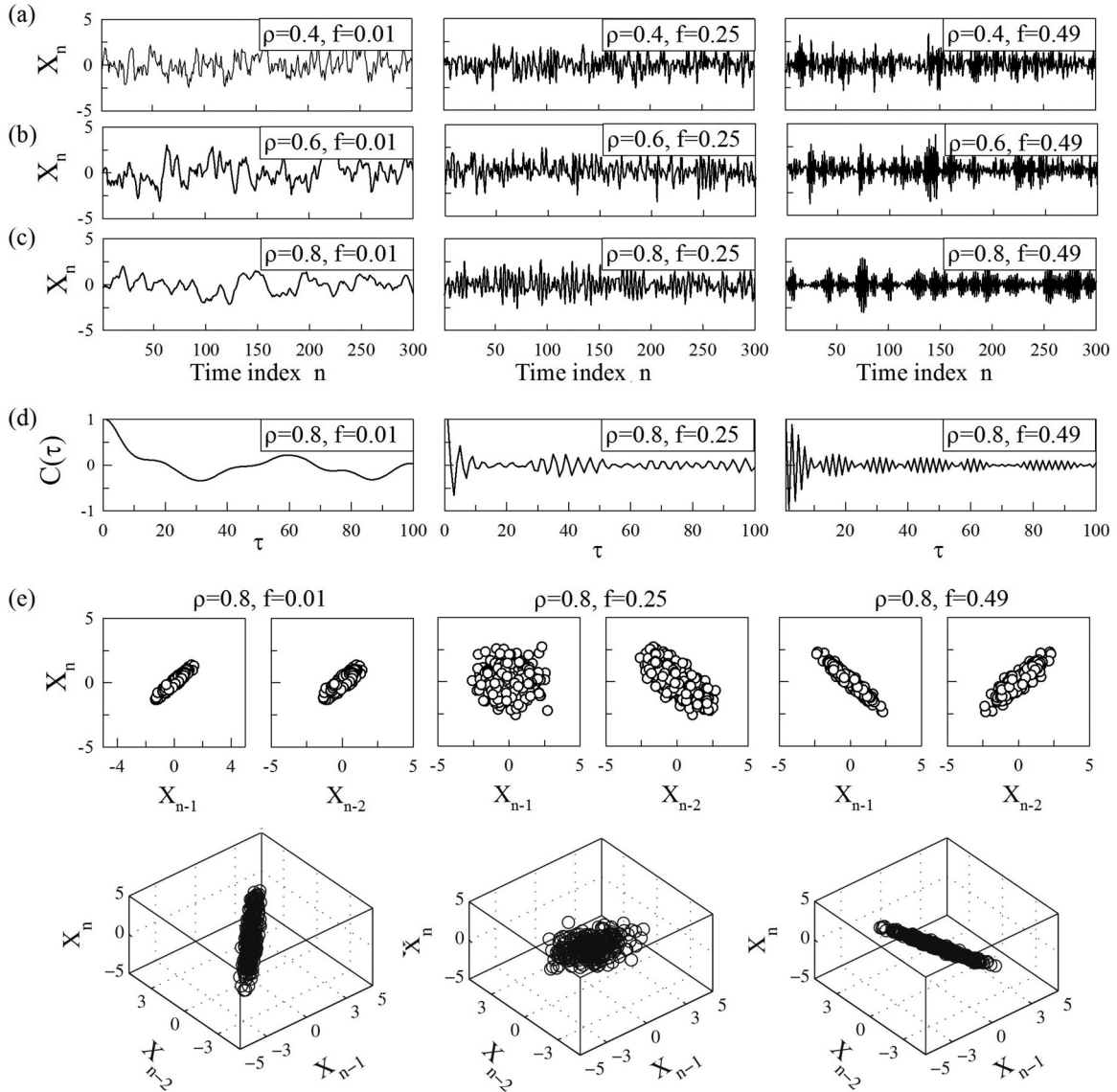


FIG. 5. Autoregressive processes: characterization of a stationary order-2 AR process for different values of the AR amplitude ρ and frequency f . (a)–(c) Exemplary realizations of the process obtained varying ρ (columns) and f (rows). Results: When f is fixed, the process appears more regular for higher values of ρ . (d) Autocorrelation of the process as a function of the lag τ for the realizations in (c). (e) 2D phase plots of (X_n, X_{n-1}) and (X_n, X_{n-2}) , and 3D phase plots of (X_n, X_{n-1}, X_{n-2}) , for the realizations in (c). When ρ is fixed, the process exhibits shorter memory and weaker dependence of the present on the past for intermediate frequency f .

the value assumed for a stationary distribution to an extent depending on the type and strength of the nonstationary behavior.

Here we study the effects of three types of nonstationarities due to common artifacts, including trends, spikes, and local changes in the signal variance, on the entropy, conditional entropy, and information storage of the AR process of order 2 described above. To reproduce these situations, we superimpose the chosen type of nonstationary behavior to stationary realizations of the AR process generated according to Eqs. (26) and (27). Nonstationary AR signals with sinusoidal trends are obtained by adding to the original stationary AR signals a sine wave of period T and amplitude A . Signals with random spikes with amplitude A and percentage $P\%$ are generated by replacing random points of the original time series with random numbers uniformly distributed in the

interval $(-A\sigma_X^2, A\sigma_X^2)$, where σ_X^2 is the variance of the original signal. To simulate local changes in variance, we choose random segments from the original time series and inflate these segments by multiplying their original values by a factor of σ . Each inflated segment contains 20 points and the total number of inflated points covers $P\%$ of the original signal length. The resulting realizations of the AR process with superimposed nonstationary behavior were always normalized to zero mean and unit variance before computing the entropy measures. Exemplary realizations of the analyzed nonstationary AR processes are depicted in Figs. 11, 13, and 15.

3. Fractionally integrated white noise process

Stochastic processes with power-law long-range correlations are generated as fractionally integrated white noise [112],

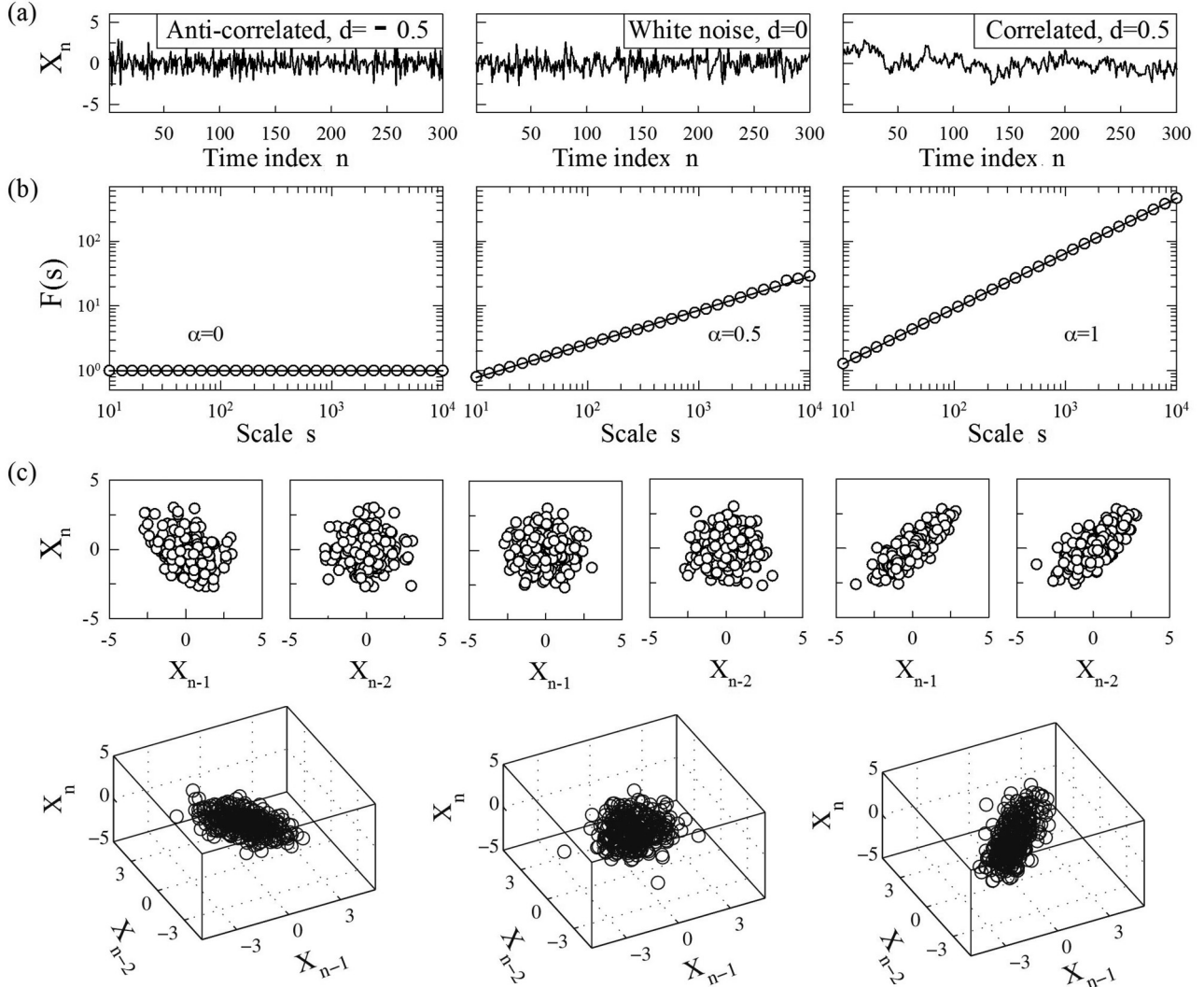


FIG. 6. Processes with long-range correlations: characterization of a fractionally integrated process with long-range power-law correlations for different values of the differencing parameter d , which controls the correlations. (a) Exemplary realizations of the process with $d = -0.5, 0, 0.5$. (b) Results of detrended fluctuation analysis (DFA) applied to longer realizations (2^{20} data points) of the process in (a). For $d \in [-0.5, 0.5]$, the DFA exponent is $\alpha = (2d + 1)/2$. (c) 2D phase plots of (X_n, X_{n-1}) and (X_n, X_{n-2}) , and 3D phase plots of (X_n, X_{n-1}, X_{n-2}) , for the realizations in (a). Results: For fixed modulus of the differencing parameter, positively correlated processes exhibits stronger dependence of the present on the past than anti-correlated processes.

defined by

$$(1 - L)^d X_n = U_n, \quad (28)$$

where U is a Gaussian white noise with zero mean and unit variance, $d \geq 0$ is the so-called differencing parameter and $(1 - L)^d$ is the fractional differencing operator defined by

$$(1 - L)^d = \sum_{k=0}^{\infty} \frac{\Gamma(k-d)L^k}{\Gamma(-d)\Gamma(k+1)}, \quad (29)$$

with $\Gamma(\cdot)$ denoting the gamma (generalized factorial) function. In this study, computation of Eq. (29) is approximated by $(1 - L)^d = \sum_{k=0}^{100} \frac{\Gamma(k-d)L^k}{\Gamma(-d)\Gamma(k+1)}$. The differencing parameter d controls the sign and degree of the correlations imposed in the process. It is related to the Hurst exponent, α , by the relation $\alpha = (2d + 1)/2$, $d \in [-0.5, 0.5]$ [113]. Within this range of values for d , the fractionally integrated process is considered

as stationary [112]. For $d \in (0, 0.5]$, the process is long-range correlated, showing long-range positive dependence, while for $d \in [-0.5, 0)$, it is anti-correlated, showing long-range negative dependence. The case $d = 0$ reduces to uncorrelated white noise.

Figure 6(a) shows exemplary realizations of fractionally integrated white noise with differencing parameter set to $d = -0.5$, $d = 0$, and $d = 0.5$. The corresponding multifractal behavior obtained through detrended fluctuation analysis is depicted Fig. 6(b), confirming the relation between the fractional differencing parameter d and the Hurst exponent α . Figure 6(c) depicts the two-dimensional phase plots of (X_n, X_{n-1}) and (X_n, X_{n-2}) and three-dimensional phase plots of (X_n, X_{n-1}, X_{n-2}) for anticorrelated, uncorrelated, and positively correlated time series. The plots evidence a cloud distribution of the points reflecting the absence of a dependence of the present on the past for the uncorrelated

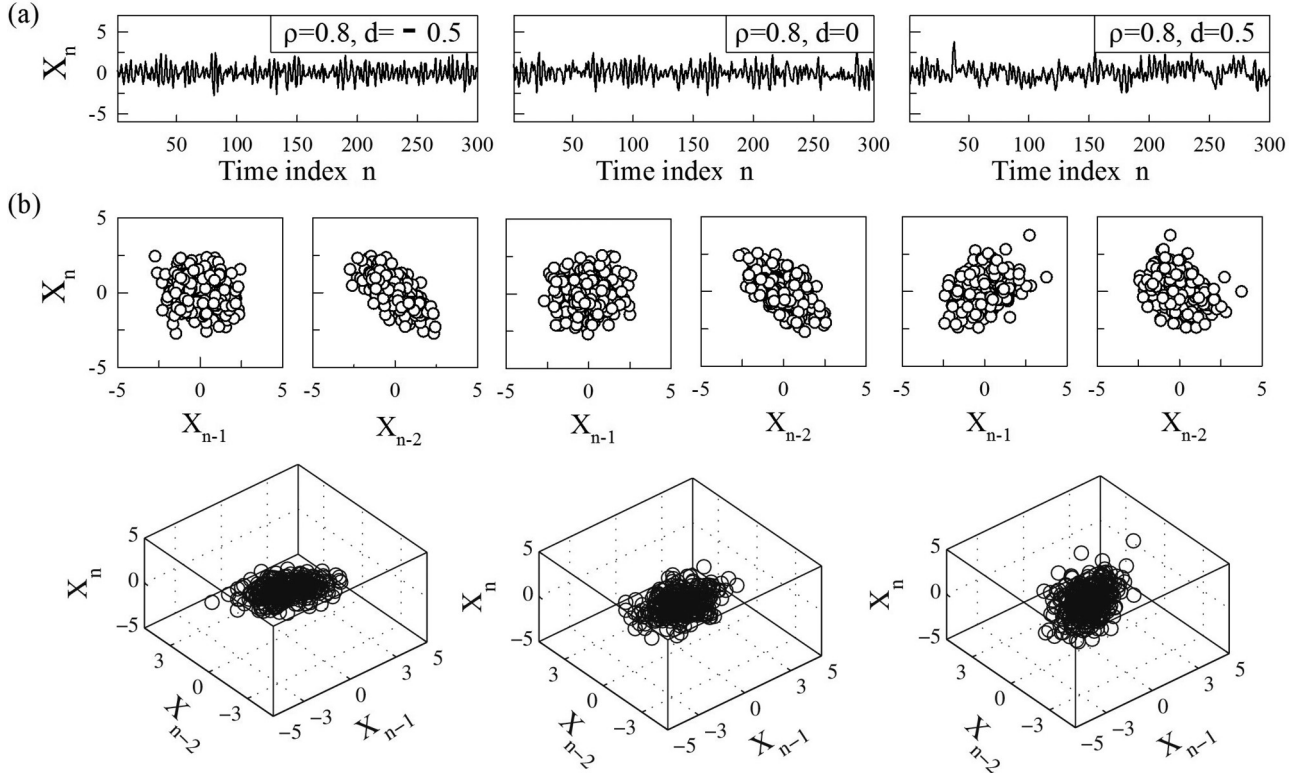


FIG. 7. Autoregressive processes with long-range correlations: characterization of a stationary fractionally integrated AR process with both autoregression and power-law long-range correlations for different values of the differencing (correlation) parameter d and fixed values of the AR parameters ρ and f . (a) Exemplary realizations of the process with $d = -0.5, 0, 0.5$ and fixed $\rho = 0.8, f = 0.25$. (b) 2D phase plots of (X_n, X_{n-1}) and (X_n, X_{n-2}) , and 3D phase plots of (X_n, X_{n-1}, X_{n-2}) for the realizations in (a). Results: The fractionally integrated AR process displays weaker dependence of the present on the past than the corresponding pure autoregressive process with the same AR parameters in the presence of positive long-range correlations and stronger dependence in the presence of negative long-range correlations.

case (middle); moreover, when the degree of correlation is the same, a much stronger dependence of the present on the past is exhibited for a process with positive correlation (right) than for a process with anticorrelation (left).

4. Fractionally integrated AR process

The combination of the autoregressive process and the fractionally integrated processes defined in Eqs. (26) and (28) results in a more general univariate process exhibiting both stochastic oscillations and long memory. The resulting process, which belongs to the class of fractionally integrated autoregressive moving average processes (ARFIMA) [112], is defined as follows:

$$A(L)(1-L)^d X_n = U_n. \quad (30)$$

Figure 7 shows exemplary realizations and phase plots of this fractionally integrated autoregressive process with fixed AR amplitude $\rho = 0.8$ and varying differencing parameter $d = -0.5, 0, 0.5$. Compared with the case in which the process is not long-range correlated but purely autoregressive [Fig. 7(a), middle, $\rho = 0.8, d = 0$], the combination of the AR stochastic oscillations with positive long-range correlations [Fig. 7(a), right, $\rho = 0.8, d = 0.5$] seems to slightly reduce the dependence of the present of the process on its past, while the opposite seems to occur when AR stochastic oscillations are combined with negative long-range correlations [Fig. 7(a),

left, $\rho = 0.8, d = -0.5$]. The same effect, i.e., a decrease of the predictability of the present given the past for positive long-range correlations and an increase of this predictability for negative long-range correlations, is observed comparing the case of mixed AR and fractionally integrated processes [Fig. 7(a)] with the pure fractionally integrated process [Fig. 6(a)]. Thus, a process with both AR short-term dependencies and long-range correlations results less predictable than its pure autoregressive or pure fractionally integrated counterparts in the case of positive long-range correlations and more predictable in the case of anticorrelations.

III. RESULTS

This section provides the results for the application of the three entropy measures defined in Sec. II A (i.e., entropy, conditional entropy, and information storage) computed using the three entropy estimators presented in Sec. II B (i.e., linear, kernel, and knn) on the four types of stochastic processes discussed in Sec. II C (i.e., stationary AR processes, AR processes with different types of nonstationarity, power-law long-range correlated processes, and process with both AR structure and long-range correlation). For each type of process, we first theoretically obtain the true values of all three entropy measures through analytical derivations starting from the assigned model parameters. Then, using the same simulation

model and model parameters, we compute the estimated values of entropy measures using all three estimators for 100 realizations of the target process. Each realization typically lasts 300 points. All the analyzed processes have zero mean and are reduced to unit variance prior to the computation of entropy measures. All entropy estimations are performed using $m = 2$ lagged components to approximate the past of the process (i.e., $X_n^m = [X_{n-1}, X_{n-2}]$); this setting corresponds to choosing the true order of the simulated AR process, so as to make the interpretation of results free from issues related to an inappropriate selection of the embedding dimension.

A. Performance of entropy estimators and entropy measures for stationary AR processes

Figure 8 reports the characterization of entropy measures and entropy estimators for the case of a stationary AR process. For this process, the exact behavior of the entropy measures in response to changes in the analysis parameters can be studied by looking at the theoretical values (black solid lines), and can be compared with the distributions of values obtained applying the different estimators to multiple realizations of the process generated from setting specific values for the parameters (symbols and error bars).

The theoretical values of all entropy measures are obviously the same for different lengths of the generated realizations [Figs. 8(d), 8(e), and 8(f)]. Moreover, since this example deals with normalized Gaussian processes with zero mean and unit variance, the entropy of the process is constant at varying the AR parameters ρ and f [Figs. 8(g) and 8(j)]. On the other hand, when f is fixed and ρ increases, the theoretical value of conditional entropy decreases and that of information storage increases. When ρ is fixed and f increases, the theoretical value of conditional entropy increases for $f \in (0, 0.25]$ and decreases for $f \in (0.25, 0.5)$. The theoretical behavior of information storage is the opposite. The dependence of the measures of dynamical complexity on the AR amplitude is expected: a process with higher ρ exhibits a stronger dependence of the present on the past, and this better predictability is reflected by lower conditional entropy and higher information storage. On the other hand, the dependence of the entropy measures on the AR frequency, documented in Figs. 8(k) and 8(l) and in more cases in Fig. 10, is a less expected behavior, which indicates the existence of a complex relation between the statistical structure of a dynamic process and its information content.

Turning to the analysis of the entropy estimates first, we see that, as one may expect, the estimated values exhibit lower variability while increasing the time series length. This behavior is particularly evident for the kernel estimator, confirming the findings of previous studies [11, 12]. The kernel estimator also shows a substantially higher variance compared to that of the linear and knn estimators [Figs. 8(e) and 8(f)]. In addition, we find that the kernel estimates of entropy and conditional entropy are strongly biased for all values of the analysis parameters [Figs. 8(d), 8(e), 8(g), 8(h), 8(j), and 8(k)]. The bias is less evident for the kernel estimates of information storage, and is generally low or negligible for the linear and knn estimates of all measures.

In Fig. 9 we investigate how the estimates of the different entropy measures are affected by the choice of the analysis parameters. The linear estimation approach has no free parameters and, for this case in which the amplitude distribution of the simulated process matches the assumption of Gaussianity made by the estimator, it returns very precise estimates for all measures [Figs. 9(a)–9(c)]. The kernel estimator turns out to be very sensitive to the choice of its free parameter, the threshold r . Specifically, as shown in Figs. 9(d) and 9(e), when r decreases from 0.5 to 0.2 and 0.1, we observe that the estimates of entropy and conditional entropy are higher and exhibit larger variability. Such sensitive dependence on the threshold r results from the partition rule of the state space used by the kernel estimator. The threshold r is the width of the Heaviside kernel function and determines the size of the cells used for probability estimation: when r decreases, less points are included in the cell used to estimate probabilities; as a result, the estimated probabilities are lower, leading to higher entropy estimates regardless of the true underlying value. On the contrary, when r increases, more points are included in the neighborhood of any reference point, increasing the estimated probability and thus leading to a lower entropy estimate. This holds regardless of the type of kernel function used for entropy estimation, and determines a substantial unreliability for the absolute values of entropy and conditional entropy estimated with the kernel method. The bias (but not the variance) is compensated for the estimates of information storage [Figs. 9(d)–9(f)]. On the contrary, results from the knn estimator are more accurate for the estimation of all entropy measures and much less dependent on the choice of its free parameter k denoting the number of neighboring points used for probability estimation.

Figure 10 provides a more detailed analysis of the dependence of entropy measures on the parameters of a stationary AR process. In this case, where both the AR amplitude ρ and the AR frequency f are varied, we see that the entropy measures reflect the signal properties observed in Fig. 5: increasing ρ with constant f , or moving f away from 0.25 with constant ρ , yields a decrease of conditional entropy and an increase of information storage that indicate lower complexity and higher regularity of the dynamics. Moreover, by comparing the theoretical and estimated values for the different estimators we found that—despite the bias in the kernel estimation of entropy and conditional entropy—all of the estimators can follow the changes in entropy measures when the internal dynamics of the stationary AR process changes. However, unlike the linear estimator which makes an accurate approximation of all entropy measures for all combinations of AR parameters, the kernel and knn estimators exhibit a bias when the AR amplitude is high ($\rho \geq 0.8$) and the AR frequency is very low ($f < 0.1$) or very high ($f > 0.4$).

In summary, the simulations reported in this section indicate that the assessment of entropy measures is not an easy task even for the simple case of stationary AR processes. Theoretically, the expected values of conditional entropy and information storage are dependent on the features of the process in a way that is not always straightforward. Moreover, the practical estimation of these measures is not an easy task: while for the linear estimator computation is accurate thanks to the close correspondence between model assumptions and properties

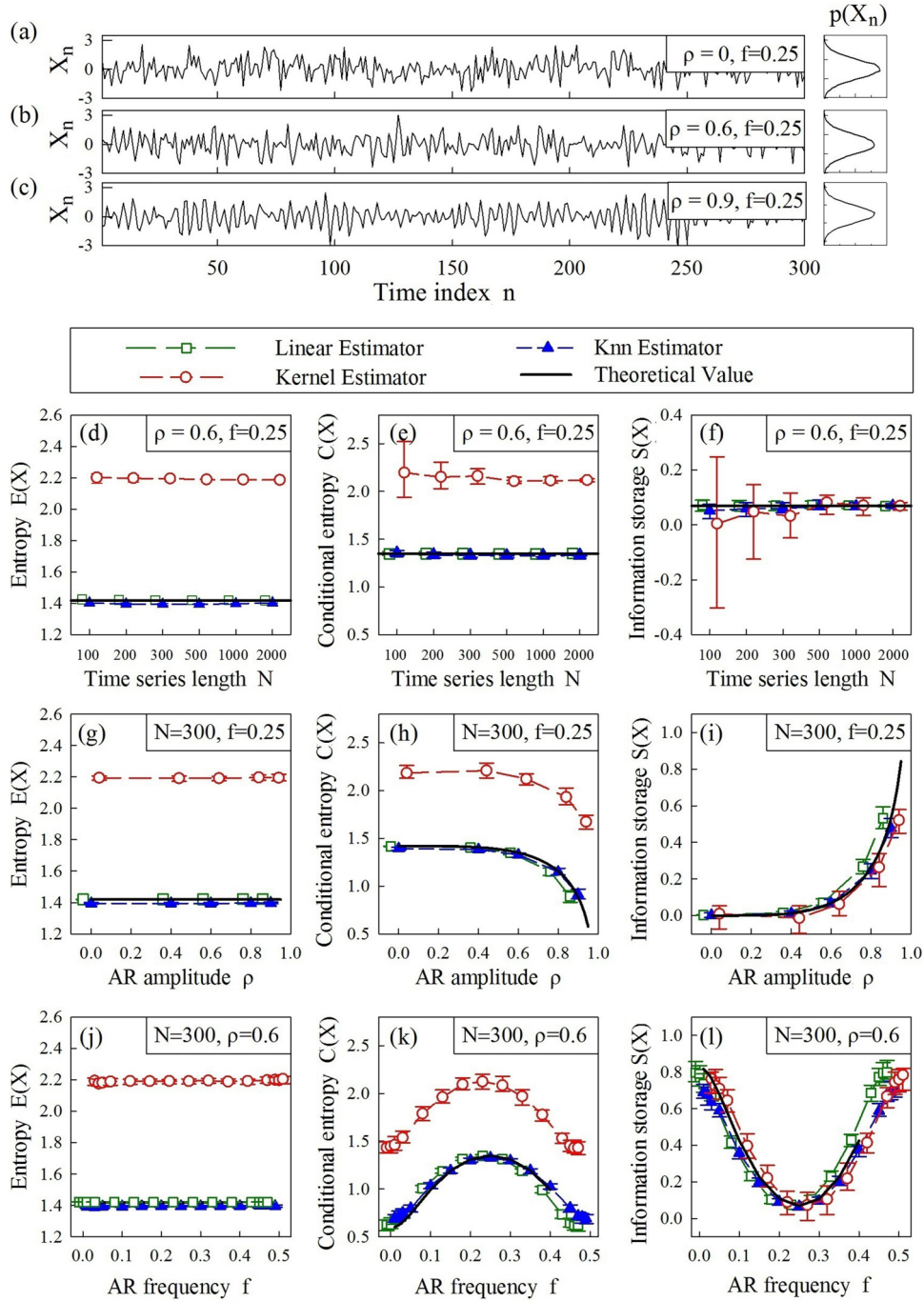


FIG. 8. Performance of entropy estimators and entropy measures for stationary AR processes. (a)–(c) Exemplary realizations of AR processes generated with fixed $f = 0.25$ and varying $\rho = 0, 0.6, 0.9$, with corresponding probability distributions reported on the right; note that if $\rho = 0$ the process is a white noise $\forall f$. (d)–(f) Dependence of entropy measures and entropy estimates, obtained for AR processes with fixed amplitude and frequency ($\rho = 0.6, f = 0.25$), on the length N of the time series generated as process realizations. (g)–(i) Dependence of entropy measures and entropy estimates on the AR amplitude ρ with fixed AR frequency ($f = 0.25$) and time series length ($N = 300$). (j)–(l) Dependence of entropy measures and entropy estimates on the AR frequency with fixed AR amplitude $\rho = 0.6$ and time series length ($N = 300$). Panels (d)–(l) report the theoretical values (black solid line) and the estimated distributions (mean and 25%–75% percentiles over 100 realizations) of entropy (d), (g), (j), conditional entropy (e), (h), (k), and information storage (f), (i), (l) obtained with the linear estimator (green squares), the kernel estimator implemented with threshold $r = 0.2$ (red circles), and the knn estimator implemented with $k = 10$ neighbors (blue triangles). Results: The expected values of all entropy measures do not change with the realization length N . Moreover, for these normalized time series the theoretical values of entropy are unaffected by the AR parameters. The conditional entropy decreases with the increase of ρ when f is fixed, and increases with increasing f for $f \in (0, 0.25]$ and decreases for $f \in (0.25, 0.5)$ when ρ is fixed. The theoretical behavior of information storage is the opposite of that of the conditional entropy. The estimates obtained with the linear and knn estimators are close to the theoretical values for all entropy measures, while the estimates of entropy and conditional entropy obtained with the kernel estimator are strongly biased and exhibit high variance for short time series.